Lappeenranta
University of Technology

Adam Kłodowski

FLEXIBLE MULTIBODY APPROACH IN BONE STRAIN ESTIMATION DURING PHYSICAL ACTIVITY: QUANTIFYING OSTEOGENIC POTENTIAL

Thesis for the degree of Doctor of Science (Technology) to be presented with due permission for the public examination and criticism in Auditorium 1383 at the Lappeenranta University of Technology, Lappeenranta, Finland on the 26th of October, 2012, at noon.

Acta Universitatis
Lappeenrantaensis 483

Supervisor

Professor Aki Mikkola
Department of Mechanical Engineering
Lappeenranta University of Technology
Finland

Reviewers

Professor Javier Cuadrado
Laboratory of Mechanical Engineering
Department of Industrial Engineering II
University of La Coruña
Spain

Professor Daniel García Vallejo
Department of Mechanical and Materials Engineering
University of Seville
Spain

Opponents

Professor Jorge Ambrósio
Institute for Mechanical Engineering
Technical University of Lisbon
Portugal

Professor Daniel García Vallejo
Department of Mechanical and Materials Engineering
University of Seville
Spain

ISBN 978-952-265-288-1
ISBN 978-952-265-289-8 (PDF)
ISSN 1456-4491

Lappeenranta University of Technology
Digipaino 2012

Abstract

Adam Kłodowski

Flexible multibody approach in bone strain estimation during physical activity: quantifying osteogenic potential

Lappeenranta, 2012

122 pages

Acta Universitatis Lappeenrantaensis 483

Diss. Lappeenranta University of Technology

ISBN 978-952-265-288-1, ISBN 978-952-265-289-8 (PDF), ISSN 1456-4491

Bone strain plays a major role as the activation signal for the bone (re)modeling process, which is vital for keeping bones healthy. Maintaining high bone mineral density reduces the chances of fracture in the event of an accident. Numerous studies have shown that bones can be strengthened with physical exercise. Several hypotheses have asserted that a stronger osteogenic (bone producing) effect results from dynamic exercise than from static exercise. These previous studies are based on short-term empirical research, which provide the motivation for justifying the experimental results with a solid mathematical background. The computer simulation techniques utilized in this work allow for non-invasive bone strain estimation during physical activity at any bone site within the human skeleton. All models presented in the study are three-dimensional and actuated by muscle models to replicate the real conditions accurately.

The objective of this work is to determine and present loading-induced bone strain values resulting from physical activity. It includes a comparison of strain resulting from four different gym exercises (knee flexion, knee extension, leg press, and squat) and walking, with the results reported for walking and jogging obtained from *in-vivo* measurements described in the literature. The objective is realized primarily by carrying out flexible multibody dynamics computer simulations. The dissertation combines the knowledge of finite element analysis and multibody simulations with experimental data and information available

from medical field literature. Measured subject-specific motion data was coupled with forward dynamics simulation to provide natural skeletal movement. Bone geometries were defined using a reverse engineering approach based on medical imaging techniques. Both computed tomography and magnetic resonance imaging were utilized to explore modeling differences.

The predicted tibia bone strains during walking show good agreement with *in-vivo* studies found in the literature. Strain measurements were not available for gym exercises; therefore, the strain results could not be validated. However, the values seem reasonable when compared to available walking and running *in-vivo* strain measurements. The results can be used for exercise equipment design aimed at strengthening the bones as well as the muscles during workout. Clinical applications in post fracture recovery exercising programs could also be the target. In addition, the methodology introduced in this study, can be applied to investigate the effect of weightlessness on astronauts, who often suffer bone loss after long time spent in the outer space.

Keywords: bone strength, exercise optimization, component mode synthesis, CT, MRI

UDC 531.39 : 621.8 : 612.75 : 004.94

Acknowledgments

Biomechanics is an interesting field of research. Thanks to support from the Academy of Finland (project name: ABIMA, number: 138574) and the Tampere Graduate School of Concurrent Mechanics, it was possible for me to get familiar with topics related to human motion, bone strain, and musculoskeletal models in terms of modeling and simulation. The research was conducted at the Lappeenranta University of Technology with the cooperation of the University of Jyväskylä and support from the UKK institute, Tampere. The opportunity to work in this field was given to me by Professor Aki Mikkola, who organized financial resources and a good research team. During the studies, I had the pleasure of working with Dr. Rami Al Nazer, who was finishing his doctoral thesis while working with me. I would like to thank Dr. Timo Rantalainen from the University of Jyväskylä, who gave me insight into the medical aspects of human modeling and was an invaluable help when conducting experimental tests. A significant part of this work was accomplished with help from Dr. Pertti Kolari, who voluntarily participated in several experiments and informed me about additional opportunities for research funding.

Quality of this work was constantly improved thanks to the comments and improvement suggestions from my colleagues: Elias Altarriba, John Bruzzo, Oleg Dmitrochenko, Janne Heikkinen, Behnam Ghalamchi, Mika Harjula, Juha Kortelainen, Emil Kurvinen, Marko Matikainen, Tuomas Rantalainen, and Antti Valkeapää.

Special thanks for Scott Semken and Juha Laurinolli for their laborious work on checking the grammar and spelling of this work and related articles.

At last, I would like to thank my family for the support they have given me throughout my PhD studies. I would like to thank my mother, Elżbieta, for her patience and encouragement; my father, Bogusław, for providing me support and motivation; and finally, my brother, Krzysztof, who has many times challenged my ideas and given me inspiration for my work.

Adam Kłodowski

Lappeenranta, 4th of September, 2012

Table of Contents

1 **Introduction** 21

1.1 Bone strengthening potential of exercises 22

1.2 Human bone endurance 24

1.3 *In-vivo* strain measurements 25

1.4 The motivation for computational models 27

1.5 Scientific contribution of the work 28

2 **Materials and methods** 31

2.1 Rigid body dynamics of multibody systems 31

2.2 Flexible multibody dynamics 37

2.3 Bone flexibility description and strain estimation 41

2.4 Medical imaging techniques 44

2.5 Medical image data 45

2.6 Bone geometry reconstruction 46

2.7 Bone material models 47

2.8 Actuation systems 51

2.8.1 *Torque actuators* 51

2.8.2 *Muscle actuators* 52

2.9 Contact definition 55

2.10 Musculoskeletal model description 58

2.10.1 *Joint description* 58

2.10.2 *Muscle models configurations* 59

2.11 Modeling environment and simulation procedure 60

2.12 Human musculoskeletal models validations methods 62

2.12.1 *Motion pattern validation* 62

2.12.2 *External force validation* 62

2.12.3 *Additional validation methods* 63
2.13 Limitations of the models 63
3 **Walking simulations** 65
3.1 The subject 65
3.2 Human gait 65
3.3 Lower leg study 66
3.3.1 *Model description* 66
3.3.2 *Results* 69
3.3.3 *Discussion* 72
3.4 Upper leg study 73
3.4.1 *Model description* 74
3.4.2 *Results* 75
3.4.3 *Discussion* 78
4 **Exercise simulations** 81
4.1 The subject 81
4.2 Leg press 81
4.2.1 *Model description* 81
4.2.2 *Results* 83
4.2.3 *Discussion* 86
4.3 Knee flexion 87
4.3.1 *Model description* 88
4.3.2 *Results* 89
4.3.3 *Discussion* 91
4.4 Knee extension 92
4.4.1 *Model description* 93
4.4.2 *Results* 93
4.4.3 *Discussion* 98

4.5 Squat 99
4.5.1 *Model description* 99
4.5.2 *Results* 100
4.5.3 *Discussion* 103
5 **Conclusions and summary** 105
5.1 Future developments 108
Bibliography 109

List of figures

Figure 1. Comparison of normal and osteoporotic bone structures 21
Figure 2. Incidence rate (per 100,000 persons) of hip fractures in Finland for women and men aged 50 years or older between 1970 and 1997 (Kannus et al., 1999) 22
Figure 3. Bone growth and resorption control process with the load history dependent on the type of physical activity.....23
Figure 4. Strain gauge installation on cadaveric human tibia.....26
Figure 5. Modeling a hydraulic drilling machine as a rigid multibody system – External forces, joints, bodies and global coordinate system are depicted (actuators are not shown in the picture). 32
Figure 6. Description of the position for the point in a rigid body expressed in local (indicated by the l index) and global (x, y, z) coordinate systems 33
Figure 7. Relation between position description of a point in the flexible body in the local (indicated by the l index) and global (x, y, z) coordinate systems ..38
Figure 8. Comparison of tibia tetrahedral mesh size described as the number of degrees of freedom depending on the element size 42
Figure 9. Medical image processing: a) Single threshold applied to a slice of a diaphysis of tibia and fibula produces bone mask, and b) Threshold applied to epiphysis of tibia and fibula requiring additional hole-removal and smoothing47
Figure 10. Schematic diagram of the Hill muscle model.....54
Figure 11. Overview of the locations and shape of the foot contact elements ..55
Figure 12. Schematic description of elements in the ellipsoid-plane contact model.....56
Figure 13. Damping coefficient dependency on penetration depth in the contact pair described as a ratio with respect to the maximum values.....57
Figure 14. Friction coefficient dependency on slip velocity.....57
Figure 15. Simulation procedure – The posture stabilization component is optional and is applied only when necessary. 61
Figure 16. Phases of human gait 65
Figure 17. Improved lower leg model – The rotational and translational joints between tibia and fibula are marked as well as the introduced patellar tendon models. 67
Figure 18. Deformation modes of tibia – Modes with high influence on the total strain energy are additionally highlighted.....69

Figure 19. Deformation modes of fibula – Modes with high strain energy influence are marked with stars. 70
Figure 20. Components of the ground reaction force during one walking cycle: a) horizontal, and b) vertical 71
Figure 21. Principal in-plane strain values on anteromedial aspect of tibial shaft – The node location is indicated by dot. 71
Figure 22. Axial tibial strain values in the middle cross section of the diaphysis 72
Figure 23. Axial strain values in the midshaft of fibula.....72
Figure 24. Discretization of the femur model with respect to bone structure and location – The femoral neck was modeled with the smallest elements. Two orientations of element coordinate systems were used; one for zone 1 and one for zone 2. 75
Figure 25. Femoral deformation modes obtained from the Craig-Bampton modal analysis.....76
Figure 26. Ground reaction forces obtained from simulation and experimental measurements including a) the horizontal component of the ground reaction force along the walking direction, and b) the vertical component of the ground reaction force.....77
Figure 27. Axial strain values at the indicated cross section of the femoral neck during single walking phase.....77
Figure 28. Axial strain values at the proximal lateral aspect of the femur during walking – The node location is indicated by the dot, and the arrow represents the direction along which strain values were measured.....78
Figure 29. Leg press machine multibody model with marked external force, joints and components.....82
Figure 30. Rope force measured during the experiment – Sections A1, B1, C1 correspond to pressing phases; sections A2, B2, C2 correspond to retraction. .83
Figure 31. Leg press cycle timing – Three consequent repetitions are presented and marked A, B, C; respectively. 83
Figure 32. Axial strain values at the midshaft of the tibia resulting from slow-speed leg.....84
Figure 33. Axial strain values at the midshaft of the tibia resulting from moderate-speed leg press 85

Figure 34. Axial strain values at the midshaft of the tibia resulting from high-speed leg press 85
Figure 35. Magnitude of knee force during leg press exercise performed at a) low, b) moderate, and c) high speed 86
Figure 36. Left knee angle time history during leg press exercise performed at a) low, b) moderate, and c) high speed 86
Figure 37. Knee flexion/extension machine multibody model with labeled elements – Joints and external torque are indicated by symbols. 89
Figure 38. Axial strain values at the middle cross section of the tibia during knee flexion performed at low speed 90
Figure 39. Axial strain values at the middle cross section of the tibia during knee flexion performed at moderate speed 90
Figure 40. Axial strain values at the middle cross section of the tibia during knee flexion performed at high speed 91
Figure 41. Knee force during knee flexion performed at a) low, b) moderate, and c) high speed.....91
Figure 42. Axial strain values at the middle cross section of the tibia during knee extension with a 30 kg load performed at low speed 94
Figure 43. Axial strain values at the middle cross section of the tibia during knee extension with a 30 kg load performed at moderate speed 94
Figure 44. Axial strain values at the middle cross section of the tibia during knee extension with a 30 kg load performed at high speed 95
Figure 45. Axial strain values at the middle cross section of the tibia during knee extension with a 40 kg load performed at low speed 95
Figure 46. Axial strain values at the middle cross section of the tibia during knee extension with a 40 kg load performed at moderate speed 96
Figure 47. Axial strain values at the middle cross section of the tibia during knee extension with a 40 kg load performed at high speed 96
Figure 48. Knee forces during knee extension with a 30 kg load performed at a) low, b) moderate, and c) high speed 97
Figure 49. Knee forces during knee extension with a 40 kg load performed at a) low, b) moderate, and c) high speed 97
Figure 50. Overview of the multibody model used in the simulation of squatting with 70 kg of external load – The thick red lines represent muscles and the green spheres represent joints. 100

Figure 51. Timing of squat phases 101
Figure 52. Axial strain values at the midshaft of the left tibia during squat performed at low speed 101
Figure 53. Axial strain values at the midshaft of the left tibia during squat performed at high speed 102
Figure 54. Left knee forces during squat performed at a) low and b) high speed 102
Figure 55. Ground reaction force during the squat exercise at a) low and b) high speed 103

List of tables

Table 1. Young's modulus for bone, literature summary 49
Table 2. Orthotropic elastic properties of femur (Reilly & Burstein, 1975) 49
Table 3. Site specific parameters for dependency of density on Hounsfield units (Rho et al., 1995) 50
Table 4. Parameters for the dependency of Young's modulus versus CT voxel values 51
Table 5. Kinematic joint parameters used in the models (Al Nazer et al., 2008a) 59
Table 6. Hill muscle model parameters 68
Table 7. The principal strain values obtained in the experimental and current study at the proximal aspect of the midshaft of the tibia 70
Table 8. Loading and unloading times for the knee extension 93
Table 9. Extreme strain values during knee extension exercise 98

Nomenclature

Abbreviations

CAD	Computer Aided Design
CT	Computed Tomography
DAE	Differential Algebraic Equations
DICOM	Digital Imaging and Communications in Medicine
DXA	Dual-energy X-ray Absorptiometry
EMG	Electromyography
MRI	Magnetic Resonance Imaging
ODE	Ordinary Differential Equations
PCSA	Physiological Cross-sectional Area
PID	Proportional-Integral-Derivative
QCT	Quantitative Computed Tomography

Typographical convention

- Normal font in equations is used to denote standard mathematical functions.
- **Bolded font** is used in equations to highlight matrices and vectors.
- *Italic font* in the equations denotes scalar values, and in the text Latin phrases.
- Superposed bar is used to denote local values expressed in a local coordinate system.
- Superposed tilde symbol is used to denote skew-symmetric matrix representation of the vector.
- Superposed dot denotes first derivative with respect to time, consequently superposed double dots represent second derivative with respect to time.
- Decimals are separated with dot (.).
- Comma (,) is used as thousand separator.

Latin symbols

$\mathbf{0}$	zero matrix or vector
a	slope parameter
a_ρ	slope parameter for density versus Hounsfield units relationship
$asym$	strain asymptote parameter

$\mathbf{A}$	rotation matrix
$\dot{\mathbf{A}}$	first derivative with respect to time of the rotation matrix
b	intercept or exponential coefficient
b_ρ	intercept parameter for density versus Hounsfield units relationship
c	damping coefficient
c_{max}	maximum damping coefficient
CT	computed tomography raw voxel value
CT_A	computed tomography raw voxel value for air
CT_w	computed tomography raw voxel value for water
$\mathbf{C}$	constraint equations
$\mathbf{C}_{fq}$	constraint Jacobian matrix of a flexible body
$\mathbf{C}_q$	constraint Jacobian matrix of a rigid body
D	derivative coefficient in the PID controller model
$\delta\mathbf{r}$	virtual displacements of global position vector
$\delta\mathbf{q}$	virtual displacements of generalized coordinates of a rigid body
$\delta\mathbf{q}_f$	virtual displacements of generalized coordinates of a flexible body
δW_e	virtual work done by external forces
δW_{finer}	virtual work of inertial forces on the flexible body
δW_{iner}	virtual work of inertial forces on the rigid body
e	position error between body segment trajectories of inverse and forward dynamics
E	Young's modulus
f	smooth transition function
F	force
$F_{passive}$	force in the passive Hill muscle model component
$\mathbf{F}_e$	vector of external forces
$\mathbf{F}_{finer}$	vector of inertial forces in flexible multibody formulation
$\overline{\mathbf{G}}$	transformation matrix relating the time derivatives of angular parameters with the angular velocity vector
$\dot{\overline{\mathbf{G}}}$	first time derivative of the transformation matrix relating the time derivatives of angular parameters with the angular velocity vector
HU	voxel value expressed in Hounsfield units
I	integral coefficient in the PID controller model
$\mathbf{I}$	identity matrix
k	passive muscle stiffness
K	contact stiffness
$\mathbf{K}$	stiffness matrix of a flexible body
L_{curr}	current (instantaneous) length of muscle
L_{free}	free length of the muscle at rest when it is removed from the body

M	torque
$\mathbf{M}$	generalized inertia matrix
$\mathbf{M}_f$	generalized inertia matrix of a flexible body
n	exponent parameter in contact definition
N	total number of time steps
$\mathbf{p}$	vector of modal coordinates
$\dot{\mathbf{p}}$	vector of modal velocities
$\ddot{\mathbf{p}}$	vector of modal accelerations
P	proportional coefficient in the PID controller model
$\mathbf{q}$	vector of generalized coordinates of a rigid body
$\dot{\mathbf{q}}$	vector of generalized velocities of a rigid body
$\ddot{\mathbf{q}}$	vector of generalized accelerations of a rigid body
$\mathbf{q}_f$	vector of generalized coordinates of a flexible body
$\ddot{\mathbf{q}}_f$	vector of generalized acceleration of a flexible body
$\mathbf{Q}_e$	vector of generalized forces applied to a rigid body
$\mathbf{Q}_{fe}$	vector of generalized forces applied to a flexible body
$\mathbf{Q}_{finer}$	vector of generalized inertial forces of flexible body
$\mathbf{Q}_{fv}$	quadratic velocity vector of a flexible body
$\mathbf{Q}_{iner}$	vector of generalized inertial forces of rigid body
$\mathbf{Q}_v$	quadratic velocity vector of a rigid body
r_x	x component of the global position vector
r_y	y component of the global position vector
r_z	z component of the global position vector
$\mathbf{r}$	global position vector for a point in a body
$\dot{\mathbf{r}}$	global velocity vector for a point in a body
$\ddot{\mathbf{r}}$	global acceleration vector for a point in a body
R_x	x component of the vector defining the position of a local coordinate system
R_y	y component of the vector defining the position of a local coordinate system
R_z	z component of the vector defining the position of a local coordinate system
$\mathbf{R}$	vector defining the position of a local coordinate system
$\dot{\mathbf{R}}$	vector defining the velocity of a local coordinate system
$\ddot{\mathbf{R}}$	vector defining the acceleration of a local coordinate system
sign	mathematical *signum* function
s	penetration depth in contact formulation
$\dot{s}$	penetration velocity in contact formulation
s_{max}	limit penetration depth in contact formulation

t	time
$\bar{u}_x$	x component of the vector for point position in the local coordinate system
$\bar{u}_y$	y component of the vector for point position in the local coordinate system
$\bar{u}_z$	z component of the vector for point position in the local coordinate system
$\overline{\mathbf{u}}$	vector of point position in the local coordinate system
$\overline{\mathbf{u}}_f$	vector expressing point position in the local coordinate system on the flexible body with respect to the position of the point in undeformed state of the body
$\overline{\mathbf{u}}_{fo}$	vector expressing position of a point on a flexible body with respect to the local coordinate system
$\overline{\mathbf{u}}_o$	vector of point position in the local coordinate system on the flexible body in undeformed state
$\dot{\overline{\mathbf{u}}}$	first time derivative of the vector of point position in the local coordinate system
$\dot{\overline{\mathbf{u}}}_{fo}$	first derivative with respect to time of the vector expressing position of a point on a flexible body with respect to the local coordinate system
$\tilde{\overline{\mathbf{u}}}$	skew-symmetric matrix of the position vector expressed in the local coordinate system
$\tilde{\overline{\mathbf{u}}}_{fo}$	skew-symmetric matrix representation of the $\overline{\mathbf{u}}_{fo}$ vector
v	relative normal velocity of a contact pair
v_d	dynamic friction transition velocity in contact model
v_s	stiction transition velocity in contact model
V	volume
x	x axis of the global coordinate system
$\mathrm{x_l}$	x axis of the local coordinate system
x	x axis coordinate
x_1	x axis coordinate of the first point
x_2	x axis coordinate of the second point
x_f	x axis coordinate of a point of a body in forward dynamics
x_i	x axis coordinate of a point of a body in inverse dynamics
y	y axis of the global coordinate system
$\mathrm{y_l}$	y axis of the local coordinate system
y_1	y axis coordinate of the first point
y_2	y axis coordinate of the second point
y_f	y axis coordinate of a point of a body in forward dynamics
y_i	y axis coordinate of a point of a body in inverse dynamics

z	z axis of the global coordinate system
z_l	z axis of the local coordinate system
z_f	z axis coordinate of a point of a body in forward dynamics
z_i	z axis coordinate of a point of a body in inverse dynamics

Greek symbols

α_c	current angle
α_t	target angle
ε	strain
$\hat{\varepsilon}$	strain rate
$\boldsymbol{\theta}$	vector of rotational parameters of a body
$\dot{\boldsymbol{\theta}}$	first time derivative of the vector of rotational parameters of a body
$\ddot{\boldsymbol{\theta}}$	second time derivative of the vector of rotational parameters of a body
$\boldsymbol{\lambda}$	vector of Lagrange multipliers
μ	friction coefficient
μ_d	dynamic friction coefficient
μ_s	static friction coefficient
με	microstrain unit
ρ	apparent density
σ	physiological cross-sectional area
$\boldsymbol{\Phi}$	modal matrix
$\bar{\boldsymbol{\omega}}$	angular velocity vector represented in the body coordinate frame
$\tilde{\bar{\boldsymbol{\omega}}}$	skew-symmetric matrix of the rotation velocity vector

1 Introduction

The skeleton can be considered a mechanical structure of the human body. It allows transmitting the loads generated by the muscular system, but it also shields internal organs, produces blood cells and serves as storage for calcium and phosphor ions. It is thus important to keep it healthy.

One of the most severe bone diseases in humans is osteoporosis. It is a silent disease with no visible symptoms, and research is being carried out to develop radiation-free methods of early diagnosis (Bediz et al., 2010). Osteoporosis is a disease characterized by decreased bone mass and a micro-level degeneration of trabecular bone tissue and thinning of cortical bone. In healthy bone, the trabecular structure is rich and forms only small pores (Figure 1a). In contrast, when the bone becomes osteoporotic, the pores increase in size, and the trabecular structure becomes thinner, thus reducing the whole bone loading capacity (Figure 1b). Osteoporosis increases bone fragility and consequently introduces a fracture risk (WHO, 1994).

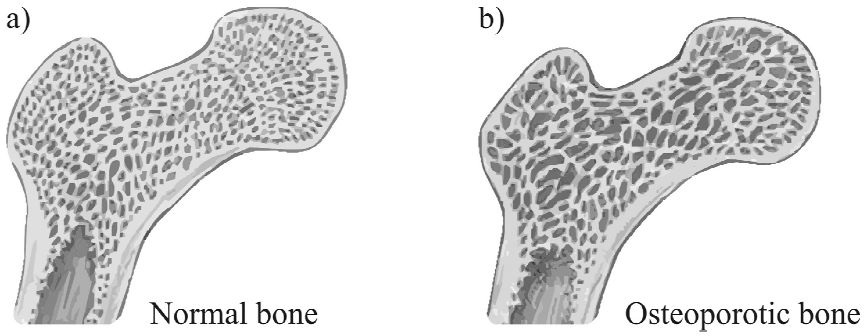

Figure 1. Comparison of normal and osteoporotic bone structures

The absolute numbers and age-specific incidence rates of osteoporotic fractures have clearly increased worldwide in recent decades, and without population level intervention, the increasing trend is likely to continue, creating a true public health problem for society (Kannus et al., 2002). For example, the number of hip fractures in Finnish people aged 50 or more increased more than threefold between 1970 and 1997 (Kannus et al., 1999). The change in the incidence rate observed during this time is presented in Figure 2. Although there are several risk factors that affect fracture development, bone strength is one of the primary predictors (Keyak et al., 1997); thus, for preventive and

treatment purposes, the ultimate goal is to reduce the risk of fractures by increasing or maintaining bone strength (Langsetmo et al., 2010).

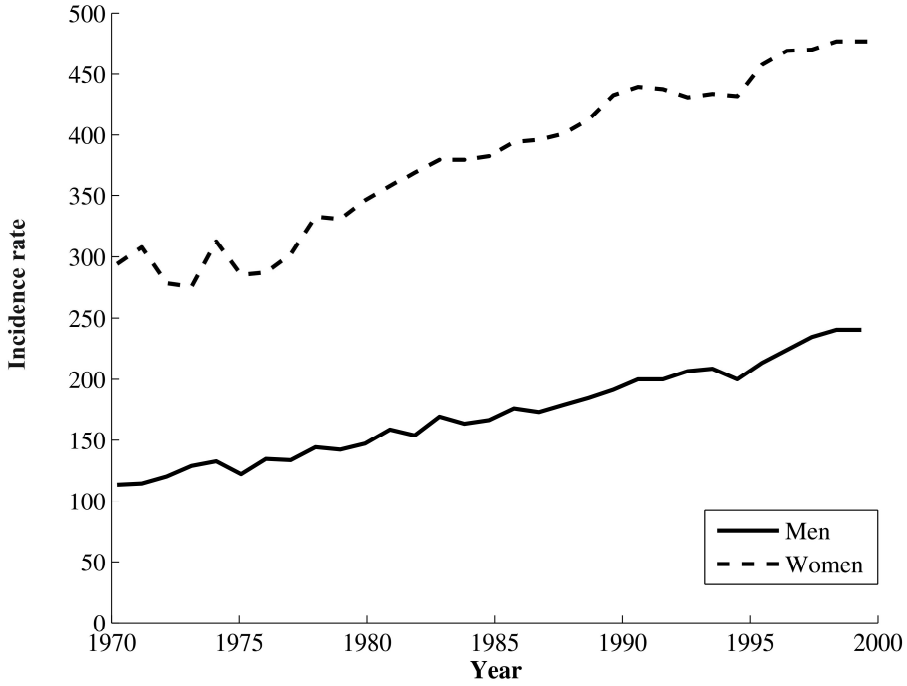

Figure 2. Incidence rate (per 100,000 persons) of hip fractures in Finland for women and men aged 50 years or older between 1970 and 1997 (Kannus et al., 1999)[1]

1.1 Bone strengthening potential of exercises

Various researches show that variable loading stimulates bone growth in both: animals (Liskova & Hert, 1971) and human (Shedd et al., 2007), (Lanyon & Rubin, 1984). There has been dispute over whether compressive or tensile strain stimulates bone growth (Sverdlova & Witzel, 2010). This question seems to remain unresolved still today. However, the load stimuli osteogenic effect has been proven.

Animal studies have demonstrated that loading magnitude, rate, number of loading cycles, and strain distribution determine the osteogenicity (i.e., the stimulus for adaptation) related to the magnitude of loading (Turner et al.,

[1] Figure was recreated from the data reported in (Kannus et al., 1999).

1995), (Lanyon, 1987). From the literature (Hadjidakis D. & Androulakis I., 2006), it can be concluded that bone growth and resorption are controlled in global and local way. Hormones are responsible for the global bone growth control and strain values affect the bone formation process locally. This hypothesis is depicted as a process flow chart in Figure 3. Since, intuitively, there is an association between ground reaction force and bone strain, it has been suggested that osteogenic index may be calculated from reaction forces (Whalen et al., 1988), (Turner & Robling, 2003). Consequently, a reaction force-based osteogenic index has been shown to differentiate successfully between the two exercises regimes. It enabled the differentiation of bone responses in human studies (von Stengel et al., 2005), (von Stengel et al., 2007).

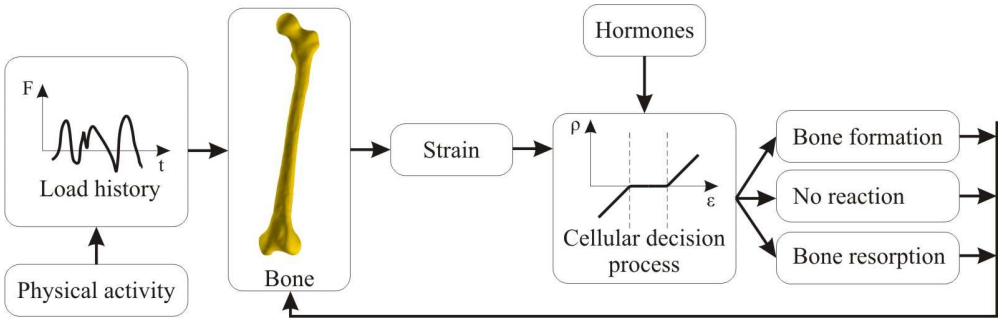

Figure 3. Bone growth and resorption control process with the load history dependent on the type of physical activity

In the absence of transient impact forces, young adults are able to produce forces of up to approximately six times the body weight (Ishikawa et al., 2005). Transient impact forces, caused by the body landing on the ground, easily double the ground reaction forces (Perttunen et al., 2000). In fact, ground reaction forces greater than 10 times the body weight are produced in daily activities by postmenopausal women (Vainionpää et al., 2007), (Jämsä et al., 2006), (Vainionpää et al., 2006). Transient impact force spikes result in high loading magnitudes. Moreover, the loading rate is much higher than when impact force spikes are not present. This raises the question of whether bones can be expected to be loaded substantially in the absence of transient impact force spikes. Several studies have shown that with transient impact force spikes, bones will be loaded enough to respond osteogenically to the loading (Heinonen et al., 1996), (Vainionpää et al., 2005), and there is an animal study

clearly indicating that transient force spikes do load bones substantially (Järvinen et al., 1998). Nevertheless, bone gains are achievable in the absence of transient impact spikes in animals (Umemura et al., 2002), (Rubin & Lanyon, 1984); however, this has not yet been confirmed in humans.

While no data is available on humans, strain distribution and loading from unusual directions have been shown to affect the osteogenic response in animals (Rubin & Lanyon, 1984). Some data supporting that effect was obtained from bone cross section images taken from athletes, which showed direction specific differences between those qualitatively subjected to typical (i.e., sagittal plane) and untypical (i.e., diverse loading directions) loading environments (Nikander et al., 2009b). The available *in-vivo* bone strain literature offers little help, as estimating strain distribution requires measuring bone strain around a cross section.

Osteogenic response in animals has been shown to be a function of loading cycle number (Rubin & Lanyon, 1984). However, the positive effect of increasing loading cycles appears to level off relatively rapidly (Turner, 1998). Cross-sectional bone studies of athletes appear to suggest an advantageous bone effect at distal parts of lower extremities (Nikander et al., 2009a), (Wilks et al., 2009). Interestingly, however, *in-vivo* measurements have shown that bone strain may also be expected to increase with increasing loading cycles in endurance types of exercises (Milgrom et al., 2007), and it remains unclear whether the bone gains are actually the effect of increased bone strain in response to muscle exhaustion or due to the high number of loading cycles. Accumulation of micro-damage and subsequent remodeling has been suggested as a possible mechanism responsible for expecting osteogenic response in association with an extensive number of loading cycles (Whalen et al., 1988).

1.2 Human bone endurance

Human bone ultimate strength is about 120 MPa, which is around half the ultimate strength of titanium and three times the ultimate strength of pinewood. Bones can withstand a significant amount of load over short periods. However, as in any mechanical structure, bones can fail by fatigue. Everyday movement and activity level determines the various ways bones are loaded, that is, their loading histories. The cortical bone fails in bending after 10^3–10^5 loading cycles

with strain ranges of 5,000–10,000 με (Carter et al., 1981). Under uniaxial tension at the strain amplitude of around 3,000 με, the bone can withstand up to one million cycles. Reducing the strain amplitude by half will prevent failure even after 37 million loading cycles (Schaffler et al., 1990).

In addition to loading cycles, the age of the bone influences remarkably the ultimate bone strength and thus fatigue life. Normally, human bones grow in young adult life until the age of 30, reaching the peak mass between the ages of 25 and 30 (Bechard et al., 2008). Then, bone mass begins to decrease gradually. At the age of 70, bone mass can be already less than 70 % of the young-adult bone mass (Riggs & Melton, 1995), (Smith & Gilligan, 1989). However people who continue to do hard physical work maintain bone density better than adults who become physically inactive. This decrease in bone strength is also caused by the weakening of muscles, which are the major source of bone loads. There is an effective bone strain threshold around 50–100 με below which bone material is lost. At this level, bone material is lost permanently, especially in the marrow proximity (Frost, 1987).

1.3 *In-vivo* strain measurements

The most accurate method of assessing bone strain is *in-vivo* strain gauge measurement. This method gives unbiased, subject-specific results; however, it requires installation and later removal of strain gauges by means of surgical intervention, as depicted in Figure 4. The gauges need to be bonded to the bone to perform accurate measurements. Originally, gauges were attached using cyanoacrylate adhesive, which is not Food and Drug Administration approved for implantation in humans. Only in 1997, a technical note was published proving the use of polymethylmethacrylate, which is an approved substance (Hoshaw et al., 1997). The medical procedure requires the installation bone site to be accessible directly, which restricts the method to superficial sites only. In addition this measurement method confines strain assessment to in-plane strain. For the above-mentioned reasons, use of the strain gauge measurement method is largely restricted to scientific research. Moreover, from an ethical point of view, this method is at least undesirable and ambiguous. Nevertheless, the results of strain gauge measurements are valuable as a source of reference data for the validation of the newer strain estimation methods based on computer simulations.

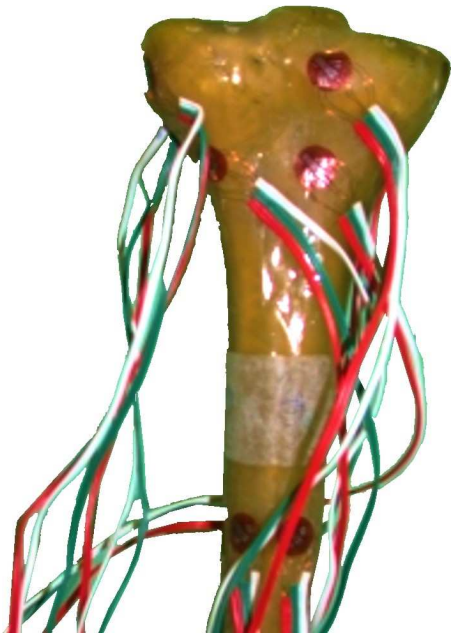

Figure 4. Strain gauge installation on cadaveric human tibia[2]

The first *in-vivo* strain measurements were performed by Lanyon (Lanyon et al., 1975). The experiment was directed at measurement, while walking of tibial in-plane strain at the anteromedial site. The subsequent work of Burr was dedicated to measuring strain resulting from vigorous activity (Burr et al., 1996). Those measurements revealed the observed extremes of bone strain. Milgrom added jumping to the list of exercise conditions providing strain measurement data for the tibia (Milgrom et al., 1998). Strain measurements were also performed on the femur; for instance, Aamodt measured tensile femoral strain at the proximal lateral site (Aamodt et al., 1997). In 2006, the effect of muscle fatigue on tibial strain was studied by Milgrom, who confirmed the clinical observation of the stress fractures that often result from muscle fatigue (Milgrom et al., 2007). Post fatigue strain increased by 11 to 29 % depending on physical activity. This indicates that stress fractures are caused by mechanical loading and are not the result of metabolic pathology.

Bone fatigue has been observed frequently in military recruits. The phenomenon was studied extensively to find the underlying cause of the

[2] Base image source:
http://www.biomedtown.org/biomed_town/LHDL/Reception/collection/StrainGauges

discrepancies between model predictions of bone fatigue life and real-life experience (Milgrom et al., 1985). Similarly, Beck investigated gender differences and their effect on stress fractures of the bone (Beck et al., 2000). In the study, Dual-energy X-ray Absorptiometry (DXA) measurements were used to quantify bone rigidity, thus instead of making direct strain measurements, a statistical analysis was performed on the effects of bone overstrain. The analysis revealed that people who suffered from stress fracture usually also had smaller muscles. The conclusion was drawn that the shielding effect of muscles is important in extreme loading conditions. It was also shown that people with stress fractures had lower body mass on average and could do considerably fewer sit-ups than those who did not suffer skeletal fractures. An animal study seems to confirm that result as bone strain measured *in-vivo* increased by 26–35 % with muscle fatigue (Yoshikawa et al., 1994).

1.4 The motivation for computational models

Since strain is arguably the bottom line for bone adaptation (Turner, 1998), (Lanyon, 1987), it would help in designing osteogenic interventions, if local bone strain throughout the bone cross section were known at clinically interesting bone sites for a wide range of exercises. Most commonly, *in-vivo* bone strain measurements are taken from superficial bone sites, and therefore measuring many of the clinically interesting bone sites *in-vivo* is not feasible. Although the literature speaks of at least one case in which measurements were taken from a bone site overlaid by muscle (Aamodt et al., 1997). Dynamic model-based approaches provide a reasonable alternative for estimating the skeletal loading for a given bone site subject to dynamic movement. Relatively little strain measurement data for dynamic movement is found currently in the literature, although, estimates for bone strain in walking subjects were made by Al Nazer in 2008 (Al Nazer et al., 2008a), (Al Nazer et al., 2008b). According to earlier studies (Milgrom et al., 1985), 40 % of fractures occurred at the midshaft of the tibia, a result that suggests the need for numerical studies to determine loading conditions at that particular bone site.

Computational models of the human musculoskeletal system can be used to estimate site-specific loading at, for example, muscle insertion points, resulting from physical activity. The models presented in this thesis allow investigating bone strain and muscle activity on a subject level. This makes it possible to

investigate the influence of exercise on the bone strengthening processes of a specific subject. Providing information about which bones and bone sites are particularly affected. Moreover, joint load estimation allows for determining if the exercise does not cause joint overload. By extending the use of the approach presented here, exercise optimization could be performed focusing on maximizing bone-loading amplitudes during exercise and at the same time keeping joint loads within safe limits. This offers the possibility of exercise optimization in terms of bone strengthening with minimal joint loading that could be used in preparing exercise programs for different age groups. In exercise equipment design, new factors could be added to the optimization procedure, resulting in not only safer but also more effective exercise, both in terms of muscle and bone strengthening.

1.5 Scientific contribution of the work

Simulation models based on the flexible multibody dynamics approach are presented in this work. All the models are solved utilizing forward dynamics and an active muscle models control system. The motion in the simulations represents natural motion of the human subjects participating in motion capture experiments. Furthermore, the models built are subject-specific. Strain and joint load results are used to estimate the osteogenity of the physical activities addressed. The simulation models presented in this work represent several improvements to earlier studies. The flexible bone models account for inhomogeneous material properties, and there are meaningful differences between the homogeneous and inhomogeneous material models based on Computed Tomography (CT). Tibia bone models contain macro level cortical and trabecular bone material models. The femur bone model for walking, due to its fine mesh, allowed for complete differentiation between cortical and trabecular bone models. Relationships between material parameters and computed tomography voxel values (a voxel is the three-dimensional analog of a pixel) were extended from isotropic, which can be found in the literature (Dalstra et al., 1993), (Dong & Guo, 2004), to orthotropic.

This thesis presents bone strain and joint loads observed during four typical gym exercises: the leg press, knee flexion, knee extension and squatting. The results allowed comparing the effects of exercise on the knee and hip loading bases with respect to strain induced in the tibia. The tibia model used in the

study was built based on computed tomography images acquired from the subject. This allowed accounting for inhomogeneous material properties within the bone. In addition to gym exercises, walking was studied, and strain data at the tibia and femoral neck were acquired. The relationship of the orthotropic material properties and the computed tomography values for the femur were developed based on available literature.

To the knowledge of author, most of the presented gym exercise simulations, with bone strain as the focus, are the first of their kind. The new knowledge for bone strain during exercise allows conclusions to be drawn about the type of exercise most beneficial in terms of bone strengthening. The results may be immediately used to optimize exercise equipment to better apply bone-strengthening forces, and at the same time provide guidelines for joint loading limits.

Furthermore, bone strain data, taken from healthy subjects while they exercise, can be used as a reference for implant design. Joint prostheses should be designed so loading on the bones does not differ considerably with respect to a healthy individual. This provides increased comfort for the patients and may reduce the need for follow-up surgical interventions. Currently, dynamic bone loading data is limited to strain gauge measurements taken from recruited military personnel during exercise and while walking. This thesis adds to the existing body of data by including new strain estimation results computed for volunteer subject carrying out squat, leg press, knee flexion, and knee extension exercises.

While this dissertation was being prepared, six scientific journal articles were produced by the author and associates (Al Nazer et al., 2008b), (Al Nazer et al., 2011), (Kłodowski et al., 2011b), (Rantalainen et al., 2011), (Kłodowski et al., 2011a), and (Kłodowski et al., 2012). In addition, the author co-edited one chapter of a book entitled “Theoretical Biomechanics”. The chapter was devoted to numerical estimation methods for bone strain (Rantalainen & Kłodowski, 2011).

2 Materials and methods

2.1 Rigid body dynamics of multibody systems

Computational models of mechanical systems are based on mathematical models that formulate the laws of physics in a discrete time domain. A mechanical system consists of a number of mechanical components, for which the laws of physics can be formulated, which can be connected via joints or force relations to form a working system. In real systems, joints represent contact between bodies. However, because mathematical models of contact are very complex, simpler kinematic models are often used to represent contact interactions in numerical models.

To simplify the mathematical model further, not every physical part of a mechanical system is represented with a separate numerical description. Instead, components that are fixed together in the physical system are usually represented as a single body in the simulation. Moreover, components with relatively small inertia and outside the scope of investigation can be neglected, e.g. fasteners. An example of system discretization with multibody system approach is depicted in Figure 5. In the example, hydraulic drilling machine components are represented as rigid bodies with mass properties and inertia. The components are connected via kinematic joints. External forces are applied to model as the reaction forces between the drill and the ground as well as the interaction between the ground and the chassis.

The important issue of modeling comes up at this point; the modeler has to decide on the level of detail. In this case, the level of detail is reduced, but still sufficient to study the overall behavior of the machine. Accordingly, the chassis is considered a single body, while in reality it consists of a large number of moving parts including bearings, wheels, and chains. The level of detail determines the complexity of the model and at the same time its accuracy.

Mathematical modeling of the system is possible knowing the discretization of the multibody model (Shabana, 2005), the connections between bodies, the masses and geometric properties, and the externally applied forces. To describe the system, a global coordinate system must be established, and the initial configuration of the system must be described with respect to the global

coordinate system. Individual inertial properties and constraints between bodies are difficult to describe directly in the global coordinate system.

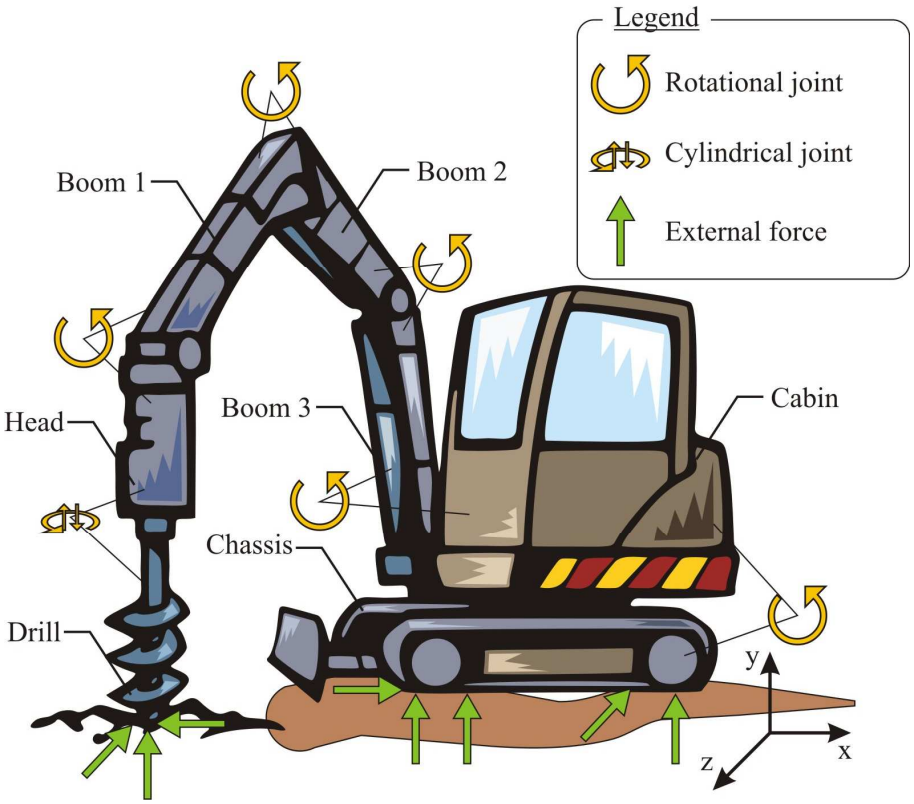

Figure 5. Modeling a hydraulic drilling machine as a rigid multibody system – External forces, joints, bodies and global coordinate system are depicted (actuators are not shown in the picture).

For that reason, local coordinate systems are often introduced. The local coordinate systems are associated with the bodies, so that each receives its own reference frame as depicted in Figure 6.

In this study, coordinates expressed in local coordinate systems are denoted with a superposed bar. The global position for a point in a rigid body in the global coordinate system can be then described as follows.

$$\mathbf{r} = \mathbf{R} + \mathbf{A}\bar{\mathbf{u}} \tag{1}$$

The symbol **r** represents the global position vector, which has three components (r_x, r_y and r_z), corresponding to the location of the point in the global coordinate system (x, y, z). The vector $\mathbf{R} = \begin{bmatrix} R_x & R_y & R_z \end{bmatrix}^T$ defines the position of the local coordinate system with respect to the global coordinate system, and $\bar{\mathbf{u}} = \begin{bmatrix} \bar{u}_x & \bar{u}_y & \bar{u}_z \end{bmatrix}^T$ defines the position vector for a point in the body expressed in the local coordinate system (x_l, y_l, z_l). Matrix **A** is the rotation matrix specifying the orientation of the local coordinate system with respect to the global coordinate system. Figure 6 illustrates.

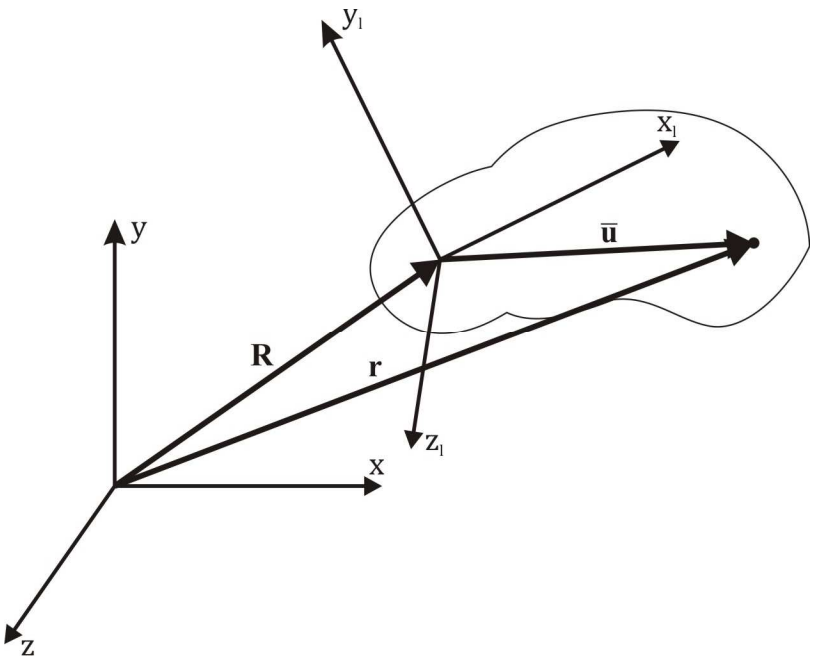

Figure 6. Description of the position for the point in a rigid body expressed in local (indicated by the l index) and global (x, y, z) coordinate systems

Deriving the rotation matrix for the three-dimensional case can be accomplished by combining three rotation matrices describing successive rotations. Single-axis rotation matrices for the three-dimensional case can be expressed in a number of ways, which have been discussed in detail (Kuipers, 2002).

Generalized coordinates have been used to describe the configuration of the system relative to the global coordinate system. They uniquely define the state

of the multibody system at any instant in time, and they can be divided into dependent and independent coordinates. The number of independent generalized coordinates is equal to the number of the degrees of freedom of the multibody system. On the other hand, the number of dependent coordinates is related to the number of constraint equations. The vector of generalized coordinates can be represented as $\mathbf{q}$. Similarly, generalized angular and translational accelerations are combined into a vector denoted $\ddot{\mathbf{q}}$, and the vector of generalized velocities is $\dot{\mathbf{q}}$. The equations of motion can be derived beginning with derivation of the velocity vector $\dot{\mathbf{r}}$, which is the first derivative with respect to time of equation (1).

$$\dot{\mathbf{r}} = \dot{\mathbf{R}} + \dot{\mathbf{A}}\bar{\mathbf{u}} + \mathbf{A}\dot{\bar{\mathbf{u}}} \tag{2}$$

The vector defining the velocity of a local coordinate system is $\dot{\mathbf{R}}$, the first derivative with respect to time of the rotation matrix is $\dot{\mathbf{A}}$. In case of a rigid body, the time derivative of a vector of point position $\dot{\bar{\mathbf{u}}}$ is equal to zero. The term $\dot{\mathbf{A}}\bar{\mathbf{u}}$ can be expressed as follows.

$$\dot{\mathbf{A}}\bar{\mathbf{u}} = \mathbf{A}(\bar{\boldsymbol{\omega}} \times \bar{\mathbf{u}}) = -\mathbf{A}(\bar{\mathbf{u}} \times \bar{\boldsymbol{\omega}}) = -\mathbf{A}\tilde{\bar{\mathbf{u}}}\bar{\boldsymbol{\omega}} \tag{3}$$

The skew-symmetric matrix representation of vector $\bar{\mathbf{u}}$ is denoted $\tilde{\bar{\mathbf{u}}}$. The first derivative with respect to time of the rotation matrix $\dot{\mathbf{A}}$ can also be expressed as:

$$\dot{\mathbf{A}} = \mathbf{A}\tilde{\bar{\boldsymbol{\omega}}}, \tag{4}$$

where $\tilde{\bar{\boldsymbol{\omega}}}$ is a skew-symmetric matrix representation of angular velocity vector $\bar{\boldsymbol{\omega}}$, which can be written as follows.

$$\bar{\boldsymbol{\omega}} = \bar{\mathbf{G}}\dot{\boldsymbol{\theta}} \tag{5}$$

The transformation matrix $\bar{\mathbf{G}}$ links the first time derivatives of the orientation parameters and generalized angular velocities expressed in the local coordinate system. Matrix $\bar{\mathbf{G}}$ depends on the selected rotational coordinates of the body.

The vector for generalized angular velocity is denoted $\dot{\boldsymbol{\theta}}$. Inserting equations (3) and (5) into equation (2), the velocity vector $\dot{\mathbf{r}}$ can be also expressed as follows.

$$\dot{\mathbf{r}} = \dot{\mathbf{R}} - \mathbf{A}\tilde{\bar{\mathbf{u}}}\bar{\mathbf{G}}\dot{\boldsymbol{\theta}} \tag{6}$$

The velocity vector $\dot{\mathbf{r}}$ can be expressed in terms of generalized velocities as follows.

$$\dot{\mathbf{r}} = \begin{bmatrix}\mathbf{I} & -\mathbf{A}\tilde{\bar{\mathbf{u}}}\bar{\mathbf{G}}\end{bmatrix}\begin{bmatrix}\dot{\mathbf{R}} \\ \dot{\boldsymbol{\theta}}\end{bmatrix} \tag{7}$$

The identity matrix is **I**. The time derivative of equation (7), which is the global acceleration vector, $\ddot{\mathbf{r}}$ can be computed, leading to the following expression:

$$\ddot{\mathbf{r}} = \begin{bmatrix}\mathbf{I} & -\mathbf{A}\tilde{\bar{\mathbf{u}}}\bar{\mathbf{G}}\end{bmatrix}\begin{bmatrix}\ddot{\mathbf{R}} \\ \ddot{\boldsymbol{\theta}}\end{bmatrix} + \begin{bmatrix}\mathbf{0} & -\mathbf{A}\tilde{\bar{\boldsymbol{\omega}}}\tilde{\bar{\mathbf{u}}}\bar{\mathbf{G}} - \mathbf{A}\tilde{\bar{\mathbf{u}}}\dot{\bar{\mathbf{G}}}\end{bmatrix}\begin{bmatrix}\dot{\mathbf{R}} \\ \dot{\boldsymbol{\theta}}\end{bmatrix}, \tag{8}$$

where $\ddot{\mathbf{R}}$ is the vector defining the acceleration of a local coordinate system, and $\ddot{\boldsymbol{\theta}}$ is the second time derivative of the vector of rotational parameters of a body. The equation of motion can be derived using the principle of virtual work. The virtual displacement needed in the concept of virtual work can be expressed in terms of generalized coordinates as follows.

$$\delta\mathbf{r} = \frac{\partial \mathbf{r}}{\partial \mathbf{q}}\delta\mathbf{q}, \tag{9}$$

where $\delta\mathbf{r}$ represents the virtual displacements of global position vector, and $\delta\mathbf{q}$ stands for virtual displacements of generalized coordinates. Using the virtual displacements, the virtual work of inertial forces δW_{iner} can be derived using Newton's second law and d'Alembert's principle as follows.

$$\delta W_{iner} = \int_V \rho\ddot{\mathbf{r}}^T \frac{\partial \mathbf{r}}{\partial \mathbf{q}}\delta\mathbf{q}dV, \tag{10}$$

where V is the volume, and ρ is the density of the rigid body. Consequently, the generalized inertial forces $\mathbf{Q}_{iner}$ can be expressed in the following way.

$$\mathbf{Q}_{iner} = \int_V \rho \left[\begin{bmatrix} \mathbf{I} \\ -\bar{\mathbf{G}}^T \tilde{\bar{\mathbf{u}}}^T \mathbf{A}^T \end{bmatrix} \begin{bmatrix} \mathbf{I} & -\mathbf{A}\tilde{\bar{\mathbf{u}}}\bar{\mathbf{G}} \end{bmatrix} \right] \ddot{\mathbf{q}} + \begin{bmatrix} \mathbf{I} \\ -\bar{\mathbf{G}}^T \tilde{\bar{\mathbf{u}}}^T \mathbf{A}^T \end{bmatrix} \left(-\mathbf{A}\tilde{\bar{\boldsymbol{\omega}}}\tilde{\bar{\mathbf{u}}}\bar{\mathbf{G}}\dot{\theta} - \mathbf{A}\tilde{\bar{\mathbf{u}}}\dot{\bar{\mathbf{G}}}\dot{\theta} \right) dV \tag{11}$$

The generalized accelerations vector of the rigid body is $\ddot{\mathbf{q}}$. Using the above equation, the mass matrix $\mathbf{M}$ and the quadratic velocity vector $\mathbf{Q}_v$ can be formulated as equations (12) and (13).

$$\mathbf{M} = \int_V \rho \begin{bmatrix} \mathbf{I} & -\mathbf{A}\tilde{\bar{\mathbf{u}}}\bar{\mathbf{G}} \\ -\bar{\mathbf{G}}^T \tilde{\bar{\mathbf{u}}}^T \mathbf{A}^T & \bar{\mathbf{G}}^T \tilde{\bar{\mathbf{u}}}^T \tilde{\bar{\mathbf{u}}} \bar{\mathbf{G}} \end{bmatrix} dV \tag{12}$$

$$\mathbf{Q}_v = \int_V \rho \begin{bmatrix} \mathbf{A}\tilde{\bar{\boldsymbol{\omega}}}\tilde{\bar{\boldsymbol{\omega}}}\tilde{\bar{\mathbf{u}}} - \mathbf{A}\tilde{\bar{\mathbf{u}}}\dot{\bar{\mathbf{G}}}\dot{\theta} \\ -\bar{\mathbf{G}}\tilde{\bar{\mathbf{u}}}^T \tilde{\bar{\boldsymbol{\omega}}}\tilde{\bar{\boldsymbol{\omega}}}\tilde{\bar{\mathbf{u}}} + \bar{\mathbf{G}}\tilde{\bar{\mathbf{u}}}^T \tilde{\bar{\mathbf{u}}}\dot{\bar{\mathbf{G}}}\dot{\boldsymbol{\theta}} \end{bmatrix} dV \tag{13}$$

Examining equations (11), (12), and (13); one can conclude the generalized inertial forces may be expressed in terms of the mass matrix and quadratic velocity vector as follows.

$$\mathbf{Q}_{iner} = \mathbf{M}\ddot{\mathbf{q}} + \mathbf{Q}_v \tag{14}$$

Virtual work δW_e done by external forces $\mathbf{F}_e$ can be derived in the same way as the virtual work of inertial forces from equation (10). Accordingly, the vector of generalized external forces $\mathbf{Q}_e$ can be obtained. In equilibrium, the virtual work done by external forces can be seen to be equal to the virtual work of inertial forces. Likewise, the virtual work equilibrium, that is, the force equilibrium can be written in this manner:

$$\mathbf{Q}_{iner}^T \delta\mathbf{q} = \mathbf{Q}_e^T \delta\mathbf{q} \tag{15}$$

Using the augmented formulation, constraint equations $\mathbf{C}(\mathbf{q}, t)$, can be added to the equation of motion using a vector of Lagrange multipliers. This leads to the following extended form of equations of motion.

$$\mathbf{M}\ddot{\mathbf{q}} + \mathbf{Q}_v - \mathbf{Q}_e - \mathbf{C}_q^T \boldsymbol{\lambda} = \mathbf{0} \tag{16}$$

The Jacobian matrix $\mathbf{C}_q$ can be obtained by differentiating the constraint equations with respect to the generalized coordinates. In equation (16), the acceleration of generalized coordinates and Lagrange multiplier vector are unknown, making it impossible to solve them solely with equation (16). The additional information needed to solve the equation can be obtained from the constraint equations. Finally, the equation of motion for the multibody system can be written as follows.

$$\begin{cases} \mathbf{M}\ddot{\mathbf{q}} - \mathbf{C}_q^T\boldsymbol{\lambda} = \mathbf{Q}_e - \mathbf{Q}_v \\ \mathbf{C}(\mathbf{q}, t) = \mathbf{0} \end{cases} \tag{17}$$

The constraint equations define the relations between generalized coordinates that are coupled. For instance, a spherical joint implies no relative translation of two bodies at the joint.

2.2 Flexible multibody dynamics

To account for flexibility, the kinematic description for the position of a point in the body must be extended. The point position vector for a flexible body needs an additional term, which represents body deformation. This term is added by partitioning the vector $\bar{\mathbf{u}}$. The resulting vector $\bar{\mathbf{u}}_o$corresponds to the undeformed point position, and $\bar{\mathbf{u}}_f$ corresponds to the displacement of a point from its original location on the body due to elastic deformation. Equation (18) represents the updated equation (1) for flexible bodies.

$$\mathbf{r} = \mathbf{R} + \mathbf{A}(\bar{\mathbf{u}}_o + \bar{\mathbf{u}}_f) \tag{18}$$

Figure 7 represents the coordinate transformation expressed in equation (18). As suggested by Craig, the deformation of the flexible body $\bar{\mathbf{u}}_f$ can be approximated using the model reduction method as follows (Craig & Bampton, 1968).

$$\bar{\mathbf{u}}_f \cong \boldsymbol{\Phi}\mathbf{p} \tag{19}$$

The matrix of deformation modes is $\mathbf{\Phi}$, and $\mathbf{p}$ is the vector of modal coordinates. Thus, the vector of generalized coordinates in the flexible body case $\mathbf{q}_f$ can be described as follows.

$$\mathbf{q}_f = [\mathbf{q}^T \quad \mathbf{p}^T]^T \tag{20}$$

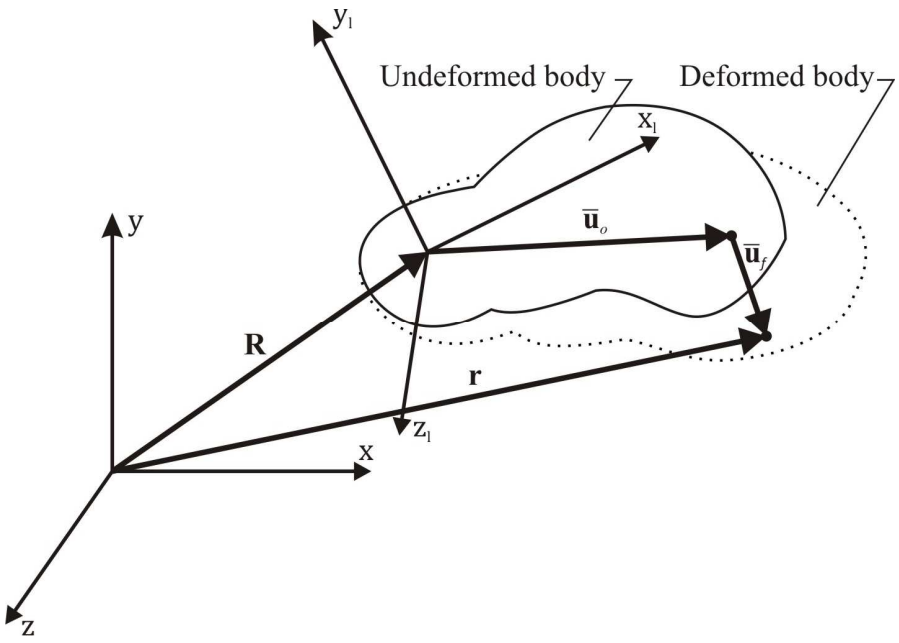

Figure 7. Relation between position description of a point in the flexible body in the local (indicated by the l index) and global (x, y, z) coordinate systems

The sum of vectors $\overline{\mathbf{u}}_o$ and $\overline{\mathbf{u}}_f$ in equation (18) can be denoted as $\overline{\mathbf{u}}_{fo}$. Velocity vector $\dot{\mathbf{r}}$ can be derived by differentiating equation (18) once with respect to time, yielding:

$$\dot{\mathbf{r}} = \dot{\mathbf{R}} + \dot{\mathbf{A}}\overline{\mathbf{u}}_{fo} + \mathbf{A}\dot{\overline{\mathbf{u}}}_{fo}, \tag{21}$$

where $\dot{\overline{\mathbf{u}}}_{fo}$ is the first time derivative of the $\overline{\mathbf{u}}_{fo}$ vector. The product $\dot{\mathbf{A}}\overline{\mathbf{u}}_{fo}$ can be expressed as follows.

$$\dot{\mathbf{A}}\overline{\mathbf{u}}_{fo} = \mathbf{A}(\bar{\boldsymbol{\omega}} \times \overline{\mathbf{u}}_{fo}) = -\mathbf{A}(\overline{\mathbf{u}}_{fo} \times \bar{\boldsymbol{\omega}}) = -\mathbf{A}\tilde{\overline{\mathbf{u}}}_{fo}\bar{\boldsymbol{\omega}}, \tag{22}$$

where $\bar{\boldsymbol{\omega}}$ can be expressed as in rigid multibody dynamics by equation (5), and $\tilde{\bar{\mathbf{u}}}_{fo}$ is a skew-symmetric matrix representation of the $\bar{\mathbf{u}}_{fo}$ vector.

Forces including elastic, internal and damping expressed in terms of generalized coordinates can be used to derive the equation of motion of a flexible multibody system. For that purpose, the principle of virtual work can be utilized. The inertial forces $\mathbf{F}_{finer}$ of a flexible body can be then expressed as the integral of the product of density ρ and the transpose of the vector of accelerations $\ddot{\mathbf{r}}$ over the volume of the flexible body V. By applying the concept of virtual displacement, the virtual work done by inertia forces can be expressed in this manner.

$$\delta W_{finer} = \int_V \rho \ddot{\mathbf{r}}^T \delta \mathbf{r} dV \tag{23}$$

The virtual displacements vector can be expressed in the following form.

$$\delta \mathbf{r} = \begin{bmatrix} \mathbf{I} & -\mathbf{A}\tilde{\bar{\mathbf{u}}}_{fo}\bar{\mathbf{G}} & \mathbf{A}\boldsymbol{\Phi} \end{bmatrix} \delta \mathbf{q}_f \tag{24}$$

Combining equations (23) and (24) yields this expression.

$$\delta W_{finer} = \int_V \rho \ddot{\mathbf{r}}^T \begin{bmatrix} \mathbf{I} & -\mathbf{A}\tilde{\bar{\mathbf{u}}}_{fo}\bar{\mathbf{G}} & \mathbf{A}\boldsymbol{\Phi} \end{bmatrix} dV \delta \mathbf{q}_f = \mathbf{Q}_{finer}^T \delta \mathbf{q}_f \tag{25}$$

Differentiating equation (21) once leads to a description of the acceleration vector $\ddot{\mathbf{r}}$.

$$\begin{aligned} \ddot{\mathbf{r}} = & \begin{bmatrix} \mathbf{I} & -\mathbf{A}\tilde{\bar{\mathbf{u}}}_{fo}\bar{\mathbf{G}} & \mathbf{A}\boldsymbol{\Phi} \end{bmatrix} \begin{bmatrix} \ddot{\mathbf{R}} \\ \ddot{\boldsymbol{\theta}} \\ \ddot{\mathbf{p}} \end{bmatrix} \\ & + \begin{bmatrix} \mathbf{0} & -\mathbf{A}\tilde{\bar{\boldsymbol{\omega}}}\tilde{\bar{\mathbf{u}}}_{fo}\bar{\mathbf{G}} - \mathbf{A}\tilde{\bar{\mathbf{u}}}_{fo}\dot{\bar{\mathbf{G}}} & 2\mathbf{A}\tilde{\bar{\boldsymbol{\omega}}}\boldsymbol{\Phi} \end{bmatrix} \begin{bmatrix} \dot{\mathbf{R}} \\ \dot{\boldsymbol{\theta}} \\ \dot{\mathbf{p}} \end{bmatrix} \end{aligned} \tag{26}$$

Combining equations (25) and (26) yields this expression for the vector of generalized inertial forces.

$$\mathbf{Q}_{finer} = \int_V \rho \left[\begin{bmatrix} \mathbf{I} \\ -\bar{\mathbf{G}}^T \tilde{\bar{\mathbf{u}}}_{fo}^T \mathbf{A}^T \\ \mathbf{\Phi}^T \mathbf{A}^T \end{bmatrix} \begin{bmatrix} \mathbf{I} & -\mathbf{A}\tilde{\bar{\mathbf{u}}}_{fo}\bar{\mathbf{G}} & \mathbf{A}\mathbf{\Phi} \end{bmatrix} \right] \ddot{\mathbf{q}}_f + \begin{bmatrix} \mathbf{I} \\ -\bar{\mathbf{G}}^T \tilde{\bar{\mathbf{u}}}_{fo}^T \mathbf{A}^T \\ \mathbf{\Phi}^T \mathbf{A}^T \end{bmatrix} \left(-\mathbf{A}\tilde{\bar{\boldsymbol{\omega}}}\tilde{\bar{\mathbf{u}}}_{fo}\bar{\mathbf{G}}\dot{\boldsymbol{\theta}} - \mathbf{A}\tilde{\bar{\mathbf{u}}}_{fo}\dot{\bar{\mathbf{G}}}\dot{\boldsymbol{\theta}} + 2\mathbf{A}\tilde{\bar{\boldsymbol{\omega}}}\mathbf{\Phi}\dot{\mathbf{p}} \right) dV \tag{27}$$

The mass matrix $\mathbf{M}_f$ and the quadratic velocity vector $\mathbf{Q}_{fv}$ in equation (27), are defined as follows.

$$\mathbf{M}_f = \int_V \rho \begin{bmatrix} \mathbf{I} & -\mathbf{A}\tilde{\bar{\mathbf{u}}}_{fo}\bar{\mathbf{G}} & \mathbf{A}\mathbf{\Phi} \\ -\bar{\mathbf{G}}^T \tilde{\bar{\mathbf{u}}}_{fo}^T \mathbf{A}^T & \bar{\mathbf{G}}^T \tilde{\bar{\mathbf{u}}}_{fo}^T \tilde{\bar{\mathbf{u}}}_{fo}\bar{\mathbf{G}} & -\bar{\mathbf{G}}^T \tilde{\bar{\mathbf{u}}}_{fo}^T \mathbf{\Phi} \\ \mathbf{\Phi}^T \mathbf{A}^T & -\mathbf{\Phi}^T \tilde{\bar{\mathbf{u}}}_{fo}\bar{\mathbf{G}} & \mathbf{\Phi}^T \mathbf{\Phi} \end{bmatrix} dV \tag{28}$$

$$\mathbf{Q}_{fv} = \int_V \rho \begin{bmatrix} \mathbf{A}\tilde{\bar{\boldsymbol{\omega}}}\tilde{\bar{\boldsymbol{\omega}}}\tilde{\bar{\mathbf{u}}}_{fo} - \mathbf{A}\tilde{\bar{\mathbf{u}}}_{fo}\dot{\bar{\mathbf{G}}}\dot{\boldsymbol{\theta}} - 2\mathbf{A}\tilde{\bar{\boldsymbol{\omega}}}\mathbf{\Phi}\dot{\mathbf{p}} \\ -\bar{\mathbf{G}}\tilde{\bar{\mathbf{u}}}_{fo}^T \tilde{\bar{\boldsymbol{\omega}}}\tilde{\bar{\boldsymbol{\omega}}}\tilde{\bar{\mathbf{u}}}_{fo} + \bar{\mathbf{G}}\tilde{\bar{\mathbf{u}}}_{fo}^T \tilde{\bar{\mathbf{u}}}_{fo}\dot{\bar{\mathbf{G}}}\dot{\boldsymbol{\theta}} - 2\bar{\mathbf{G}}\tilde{\bar{\mathbf{u}}}_{fo}^T \tilde{\bar{\boldsymbol{\omega}}}\mathbf{\Phi}\dot{\mathbf{p}} \\ \mathbf{\Phi}^T \tilde{\bar{\boldsymbol{\omega}}}\tilde{\bar{\boldsymbol{\omega}}}\tilde{\bar{\mathbf{u}}}_{fo} - \mathbf{\Phi}^T \tilde{\bar{\mathbf{u}}}_{fo}\dot{\bar{\mathbf{G}}}\dot{\boldsymbol{\theta}} - 2\mathbf{\Phi}^T \tilde{\bar{\boldsymbol{\omega}}}\mathbf{\Phi}\dot{\mathbf{p}} \end{bmatrix} dV \tag{29}$$

The concept of virtual work can be also applied to the elastic forces and externally applied forces in a similar manner as in the case of the inertial forces. After introducing constraint equations, the equation of motion takes the form of a differential equation.

$$\mathbf{M}_f \ddot{\mathbf{q}}_f + \mathbf{K}\mathbf{q}_f + \mathbf{C}_{fq}^T \boldsymbol{\lambda} = \mathbf{Q}_{fe} - \mathbf{Q}_{fv} \tag{30}$$

In the above equation $\mathbf{Q}_{fe}$ is the vector of generalized forces, $\mathbf{C}_{fq}^T$ is the constraint Jacobian matrix, $\boldsymbol{\lambda}$ is the vector of Lagrange multipliers of flexible body, and the generalized reaction forces are represented by the product $\mathbf{C}_{fq}^T \boldsymbol{\lambda}$. Index f is used to distinguish between rigid and flexible multibody formulation elements. The constraint equations $\mathbf{C}(\mathbf{q}_f, t)$ and equation (30) combine to form a set of Differential Algebraic Equations (DAE) which can be converted to Ordinary Differential Equations (ODE) to solve for the dynamic response of the multibody system forward in time.

2.3 Bone flexibility description and strain estimation

Bone deformation is small and in generally insignificant in terms of dynamic performance. For that reason, linear description of bone deformation can be successfully used in multibody simulations. There are two principal approaches to accounting for bone elasticity in multibody simulations. The first calculated deformation, and therefore strain, during post-processing based on the external forces acting on the bone. The second more directly implement a flexible bone description in the simulation (Geradin & Cardona, 2000). With the first method, there is a complete decoupling of flexibility from the mechanical simulation, which may increase error of the estimated strain values, especially during dynamic motion. On the other hand, integrating the flexible bone description, the second method, is more complex to implement and may result in longer simulation times.

Either way the strain values are obtained from deformation of the bone. By definition, strain is a relation between deformed and undeformed states. This implies that strain values obtained from simulation may be larger than those obtained *in-vivo*, where the undeformed, i.e. zero level strain values have to be assumed. Usually during *in-vivo* measurements, it is assumed that bone is undeformed when a subject is lying in the supine or prone positions or when seated with legs freely hanging, although the seated position will result in some strain related to suspending bone under its own weight. In both cases, strain will occur due to muscle tension and tendon resting load, which in simulations is already a non-zero load.

Two main types of finite element models for long bones are described in this section. The first type is the shell element model (Al Nazer et al., 2008a). The second one is based on the use of the solid element model. In both cases, modeling begins with a bone geometry description. The geometry can be either generic or obtained from medical imaging. The type of elements used for meshing determines the requirements for the geometrical model. The model based on shell elements requires just the cortical bone representation. Depending on the bone site, the modeler must decide whether uniform averaged thickness or variable cortical thickness should be applied. The significant problem with the shell model is that connections between elements of non-uniform thickness are unrealistic. Analogical problems exist when modeling a

beam of varying cross section with beam elements. Shell models offer an easy way to obtain in-plane surface strain values, however, they do not account for the trabecular bone loading capacity.

Solid finite element modeling allows for straightforward inclusion of inhomogeneous material properties in trabecular and cortical bone structures. It also allows for accurate volume meshing. However, the accuracy strongly depends on element size. To model cortical and trabecular bone separately, an element size of around 0.5 mm must be used at the distal regions of the bone. This increases the finite element model size considerably, and the resources needed to compute the model might exceed the capabilities of a desktop computer. For that reason, it is common to combine the trabecular and cortical structure models making acceptable the usage of an element size in the range of 3 to 7 mm (Al Nazer et al., 2008a). More information about optimal mesh size for tibia bone strain analysis can be found in a conference paper dedicated to convergence analysis for the mesh size used for a tibia in connection with the Craig-Bampton method (Kłodowski et al., 2011c). A comparison of element size and number of degrees of freedom for a tibia bone mesh is presented in Figure 8.

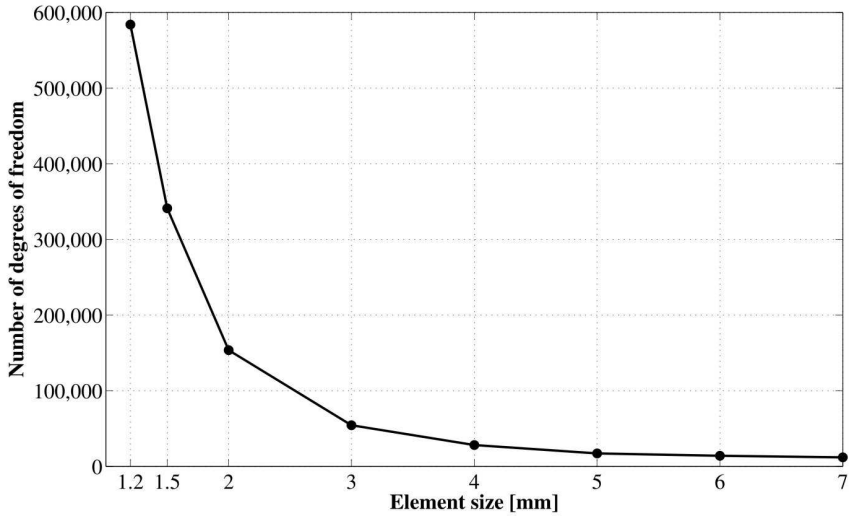

Figure 8. Comparison of tibia tetrahedral mesh size described as the number of degrees of freedom depending on the element size

The size of the model stiffness matrix for a mesh with element size of 3 mm would be in the range of 11 GB, while for a mesh using 2 mm elements, around 87 GB of memory would be required. Solving the model would of course require additional memory and computational power. Therefore, analysis of the Figure 8 data leads to the conclusion that element size for a static finite element model of a single tibia should be limited to somewhere between 2 and 3 mm for desktop computer calculations. For dynamic simulations, even the coarsest mesh presented in Figure 8 would result in 11,970 degrees of freedom; too many for an efficient multibody dynamic simulation. To overcome this problem, the overlarge finite element model implementation in the multibody model can be reduced in size using for instance, the Craig-Bampton method (Craig & Bampton, 1968).

Static correction modes together with the fixed interface normal modes can be used to calculate reduced mass and stiffness matrices. Those matrices can be later subjected to eigenvalue analysis followed by orthonormalization procedure to obtain the Craig-Bampton modes set. The reduction of the model comes from the fact that each column of the matrix of internal coordinates contains only one non-zero term, which corresponds to a mode shape. The coordinates that describe each degree of freedom in the Craig-Bampton method are divided into two groups: boundary and internal degrees of freedom. The boundary degrees of freedom are expressed in physical coordinates, while the internal degrees of freedom are expressed using modal coordinates. There is however transformation allowing for expressing modal coordinates in the physical coordinates and vice versa.

By selecting a high enough number of deformation modes, model accuracy can be preserved while still running a computationally efficient simulation. For instance, the tibia model used for walking, based on quantitative computed tomography with a mesh size of 5 mm could be represented with just 7 deformation modes without affecting strain energy more than 2 %. This compares to 18 deformation modes computed for that bone (Klodowski et al., 2009).

In preparing the reduced finite element model, numerical modal analysis needs to be performed on the initial full finite element model. The analysis requires

the definition of boundary conditions, which should reflect the boundary conditions of the model in the multibody simulation. For the tibia bone, the most intuitive choice for boundary definition is the use of center points of the knee and ankle joints as locations for creating boundary nodes. The connection between tibias epiphysis surfaces and the joint centers can be made using mass-less, rigid beams. This technique allows preserving the mass of the bone as well as distributing the surface load over the articular cartilage surfaces. More information about numerical modal reduction can be found in (Agrawal & Shabana, 1985). Selection of deformation modes is described in (Kim & Haug, 1990) and (Wu et al., 1995).

2.4 Medical imaging techniques

The bone strain estimation process strongly depends on bone model accuracy. To achieve sound results, bone geometry and material models should be reconstructed from human subjects. Two major medical imaging techniques are in use: Magnetic Resonance Imaging (MRI) and Computed Tomography (Bushong, 1988), (Buzug, 2008). Both methods are non-invasive and allow for scanning of internal body structures like soft tissue and bone, the difference is, however, in the operating principles. Magnetic Resonance Imaging uses powerful magnetic field and radio frequency pulses to produce images. The radio waves are used to redirect the axes of spinning protons, which are the nuclei of hydrogen atoms constrained by strong magnetic field. The radio signals are emitted and received by a set of coils placed on either side of the patient. A computer compares the sent and received signals and creates a set of images representing slices of the body of the patient. Although the strong magnetic field of MRI is generally harmless, implanted medical devices containing magnetic metals or electronic components may malfunction or cause problems during an exam.

The drawback of using MRI data is the lack of correlation between the voxel values and bone density (or any other mechanical property); therefore, only bone geometry and muscle insertion points in the bone can be reconstructed. An additional downside is that scanning time is relatively long, taking up to forty-five minutes to scan longer bones, depending on the spacing of slices. This long exposure duration can result in blurred images, due to patient movement, and subsequently result in inaccurate shape reconstruction. In addition, the initial

orientation of the leg with respect to the gantry affects the quality of the reconstruction. If the leg is placed along the gantry then voxels at the edges of the bone appear more homogeneous and capture the cortical material with less addition of the soft tissue outside the bone.

Computed tomography, on the other hand, accounts for material properties as well as the geometry. Moreover, scanning times for CT are shorter than scanning times for MRI. Scanning of long bones takes only several seconds. The drawback of CT is the amount of ionizing radiation received by the subject, which depends on scanning time, number of slices, and desired resolution. In the CT apparatus, multiple x-ray radiation sources and electronic x-ray detectors revolve around the subject. The subject moves axially at the same time producing a spiral movement of the x-ray beams. This scanning procedure is the most common nowadays due to reduction of exposure time in contrast to other scanning modes. The CT x-ray detectors measure radiation absorbed by tissue. This information is later processed to compose a set of image slices making up the scanned volume.

A major advantage of CT is its ability to image bone, soft tissue and blood vessels simultaneously. The main disadvantage of CT is exposing the subject to significant doses of radiation. The effective radiation dose from this procedure ranges from approximately 2 to 10 mSv, which is about the same as the average person receives from background radiation in eight months to three years.[3]

2.5 Medical image data

Medical images are stored in a file format specified in the Digital Imaging and Communications in Medicine (DICOM) standard.[4] The file contains general information about the patient and the scanning apparatus, scanning parameters, the number of slices, and the image data. Each slice is represented as a matrix of voxel values. Each voxel can take a value specified by the 16- or 32-bit range depending on the apparatus. In case of the MRI voxel, the value represents the response of water atoms to the changing magnetic field. This information allows distinguishing between soft tissues and bones. The CT voxel values

[3] Radiation dose information from:
http://www.radiologyinfo.org/en/safety/index.cfm?pg=sfty_xray
[4] Official full documentation of DICOM can be found at: http://medical.nema.org/

represent the absorption of x-ray radiation, which also gives good contrast between bones and soft tissues. In addition, there is a mathematical relationship between the CT values and density. Voxel size information, included in the header of the file, allows transforming pixel distances to millimeters. This information is essential in planar geometry reconstruction. The third dimension is obtained from slice spacing.

2.6 Bone geometry reconstruction

Bone geometry reconstruction starts with image segmentation (Bankman, 2000), (Simon & Lavallée, 1998). This step is required to differentiate between bones and soft tissue. In the case of high contrast images, threshold-based segmentation can be sufficient to produce accurately the contours of bones in each single slice. Secondary segmentation may be aimed at differentiating between cortex and trabecular bone structures. In which case, manual work usually is needed, because the density of both bone structures is similar. Figure 9 demonstrates the effects of applying thresholds for two different bone regions. In the first case, Figure 9a, a single operation is sufficient to produce a valid mask. In the second case, Figure 9b, the density variation within the trabecular structure requires additional processing to remove holes from the mask and smooth the edges. Situation in Figure 9b demonstrates also the problem of determining the boundary between the trabecular and cortical structures, which can be solved by either assuming constant cortical thickness or performing manual segmentation.

An edge detection algorithm is usually applied to bone segments to extract external and internal boundaries. Bone boundaries are later discretized to a cloud of points representing the outer and inner bone shells. Using Computer Aided Design (CAD) or specialized medical analysis software, it is possible to fit a surface to the cloud of points generating a surface bone model.

A simple method of fitting a surface is to produce polygonal fits for the points in each slice and then connect them linearly. This approach produces models that are easy to mesh, as the surface is continuous. In the case of a small number of slices, this method will result in an overly simplified geometrical reconstruction. A more sophisticated method relies on curved three-dimensional b-spline fitting to connect slices. The surface will be smoother and more

realistically represent bone. For this method to work, point homogenization is normally required prior to curve fitting. Homogenization of the cloud of points reduces surface fitting errors in the epiphysis regions of a bone. The surface model can be used as is in the finite element software to produce the surface mesh, or it can be transformed to a volumetric description, which can be meshed with solid finite elements.

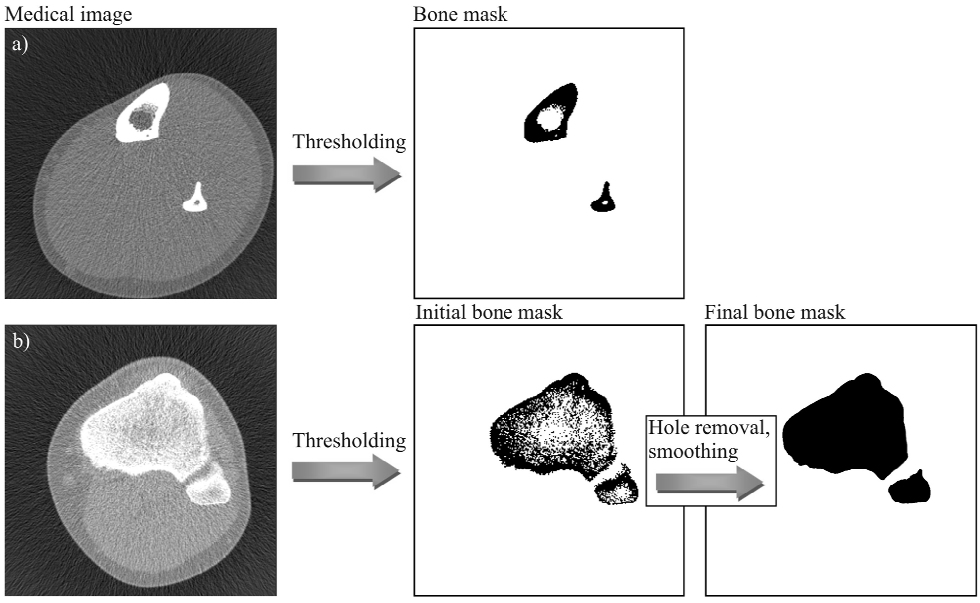

Figure 9. Medical image processing: a) Single threshold applied to a slice of a diaphysis of tibia and fibula produces bone mask, and b) Threshold applied to epiphysis of tibia and fibula requiring additional hole-removal and smoothing

2.7 Bone material models

The bone material model has a significant influence on the strain results as indicated by Kłodowski (Klodowski et al., 2009). From an anatomical point of view, bones are anisotropic; however, isotropic material models for bones are also widely used, due to their simplicity, as lower number of parameters need to be specified. On average, bone strain during exercise should not exceed 3,000 με, however, peak values might be higher. From modeling point of view, strain values within 5,000 με are within the validity of the small deformation theory (Slaughter, 2002). Moreover, the bone material yield point exceeds 1 % strain (Kopperdahl & Keaveny, 1998), therefore a linear material model description can be considered as a well acceptable assumption for modeling

bone. Bone mineral area density, mass per square centimeter, is the most reported bone material property. This value however, is useless in terms of finite element modeling, in which physical density is important. Physical bone density, called 'apparent density' in biomedicine, is the ratio of bone mass to total volume of the sample.

According to Keller, apparent bone density ranges from 50 to 1,890 kg/m^3 (Keller, 1994). The mechanical properties of bone depend strongly on age, physical activity level, and genetics. The Young's modulus for cortical bone ranges from 12 to 23.3 GPa. In the case of macro scale Young's modulus of trabecular bone, the range is even greater, from 0.01 to 10 GPa (Ashman et al., 1984). The Poisson's ratio for cortical bone is between 0.2 and 0.5, while for trabecular bone it is reported to vary between 0.01 and 0.35.

Table 1 is a compilation of Young's moduli for human bone. The data describe the axial stiffness properties of bone material. At the material level, trabecular and cortical bone are identical (Rho et al., 1993). However, on the macro level, there are significant differences between trabecular and cortical bone material properties. Table 2 presents average femoral elastic property values as reported in (Reilly & Burstein, 1975).

The stiffness of compact bone tissue depends on the bone from which it is taken. Fibular bone has a Young's modulus about 18 % greater, and tibial bone about 7 % greater, than that of femoral bone. The differences originate in the histology of the bone tissue. The choice of the type of material model used for bone modeling is determined mostly by the type of finite element discretization of the bone. For a coarse mesh, it is impossible to account for differences between trabecular and cortical structures; therefore an averaged material model must be used. When the discretization is fine, it is possible to differentiate between the two bone structures and use separate material models. To account for trabecular structure in detail, a micro finite element model is needed, where the element size is in the range of 1 µm. This type of model is usually used to estimate the overall elastic parameters of the trabecular structure to be used in a whole bone models, due to the computational expense of micro-finite element models. The use of micro-finite element models is also limited by the low spatial resolution of clinically used CT scanners (180 microns and above).

Table 1. Young's modulus for bone, literature summary

Source	Testing method	Elastic modulus [GPa]
(Wolff, 1892)	Hypothesis	17–20 (assumption)
(Runkle & Pugh, 1975)	Buckling	8.69 ± 3.17 (dry)
(Townsend et al., 1975)	Inelastic buckling	11.38 (wet)
(Williams & Lewis, 1982)	Back-calculating from finite element models	1.30
(Ashman & Rho, 1988)	Ultrasound test	12.7 ± 2.0 (wet)
(Ryan & Williams, 1989)	Tensile testing	0.76 ± 0.39
(Hodgskinson et al., 1989)	Microhardness	15
(Kuhn et al., 1989)	Three-point bending	3.81 (wet)
(Mente & Lewis, 1989)	Cantilever bending with finite element analysis	7.8 ± 5.4 (dry)
(Choi et al., 1990)	Four-point bending	5.35 ± 1.36 (wet)
(Rho et al., 1993)	Tensile testing Ultrasound test	10.4 ± 3.5 (dry) 14.8 ± 1.4 (wet)
(Rho et al., 1997)	Nanoindentation	19.6 ± 3.5 (dry) longitudinal 15.0 ± 3.0 (dry) transverse
(van Rietbergen et al., 1995)	Trabecular bone, micro finite element model	2.23–10.1

Table 2. Orthotropic elastic properties of femur (Reilly & Burstein, 1975)

Parameter	Value
Young's moduli (longitudinal direction)	17 GPa
Young's moduli (transverse direction)	11.5 GPa
Shear moduli (longitudinal direction)	3.6 GPa
Shear moduli (transverse direction)	3.3 GPa
Poisson's ratio (longitudinal direction)	0.58
Poisson's ratio (transverse direction)	0.31

For Quantitative Computed Tomography (QCT) data, the material model can be estimated from the voxel values. Several studies have examined relationships between CT voxel values and apparent bone density and elasticity. The use of CT-based material model allows accounting for inhomogeneous mass and elastic properties distribution. To normalize the CT raw data it is usually converted to Hounsfield units HU using the following expression.

$$HU = \frac{1000(CT - CT_w)}{CT_w - CT_A}, \tag{31}$$

where: CT, CT_w, and CT_A are the linear attenuation coefficients for bone, water, and air respectively (Rho et al., 1995). Parameter values can be determined from CT images taken of a calibration sample, which is simply water in a tank

surrounded by air. The elastic modulus can be then estimated using (Carter & Hayes, 1977) relationship, which accounts also for the strain rate.

$$E = 3.790\hat{\varepsilon}^{0.06}\rho^{3}, \tag{32}$$

where E is the Young's modulus expressed in GPa, $\hat{\varepsilon}$ is the strain rate for the applied load in Hz, and ρ is the apparent density in g/cm^3, which can be determined as a function of Hounsfield units HU as expressed by equation (33).

$$\rho = \frac{a_\rho + b_\rho HU}{1000} \tag{33}$$

Parameters a_ρ and b_ρ are site specific and can be obtained from Table 3.

Table 3. Site specific parameters for dependency of density on Hounsfield units (Rho et al., 1995)

Site	$\boldsymbol{a_\rho}$	$\boldsymbol{b_\rho}$
Proximal tibia	114	0.916
Proximal femur	131	1.067
Distal femur	139	1.205
Proximal humerus	173	0.624
Lumbar spine	47	1.122

For dynamic simulations, strain rate is usually not known prior to performing the simulation, for that reason a dependency described by Helgason can be used (Helgason et al., 2008), which does not take into account the strain rate.

$$E = a\rho^{b} \tag{34}$$

The parameters a and b in the equation (34), can be chosen depending on the bone site according to Table 4.

Table 4. Parameters for the dependency of Young's modulus versus CT voxel values

Source	Site	Density range [g/cm^3]	*a*	*b*
(Lotz et al., 1990)	Trabecular structure of femoral neck	0.18–0.95	1.310	1.40
(Snyder & Schneider, 1991)	Cortical structure of tibial diaphysis	1.748–1.952	3.891	2.39
(Linde et al., 1992)	Trabecular structure of proximal tibia	~0.273	4.778	1.99
(Dalstra et al., 1993)	Trabecular structure of pelvis	0.109–0.959	2.0173	2.46
(Morgan et al., 2003)	Trabecular structure of vertebrae	0.11–0.35	4.730	1.56
(Morgan et al., 2003)	Trabecular structure of proximal tibia	0.09–0.41	15.520	1.93
(Morgan et al., 2003)	Trabecular structure of greater trochanter	0.14–0.28	15.010	2.18
(Morgan et al., 2003)	Trabecular structure of femoral neck	0.26–0.75	6.850	1.49
(Morgan et al., 2003)	Trabecular structure, pooled	0.09–0.75	8.920	1.83

2.8 Actuation systems

Typically, two types of dynamic human models are analyzed: passive and active. Passive models are usually software implementations of crash test dummies, which have no self-actuation system. In this type of model, bodies are acted upon by external forces coming from contact models, fixtures, and passive elastic or damping components. Active models, on the other hand, are used in simulations where human activity must be analyzed. In active model, body motion is primarily a result of internal forces developed in the model. One of the most straightforward ways of adding skeletal actuation is by applying torque at skeletal joints. Another option, which is more anatomically correct, is to model muscle actuation. Both methods are explored and compared in this subsection.

2.8.1 Torque actuators

The simpler skeletal actuation method benefits primarily from its straightforward implementation. By assuming kinematic joints in the model and prescribing the desired motion path for each bone (prescribed joint angular change history), the torques needed to replicate the motion can be calculated

using Proportional-Integral-Derivative (PID) controller. The model does not suffer from redundancy problems, as each degree of freedom is controlled by a single torque actuator. The torque M required to perform the motion for a single time step, can be calculated using the following formula.

$$M = P(\alpha_c - \alpha_t) + I \int (\alpha_c - \alpha_t)\, dt + D \frac{\partial(\alpha_c - \alpha_t)}{\partial t}, \qquad (35)$$

where the symbols α_c and α_t represent, respectively, the current and target angular positions of a joint. In equation (35) constants P, I, D are proportional, integral, and derivative parameters of the controller. Parameter t represents time. For sufficiently slow movements without rapidly changing external forces, the derivative and integral parts of the controller can be omitted.

Within their angular limits, torque actuators enable the replication of multiple body motions. They can be applied in rigid body skeletal models when the emphasis of a study is on motion or the interaction between the skeleton and foreign objects. Joint net torques will always converge to the minimal solution with torque actuation. However, using this type of actuation in a flexible bones model will yield unrealistic results, because the influence of local forces on the bones near the muscle attachment points will be neglected. Furthermore, with actuator-based torque actuation, bending will always be the dominating load in actuated bones (Rantalainen & Kłodowski, 2011).

2.8.2 Muscle actuators

To overcome the analytical limitations of skeletal torque actuation, simulated muscle actuation is required. Muscle actuator models, unlike torque actuators, are made by applying forces to connection points on bone pairs. The attachment points define the geometry of the muscle, which changes during motion. A simple closed-loop muscle model develops a force between muscle attachment points with a PID controller that minimizes the length error of the muscle (difference between current and target length for time instance). Muscle length change history, used as an input (target function), can be obtained from the inverse dynamics of the skeletal system driven by motion capture data. The simulated muscles can be also driven with open-loop control. In that case, the force produced by the muscle can be proportional to the prescribed control signal. The control signal may be synthetic or come from, for instance, rectified

and filtered electromyography (EMG) measurements. It has to be noted however, that due to the differences of the model and real subject, EMG driven muscles always need to be supported by either torque actuators or muscle actuators driven in closed-loop control fashion. As a rule of the thumb, each degree of freedom needs to be actuated by at least one closed-loop actuator. The reason why open-loop controlled muscles are interesting is that they allow reducing the muscle redundancy problem, and can be used to replicate antagonistic muscle action.

The advantage to simulating muscle actuation is that forces are applied to bones at anatomical muscle attachment points. In addition, with this type of actuation, there is no need for kinematic joints in the model and complex contact ligament-based joints can be applied. The drawbacks are the complexity and redundancy of musculature in the human body. An optimization procedure must be used to simplify the actuation scheme and still produce the prescribed motion pattern (Anderson & Pandy, 2001). The correct motion path can be preserved by arbitrarily adjusting net muscle force to produce the desired motion while keeping relative muscle forces constant. However this leads to inconsistencies. To overcome the problem of over-actuation, the force division between the muscles of a single muscle group can be made proportional to the physiological cross section of each of the muscles or be the result of a metabolic cost minimization procedure.

With simulated muscle actuation, large angular displacements between bone pairs can result in the muscle force passing through the center of their connection joint resulting in a mathematical singularity. This problem can be overcome by implementing the wrapping of muscle around bones. Tissue wrapping implementation in multibody simulations remains challenging and increases model size considerably resulting in longer computation times. As a result, it is relatively rarely used. However, muscle wrapping should be considered in studies where large angular joint displacement is a consideration. The main disadvantage of muscle actuators is the number of parameters that need to be obtained (Zajac, 1989).

Hill muscle model

The Hill muscle model (Hill, 1938) is a typical example of a phenomenological model. It was constructed to connect known input and output pairs obtained from experiments on muscle tissue, using simple and predictable mechanical model. The resulting model includes a parallel spring-damper structure with a non-linear contracting element added in series to the spring. A schematic diagram of the Hill muscle model is presented in Figure 10.

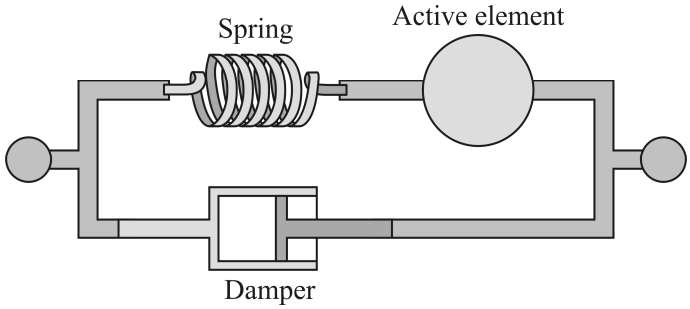

Figure 10. Schematic diagram of the Hill muscle model

Physiological limitations and muscle model parameters

Physiological Cross-sectional Area (PCSA) is an important muscle parameter because maximum muscle force is linearly related to it. By definition, PCSA is equal to muscle volume divided by fiber length. Muscle volume can be measured non-invasively with nuclear magnetic resonance imaging. Fiber length can be estimated using relationships seen in dissected muscles between muscle length and fiber length. The maximum fiber force capacity of muscle has been determined to be 87.1 N/cm^2 (Hatze, 1981). The product of the maximum fiber force capacity of a muscle and the PCSA for this muscle is the maximum isometric force that the muscle can produce. The maximum passive force is expressed more precisely as follows.

$$F_{passive} = \frac{k\varepsilon}{1 - \frac{\varepsilon}{asym}}\sigma \tag{36}$$

The PCSA is σ, the strain asymptote parameter is $asym$, k is passive muscle stiffness and, strain, ε, in equation (36) can be expressed in terms of L_{curr}, the current (instantaneous) length of the muscle, and L_{free}, the free length of the muscle at rest when removed from the body.

$$\varepsilon = \frac{\left(L_{curr} - L_{free}\right)}{L_{free}} \tag{37}$$

More details on proper application of different muscle models can be found in (Winters, 1995).

2.9 Contact definition

The investigated movements of this study, which include walking and a number of exercises, require the description of feet-to-ground contact or leg support. For walking, accurate definition of the contact model is important, because it should provide a stable support for the whole body. For that purpose, a multi-element contact model was prepared for each foot. The contact model consists of two elements. The first is the geometric contact detection procedure, and the second is the calculation routine for contact force. Both routines use the same contact geometry. The contact geometry of the foot is simplified to ellipsoids; the ground geometry is represented by a single plane. Contact elements on the foot are presented in Figure 11.

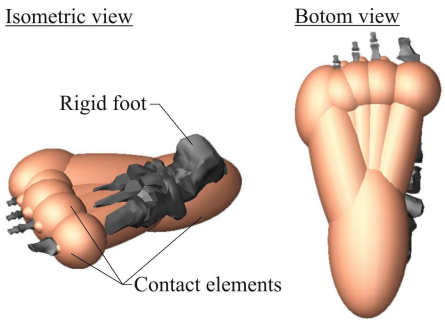

Figure 11. Overview of the locations and shape of the foot contact elements

The ellipsoid-plane contact model runs efficiently and results in quick contact calculations. Contact force F is calculated based on penetration depth s using the following formula.

$$F = Ks^n + c(s)\dot{s}, \tag{38}$$

where K is contact stiffness, n is the exponent coefficient, $\dot{s}$ is the velocity of penetration, $c(s)$ is the damping coefficient function dependent on penetration value. Penetration depth is defined as the shortest distance between the centroid of the contact volume of the ellipsoid that penetrates through the contact plane.

The contact force aligns with the contact point and the centroid of the contact volume. An ellipsoid-plane contact pair is shown as an example of contact detection in Figure 12.

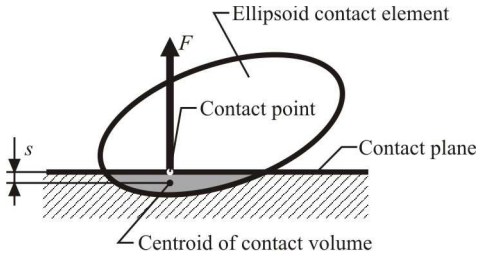

Figure 12. Schematic description of elements in the ellipsoid-plane contact model

The contact damping-penetration relation can be described by the relationship expressed in equation (39).

$$c(s) = \begin{cases} \left(\dfrac{\sin\left(\dfrac{s}{s_{max}}\pi - \dfrac{\pi}{2}\right)}{2} + 0.5 \right) c_{max} & s \le s_{max} \\ c_{max} & s > s_{max} \end{cases} \tag{39}$$

The limit penetration depth s_{max} is where the maximum damping coefficient c_{max} is applied. The relationship between c/c_{max} and s/s_{max} is illustrated in Figure 13. Friction can be modeled dynamically, which means the friction coefficient is slip velocity dependent. Friction coefficient dependency on slip velocity is shown in Figure 14.

The friction coefficient μ is velocity dependent and can be defined as follows.

$$\mu(v) = \begin{cases} -\text{sign}(v)\mu_d & |v| > v_d \\ -f(|v|, v_d, \mu_d, v_s, \mu_s)\text{sign}(v) & v_s \le |v| \le v_d \\ f(v, -v_s, \mu_s, v_s, -\mu_s) & -v_s < v < v_s \end{cases} \tag{40}$$

The parameters v_s, v_d, μ_s, and μ_d represent respectively: stiction transition velocity, dynamic friction transition velocity, static friction coefficient, and dynamic friction coefficient. The smooth transition function f is defined in equation (41), and the *signum* function sign is specified in equation (42).

$$f(x, x_1, y_1, x_2, y_2) = y_1 + \frac{y_2 - y_1}{x_2 - x_1} - \frac{y_2 - y_1}{2\pi} \sin\left(\frac{2\pi(x - x_1)}{x_2 - x_1}\right) \quad (41)$$

$$\text{sign}(x) = \begin{cases} 1 & x > 0 \\ 0 & x = 0 \\ -1 & x < 0 \end{cases} \quad (42)$$

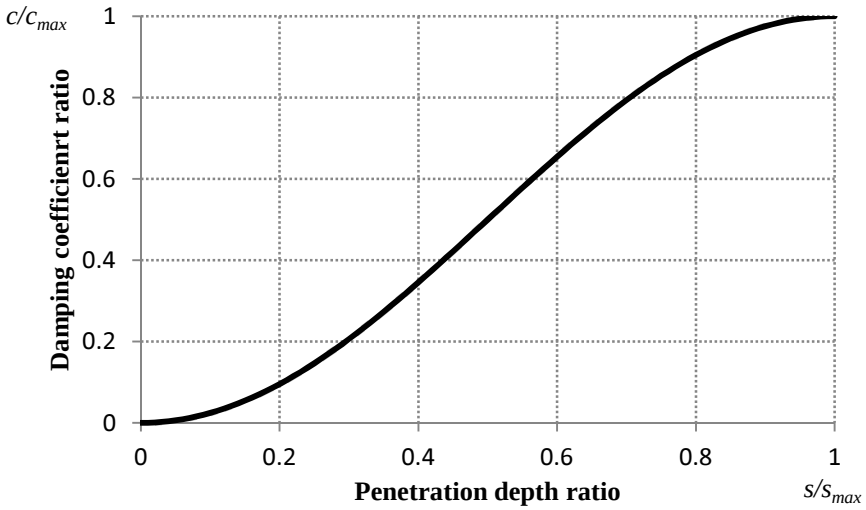

Figure 13. Damping coefficient dependency on penetration depth in the contact pair described as a ratio with respect to the maximum values

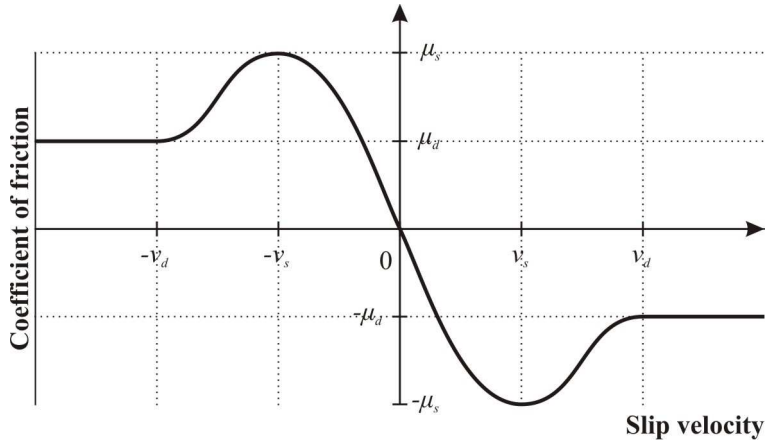

Figure 14. Friction coefficient dependency on slip velocity

2.10 Musculoskeletal model description

2.10.1 Joint description

Joints in the multibody model act as constraints between separate bodies. Their function is to unite separate bodies to form a working mechanism. While joint description is relatively simple in engineering practice, in reality, human body joints are very complex. A characteristic feature of human joints is their nearly zero friction, which allows them to function a lifetime without incurring excessive wear as long as the loading conditions do not damage the cartilage.

Joint cartilage acts as a bearing and lubrication medium, damping vibrations and cushioning impact forces. Ligaments secure skeletal joints, holding them together when not loaded and stabilizing them throughout their range of motion. Ligaments are also responsible for cartilage pre-tensioning. Their presence adds passive stiffness to a joint.

Realistic joint description is not only complex, but also requires the input of parameters that might be difficult to obtain. Therefore, most mechanical musculoskeletal models utilize simpler kinematic joints instead of attempting to solve the realistic description. Knee, lumbar, thoracic, lower neck, elbow, and wrist are usually modeled as revolute joints. Ankle and shoulder are often described as universal joints. The hip joint is regularly modeled as a spherical joint, and the upper neck and scapular joints are modeled as fixed joints. Joint description, and its level of complexity, depends on the type of exercise being simulated. For instance, there is no need to describe a wrist joint with high accuracy for a walking exercise, which focuses on the lower body.

An important concept for kinematic joint modeling of a human body is the inclusion of joint angle limits. In most cases, these limits are achieved by adding torsion spring elements to represent the limit stiffness. The common joint parameters are presented in Table 5. The flexion/extension of the joints takes place in the sagittal plane, inversion/eversion is the movement in the frontal plane and the rotation corresponds to the motion around the normal of the transverse plane of the human body. All the definitions of the motion correspond to the body in standing position with the hands placed along the body.

Table 5. Kinematic joint parameters used in the models (Al Nazer et al., 2008a)

Joint	Type	Flexion/extension		Inversion/eversion Abduction/adduction		Rotation	
		Stiffness [Nmm/º]	Damping [Nmms/º]	Stiffness [Nmm/º]	Damping [Nmms/º]	Stiffness [Nmm/º]	Damping [Nmms/º]
Ankle	Universal	210	21	10,000	1,000	-	-
Knee	Revolute	270	27	-	-	-	-
Hip	Spherical	700	70	1,500	150	800	80
Lumbar	Revolute	1,000	100	-	-	-	-
Thoracic	Revolute	1,000	100	-	-	-	-
Lower neck	Revolute	1,000	100	-	-	-	-
Upper neck	Fixed	-	-	-	-	-	-
Scapular	Fixed	-	-	-	-	-	-
Shoulder	Universal	700	70	700	70	-	-
Elbow	Revolute	60	6	-	-	-	-
Wrist	Revolute	30	3	-	-	-	-

2.10.2 Muscle models configurations

Depending on the purpose of the model and type of motion to be simulated, different muscle configurations can be used. Simulations of low speed movement, like walking, and some of the exercise movements can be performed with simple PID closed-loop controlled muscle models. For these movements the range of motion is usually limited and muscle load change is moderate, so non-linear behavior effects can be neglected. The closed-loop Hill muscle model is advised for more dynamic movement, because it can account for viscous-elastic muscle properties. Neither of these approaches can accurately model antagonistic muscle effects. To model antagonistic force production, an open-loop muscle element must be added so that it drives joint flexion or joint extension with the presence of closed-loop muscle driving the opposite direction. It can also be implemented on both sides. Then, however, at least one closed-loop muscle or joint torque controller needs to be implemented to ensure real motion replication. The difficulty in such an approach lies in determining the force values, because from a mathematical point of view, each muscle configuration can produce a similar motion with an infinite number of solutions, and the solutions differ only by the scaling factor of the antagonistic force.

Accurate muscle system description results in a redundancy problem. This problem can be alleviated by applying a hybrid muscle model, where some of

the muscles are controlled in closed-loop form and some in open-loop fashion. This hybrid muscle model was described by Kłodowski (Klodowski et al., 2009). It allows reducing the redundancy level, and therefore speeds up computation.

2.11 Modeling environment and simulation procedure

The simulations performed as part of this thesis were carried out using the general-purpose multibody software ADAMS R3 with the human modeling plug-in LifeMOD 2008.1. ADAMS software provides a simulation environment consisting of the pre-processor, the modeling environment, the solver and the post-processor. The ADAMS interface is designed for general engineering modeling purposes. By itself is not ideally suited for biomechanical simulations. The LifeMOD plug-in adds user interface elements intended to simplify human body modeling. The human model database included in LifeMOD allows for creation of three-dimensional generic musculoskeletal models based on gender, height and weight. The models can be also further adjusted to match specific subject dimensions. The LifeMOD models consist of rigid bodies connected via kinematic joints. The software enables modeling with torque actuators, closed- and open-loop controlled muscle models with simple PID control system, or Hill based models. A whole body model can be equipped with a set of 122 muscles attached to the bones at anatomical landmarks. Additional muscles can also be manually added. To account for flexibility in the bones, the bones in focus were replaced by flexible versions prepared in ANSYS 12, which is a general purpose finite element solver. In this work, the videos registered as a part of motion capture procedure, were analyzed using Peak Motus software to extract trajectories of markers.

The steps of the simulation procedure used in this research are presented in Figure 15. The first step is the inverse dynamics simulation. It is performed with rigid skeleton and recording muscle models. During the inverse dynamics simulation, the model is actuated by markers following the trajectory obtained from a motion capture. The muscles do not produce any force, instead, they record the muscle length change required to perform the motion. Output data from the inverse dynamics simulation is used as the initial conditions for a forward dynamics simulation.

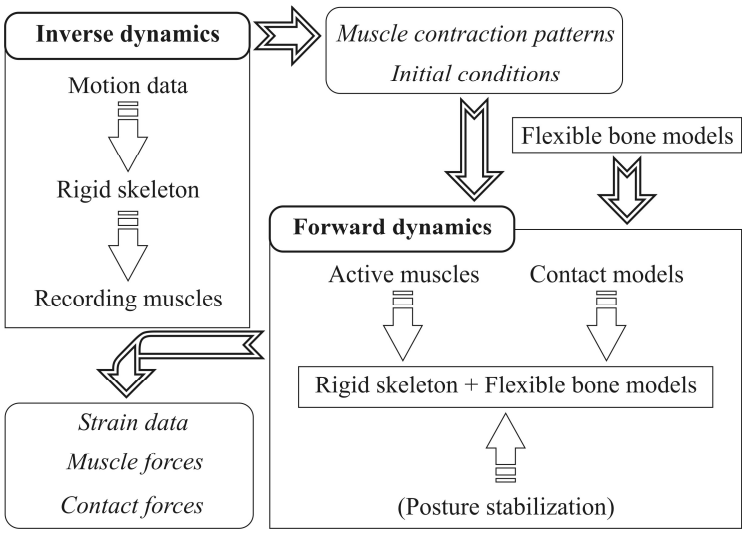

Figure 15. Simulation procedure – The posture stabilization component is optional and is applied only when necessary.

The second step is the forward dynamics simulation. Prior to this step, the model is equipped with flexible bodies, and the recording muscles are replaced with active muscle models. In the forward dynamics simulation step, motion capture markers are deactivated, and the model is driven by muscle models only. This phase concentrates on final calibration of the parameters of muscle models and the initial state of the body model. After the calibration, the forward dynamics simulation is run one more time. Strain data, muscle forces, and contact forces are obtained. The forward dynamics simulation tries to replicate a real life situation with the use of pre-computed muscle contraction patterns. The forward dynamics simulation is also used to determine the list of deformation modes with the influence on the strain energy of the bone above 1 %.

Any dynamic differences between the real subject and the computational model are visible in this step. The differences may be just insignificant body trajectory errors or can cause the skeletal model to lose balance. Therefore, it is especially important, for motion that requires the model to balance, to implement a stabilization procedure that will account for simplification of the model with respect to the real situation (Menegaldo et al., 2003). LifeMOD provides a tool that can use the path obtained in the inverse dynamics to stabilize the motion of

the skeleton in the forward dynamic simulation by the means of torques and/or forces applied at the center of mass of the model.

Contact models can be implemented before the first or second step. From a computational point of view, because contact models are computationally expensive, it is beneficial to implement them just before the second step.

2.12 Human musculoskeletal models validations methods

2.12.1 Motion pattern validation

It is a common practice to use motion capture as an input for model motion. The existence of the reference motion data enables validating muscle model performance in terms of motion replication. To simulate real conditions accurately, the mechanical behavior of the skeleton driven by the modeled muscle actuators should be identical to the skeleton behavior of the subject. To validate the motion data, trajectories of the centers of mass of the skeletons used in forward dynamics can be compared to the data from inverse dynamics. This procedure is good for standing posture exercises; such as walking, running, squatting, *etc*. For exercises performed in a sitting position, the trajectories of legs, hands, and upper body are considered.

Position error e between body segment trajectories of inverse and forward dynamics models can be computed using equation (43).

$$e = \frac{\Sigma_{t=0}^{N} \sqrt{\left(\frac{x_i(t)-x_f(t)}{x_i(t)}\right)^2 + \left(\frac{y_i(t)-y_f(t)}{y_i(t)}\right)^2 + \left(\frac{z_i(t)-z_f(t)}{z_i(t)}\right)^2}}{N}, \tag{43}$$

where $x_i(t)$, $y_i(t)$, and $z_i(t)$ are coordinates of the point on the skeleton used in the inverse dynamics simulation at the time point *t*. Coordinates for the forward dynamics of the same point are marked as: $x_f(t)$, $y_f(t)$, and $z_f(t)$. Symbol *N* denotes the total number of time points used in the simulation.

2.12.2 External force validation

The multibody human model, in general, has to interact with foreign objects, thus creating reaction forces. A demonstrative example is walking, during which there is contact between the feet of the subject and the floor surface. For walking, one of the validation methods is cross-correlation of experimentally

measured ground reaction force and contact model output. For other exercises, the contact forces between handles and hands, or legs and supports can be used for validation.

2.12.3 Additional validation methods

Whenever it is possible to obtain reliable reference measurement data, it should be used to evaluate model performance. In the biomechanical field, this is usually difficult, especially in terms of strain data measurements, which are available only for a few subjects. Because strain results are subject and exercise specific, only the range of observed values can be compared with values obtained from *in-vivo* measurements. In *in-vivo* strain assessment, usually the principle in-plain strain values are reported. Multibody simulations allow estimating any strain values within the bone of interest. The author suggests comparing axial strain values in long bones, whenever comparison data is available. By comparing axial strain values, it is possible to determine bone mechanical deformation and the loading case for specific bone sites. Specifying a particular axial cross section and determining its area are straightforward. In-plane strain can also provide deformation and loading case information, however, site location and strain orientation must be known and each are difficult to define unambiguously.

2.13 Limitations of the models

The musculoskeletal models presented in this work have several limitations. Firstly, the joint models are simplified, which makes prediction of joint surface load distribution impossible. Only total joint forces and torques can be obtained from the models. Secondly, although the LifeMOD posture stabilization algorithm is one of the simplest possible, it is not entirely realistic, which can add relatively small unrealistic external forces that affect strain and ground reaction forces results. This problem applies only to the modeling of standing posture activities. For activities involving a seated subject, the problem no longer exists, because posture stabilization is no longer needed.

Muscle model representation as a single component force joining two body segments implies single point muscle attachment. In reality, muscles are attached over relatively large surfaces of the bone. The single point attachment model leads to stress concentration around the muscle attachment nodes, so

stress and strain predictions at muscle attachment locations and in their proximity is not possible for the moment. For that reason, strain values were predicted only on the locations not affected directly by muscle attachment forces.

3 Walking simulations

3.1 The subject

Prior to the simulation, motion capture and measurements of human subject were required to simulate strain values of a specific person with natural motion pattern. The experiment was conducted at the University of Jyväskylä. The subject volunteered for the experiment. Subject was Caucasian male; height 168 cm, weight 65 kg and age 65 years.

3.2 Human gait

Walking is one of the basic physical activities that people perform daily. Medical problems related to muscle loss, neural system dysfunctions, or injury to the lower extremities usually cause reduced mobility and significant discomfort. Also, human gait is relatively unique to each individual due to differing bone shapes, joint conditions, and medical history. Moreover, a gait pattern can be used to predict mental disease, which is otherwise difficult to diagnose (Verghese et al., 2002). For these reasons, human gait is an interesting topic for researchers specializing in medical field.

Human gait can be divided to four distinct actions; the heel strike, double support, the toe off, and the single support swing phase. In addition, when a specific leg is touching the ground, this part of the action is referred as a stance, and the time that the leg is in the air is called the swing phase. The phases of the gait are always described with respect to the leg of interest. Figure 16 illustrates the phases of the human gait.

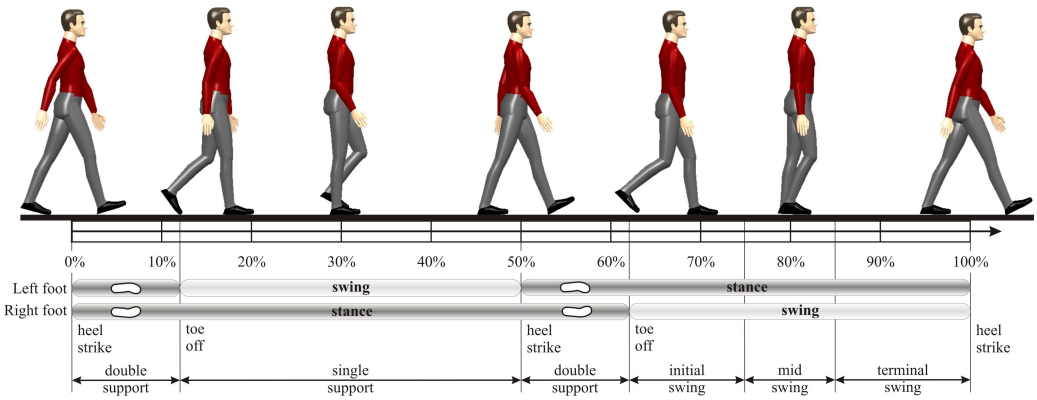

Figure 16. Phases of human gait

The gait percentage scale is described with respect to the right leg. The same time scale will be used in the subsequent figures concerning walking.

3.3 Lower leg study

Tibia bone is the most accessible bone for *in-vivo* strain measurements. For that reason, a sufficient amount of bone strain data at the tibial midshaft is available from the literature, which can be compared with the computer model strain results. Tibial strain magnitudes during locomotion have already been simulated using flexible multibody approach in the past (Al Nazer et al., 2008a), (Al Nazer et al., 2008b), (Klodowski et al., 2009), (Al Nazer et al., 2011). Based on the past modeling experience, the new model was prepared with several significant improvements in terms of the material model of the tibia; the muscle models used, the knee joint description, and finally, the weight bearing flexible fibula model was included.

3.3.1 Model description

The three-dimensional musculoskeletal model, parameterized by weight, height, age and gender, was created using LifeMOD software. Eighty-eight upper-body and 17 left leg muscles were modeled using simple PID controlled muscle model. In the right leg, 16 closed-loop Hill muscle models (Hill, 1938), and an open-loop EMG activated Hill muscle model for the tibialis anterior were used. This arrangement was found adequate since only the right tibia and fibula strain values were evaluated. Hill muscle models parameters are given in Table 6. All joints were modeled using kinematic joints with the parameters listed in chapter Musculoskeletal model description.

The generic model was customized by describing flexibility of fibula and tibia at the right leg. In addition, knee model was upgraded by attaching right patella to the knee by the revolute joint in which the rotation axis coincides with the tibio-femoral revolute joint. Three tendon elements were attached to combine patella and tibia, representing central, medial, and lateral thirds of patellar tendon. The superior tibio-fibular joint was defined as a prismatic joint between the point on the facet on the inner surface on the head of the fibula, and the corresponding point on a facet on the posterior part of the external tuberosity of the tibia. The joint axis was parallel to the longitudinal axis of tibia. The inferior tibio-fibular joint was modeled as a hinge joint with the axis of rotation

in the intersection of the transverse and coronal planes. The improvements with respect to the generic model are illustrated in Figure 17.

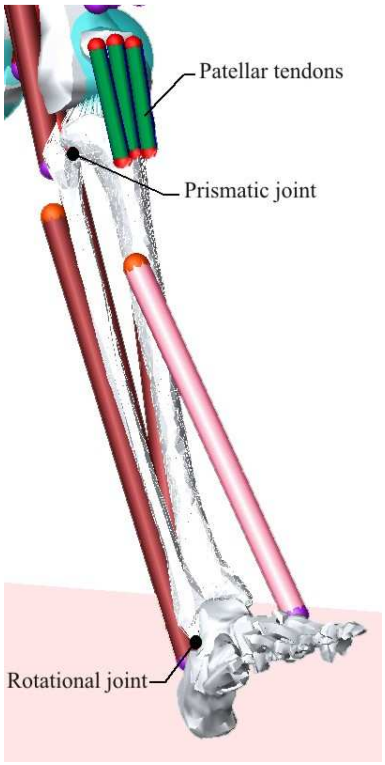

Figure 17. Improved lower leg model – The rotational and translational joints between tibia and fibula are marked as well as the introduced patellar tendon models.

Geometry and density information of the tibia for the finite element model were obtained from a helical QCT scan of the lower limb of the subject (LightSpeed RT16, GE Medical Systems). The slice thickness was 0.625 mm, slice spacing 0.31 mm and pixel size 0.39 mm. Reconstruction of tibial geometry was performed using custom code later referred as CTWorkshop. Data points, defining the outer surface of the tibia, were normalized to a net of 5 mm equidistant points prior to export to SolidWorks (SolidWorks, version SP3.1, Dassault Systems, Sureness, France), where the bone surface based on three-dimensional splines was reconstructed using least square fit method. The mean error in modeling the surface was 0.4 mm, while the range of error spanned from 0.2 up to 2.1 mm. Reconstructed geometry of the bone was exported to the

finite element software ANSYS (ANSYS, version 12.0, ANSYS Ind, Cannonsburg, USA), where four-node tetrahedral elements of a maximum 5 mm size were used resulting in 21,430 elements and 4,717 nodes model size. Later, density and elasticity properties were assigned using CTWorkshop. For each element, an average QCT voxel value was calculated using image stack voxels that are located within the volume of the element.

Table 6. Hill muscle model parameters

Muscle parameter	**Value**
Stiffness	0.871 N/m
Damping	0.0871 Ns/m
Average sarcomere length of free muscle	2.1 µm
Length of sarcomere at rest	2.6 µm
Length of sarcomere at muscle optimal length	2.8 µm
Strain asymptote	0.7
Passive muscle stiffness	3.34 N/cm^2
Maximum isometric muscle stress	100 N/cm^2
Maximum shortening velocity of the muscle	60 cm/s
Shape force-velocity curve (shortening)	0.25
Shape force-velocity curve (lengthening)	0.075
Maximum relative force (lengthening)	1.5
Shape factor	0.54
P gain	10,000,000
I gain	100,000,000
D gain	1,000,000

Poisson ratio for all three directions was assumed to be 0.4, shear modulus in the transverse plane was assumed to be 5 GPa, and 3.5 GPa for the two other orthogonal planes. Rigid, massless beams were added between articular cartilages of the bone and joint centers locations. Joint centre points were used in the eigenvalue analysis as boundary nodes. Rigid beam links enabled surface load distribution and kinematic connection between different bones in the multibody model.

Fibula bone was modeled in a simplified fashion using generic geometry from LifeMOD. Material properties were assumed to be homogeneous orthotropic. Elastic bone properties proposed by (Dong & Guo, 2004) were used. Eigenvalue analysis was performed analogically as it was for the tibia model. In this model, the addition of the fibula was aimed only at quantifying the load sharing ratio between the fibula and tibia, thus simplifications in the material model of the fibula are justified.

3.3.2 Results

Deformation modes of QCT based tibia and generic fibula are presented in the Figure 18 and Figure 19, respectively. In this study, 25 deformation modes were used for tibia model, out of which 7 affected the strain energy more than 1 %. For fibula, 21 deformation modes were used out of which 7 contributed more than 1 % to strain energy.

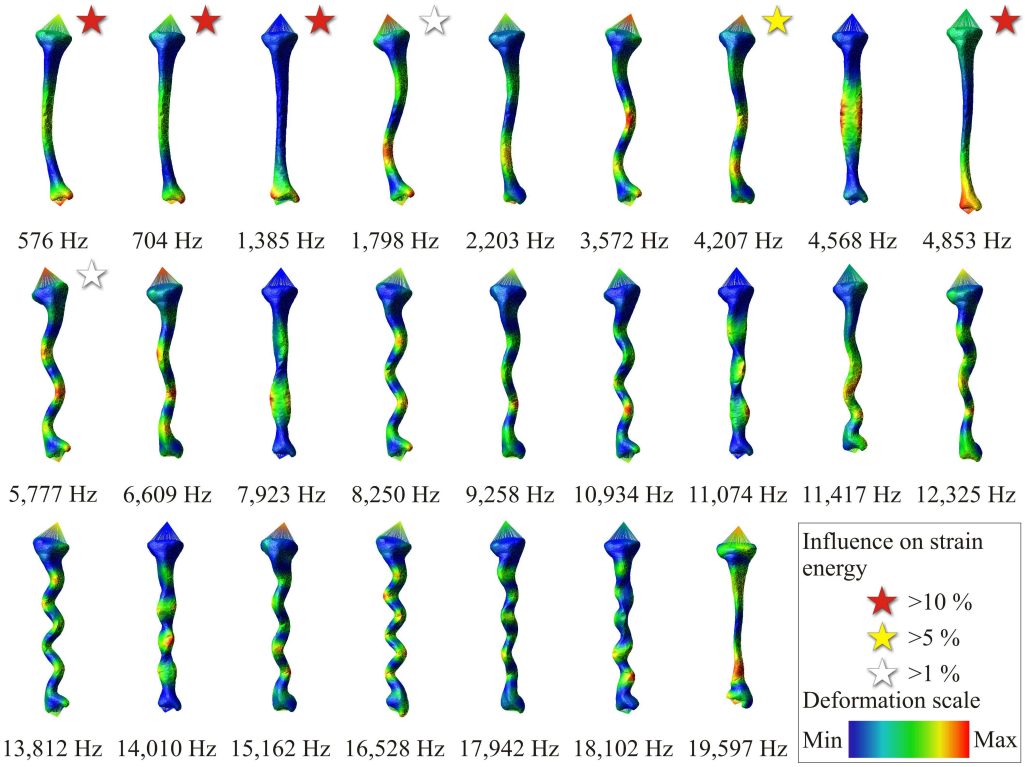

Figure 18. Deformation modes of tibia – Modes with high influence on the total strain energy are additionally highlighted.

Figure 20 shows horizontal and vertical components of the ground reaction force for the validation of the model. Principal in-plane strain values on the anteromedial surface of tibia are presented in the Figure 21. The axial strain values around the cross section of tibial midshaft are presented in Figure 22. The axial direction corresponds to the normal direction of the bone cross section. Characteristic peaks, corresponding to the heel-strike and push-off phases can be observed from Figure 21 and Figure 22. The axial strain values around the cross section of fibular midshaft are presented in Figure 23. Positive

strain values represent tensile strain, negative values compressive strain. Extreme in-plane principle strain values obtained in the current study were compared with the values found in literature (see Table 7).

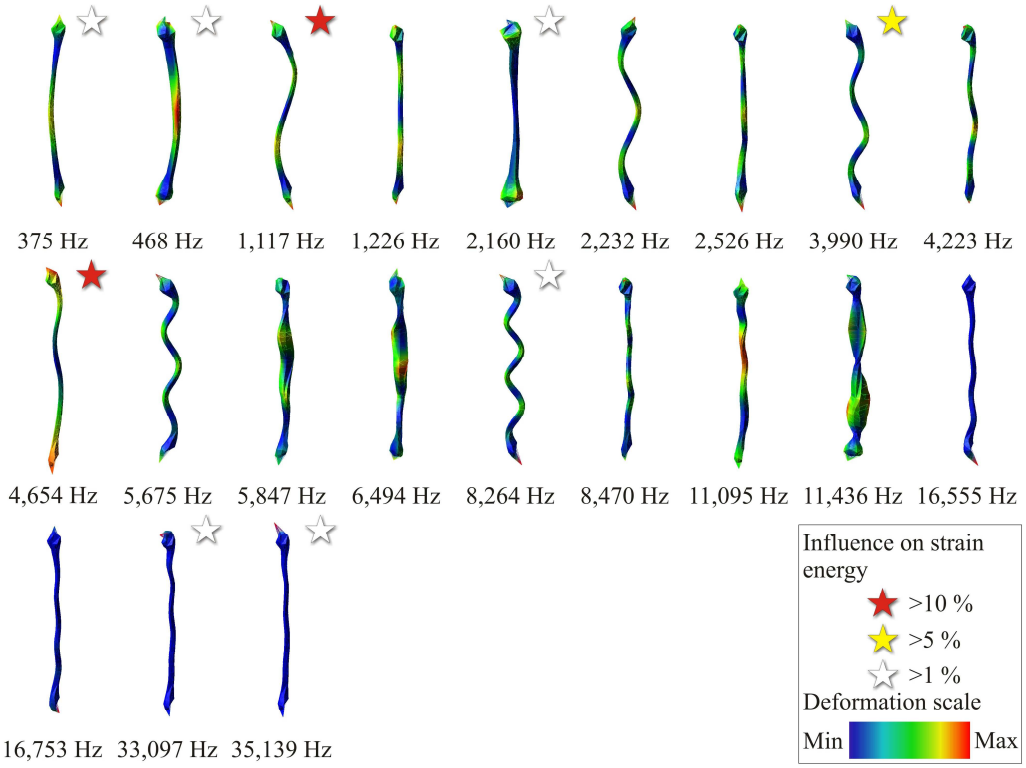

Figure 19. Deformation modes of fibula – Modes with high strain energy influence are marked with stars.

Table 7. The principal strain values obtained in the experimental and current study at the proximal aspect of the midshaft of the tibia

Strain	**(Lanyon et al., 1975) [με]**	**(Burr et al., 1996) [με]**	**(Milgrom et al., 2007) [με]**	**Current study [με]**
Max principle	395	437	342–446	622
Min principle	-434	-544	-628–716	-370
Magnitude	829	981	970–1,162	992

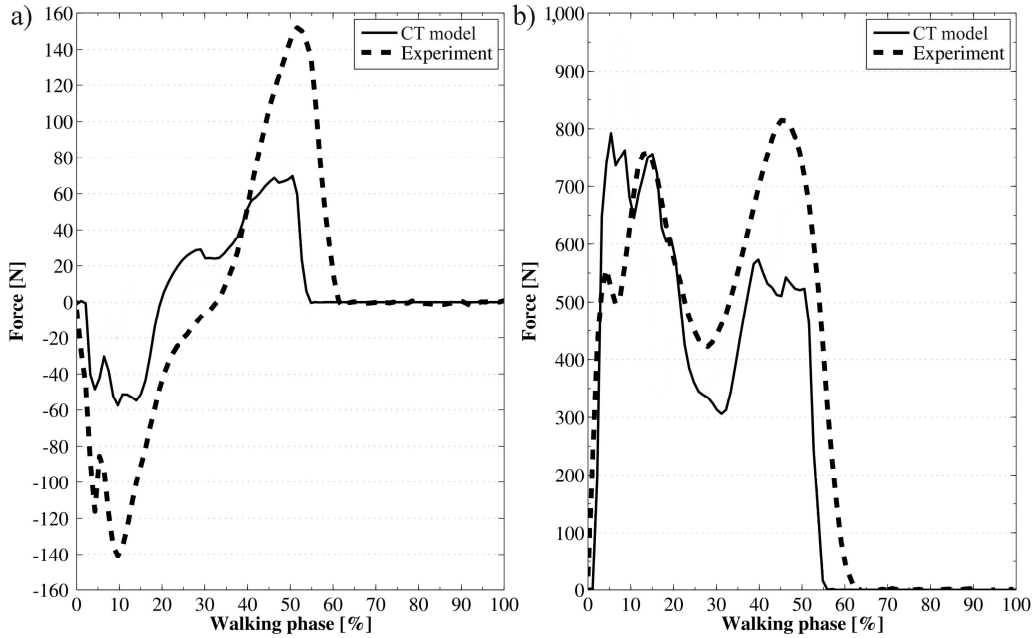

Figure 20. Components of the ground reaction force during one walking cycle: a) horizontal, and b) vertical

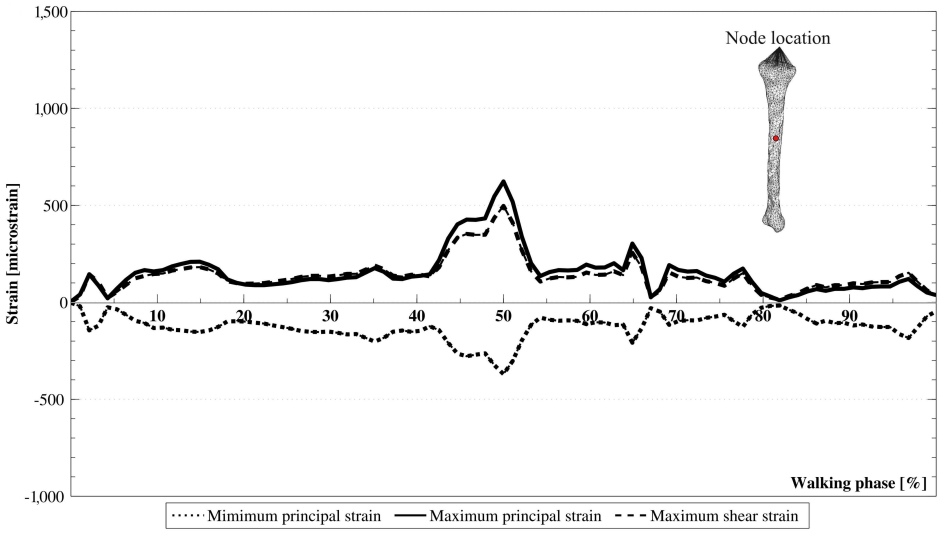

Figure 21. Principal in-plane strain values on anteromedial aspect of tibial shaft – The node location is indicated by dot.

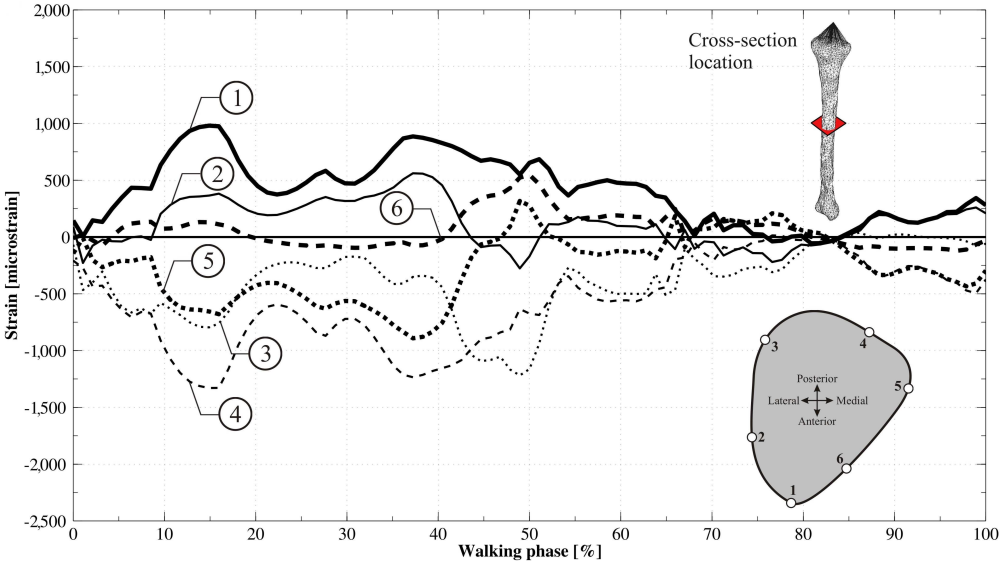

Figure 22. Axial tibial strain values in the middle cross section of the diaphysis

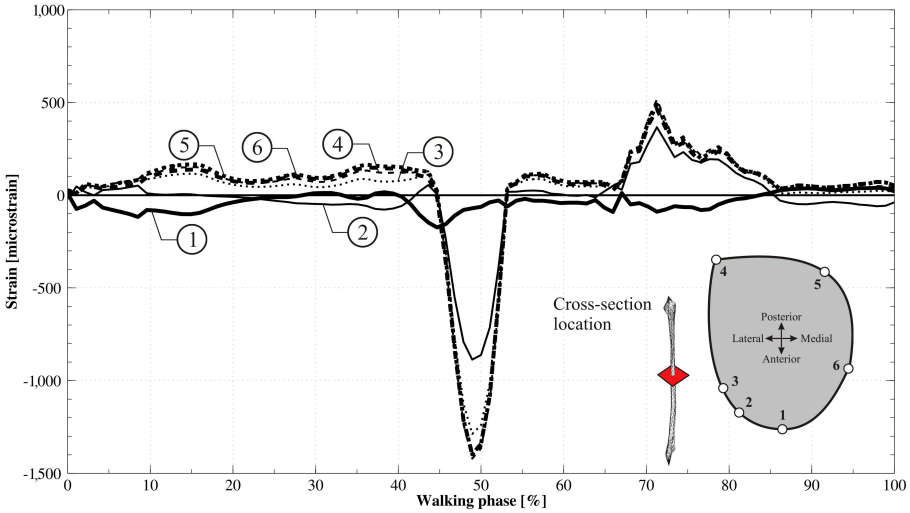

Figure 23. Axial strain values in the midshaft of fibula

3.3.3 Discussion

Strain values predicted by QCT based models (Figure 21) showed good correlation with the results of previous *in-vivo* studies. Principle in-plane strain values tend to have different zero offset in the *in-vivo* studies compared to the current study. However, the magnitude of peak strain values is within a 1.1 to 19.7 % difference depending on the study. Current bone model also indicate

bending as the dominating load during the stance phase, in line with previous findings (Biewener, 1991), (Garcia & da Silva, 2004). Forward swing phase is characterized by low strain values as it is to be expected from the fact that mostly inertia forces are acting upon tibia during this phase. Maximum and minimum axial strain for the QCT tibia model reached 980 με and -1,329 με respectively. Peak values of axial strain within the same cross section reported by (Peterman et al., 2001) are 1,185 με and -1,864 με. Apparently, the results obtained from the QCT model are well within the range of the experimental study by Peterman.

Axial strain values of the fibula (Figure 23) show the largest loading during the push-off phase. This corresponds to the highest activity of soleus muscle, which is attached to the fibula, that is, site specificity of the loading. Thus, the simulation results are in accordance with the *in-vivo* Achilles tendon force measurements (Komi et al., 1992). In addition, animal studies have shown that bone geometric adaptation is loading and direction specific (Rubin & Lanyon, 1984), which is supported by previous cross-sectional studies in human athletes (Rantalainen et al., 2010), (Nikander et al., 2008). Also, in one prospective study in growing boys (Macdonald et al., 2008) and girls (Heinonen et al., 2001) direction specific adaptation was seen at the tibia in the region of the highest strain values computed in the current study. Finally, ankle joint torque shows similar pattern with the Achilles tendon force (Silder et al., 2008).

Tibia-fibula load division is comparable with the experimental results, showing on average around 4.7 % of axial load is carried by fibula, while the experimental measurements performed by (Funk et al., 2007) state value of 8–19 %, and (Goh et al., 1992) reports the load of 7.12 % for ankle joint in neutral position.

3.4 Upper leg study

Tibial strain values evaluated in the previous section allowed for verification of the methodology against *in-vivo* measurements. However, from medical point of view, loading condition in the femoral neck is of much greater importance than loading in tibia. Femur is the largest of human bones, at the same time femoral neck, which is subjected to high loading, is relatively small zone of

femur. For this reason much higher requirements are posed for the model that could accurately predict femoral neck strain values.

3.4.1 Model description

The same subject was utilized as in case of the lower leg strain values study, thus the same motion capture data was used. Femur model geometry was reconstructed from computed tomography images of the test subject. Slice thickness was 0.625 mm, and the pixel size was 0.3906x0.3906 mm. Slices were taken with 0.31 mm spacing. Prior the scanning scanner was calibrated with standard water phantom, during the scanning procedure of the subject; additionally three phantoms containing dipotassium hydrogen phosphate (K_2HPO_4) were scanned for material model calibration purpose. Solutions concentrations were 100, 200, and 300 mg/cm^3.

Finite element representation of the femur was built using linear solid tetrahedral elements. Element size was varied from 0.5 mm up to 5 mm. Variable element size contributed to the reduction of computational effort needed to process the model. Smaller elements were used for discretization of the cortex bone at the distal ends as well as the femoral neck zone, where the strain values should be obtained. Trabecular bone was meshed with larger elements, also cortical bone along the shaft is relatively thick, and thus larger elements could be used. Finite element model of the femur with mesh sizes is depicted in Figure 24. The model consists of 331,605 elements resulting in over 196,000 degrees of freedom in total, and each element was assigned one of 1,591 material parameter sets, which were derived based on the material model connecting material properties with CT voxel values (Kłodowski et al., 2012). Differentiation between the cortical and trabecular bone was done with respect to the apparent density, where the value of 1,400 kg/m^3 was used as a threshold.

Similarly like in the previous example, the bone was subjected to modal analysis. Boundary nodes were placed at joint rotation centers of the multibody model, namely in the middle of the femoral head and in the middle of the lower extremity, thus they are not visible in the Figure 24.

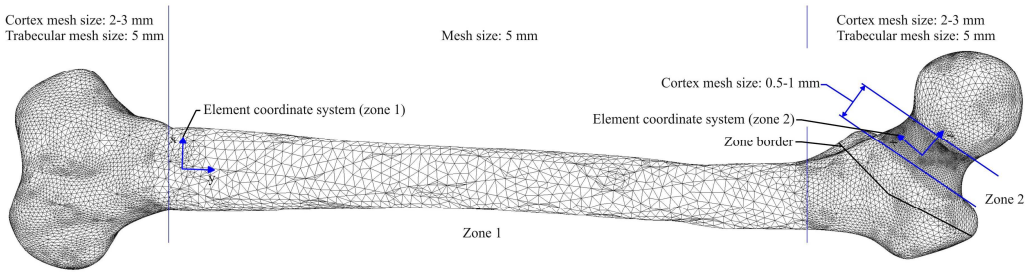

Figure 24. Discretization of the femur model with respect to bone structure and location – The femoral neck was modeled with the smallest elements. Two orientations of element coordinate systems were used; one for zone 1 and one for zone 2.

Multibody model of the musculoskeletal system of the subject was prepared using LifeMOD. The skeleton was based on the anthropometry of the subject. The initial scaling was done using weight, height, gender, age, and ethnicity. Joint locations obtained from computed tomography revealed that the further adjustment of the segments of the model is needed to fully correspond to the subject. After adjustments, kinematic joints were added to the model as well as passive recording muscle description. Motion capture data was used to drive the model in the inverse dynamics, which was the first simulation step. Following the inverse dynamics simulation, the model was modified for the forward dynamics. The modifications included replacing of the rigid femur with its flexible representation, substitution of the recording muscles with active PID versions and introducing foot-ground contact models. For the model contact stiffness was determined to be 300 N/mm, damping coefficient was 25 Ns/mm, exponent was equal to 1 and the damping depth was set to be 0.01 mm. Friction coefficient was 1 due to the static nature of friction between feet and the ground. Initial conditions for the forward dynamics simulation were obtained from the inverse dynamics results. During both forward and inverse dynamics the time step was fixed to 0.01 s and the solver used was contact optimized one.

3.4.2 Results

Thirty orthonormalized Craig-Bampton deformation modes and corresponding eigenfrequencies were computed. Size of the model resulted in 2.5 hours computation time on the desktop computer (AMD Phenom II X3 720, 2.8 Ghz, 4 GB RAM). Deformation modes computed during the finite element analysis

are depicted in Figure 25. Significant deformation modes, namely those affecting strain energy more than 1 % were highlighted with a star.

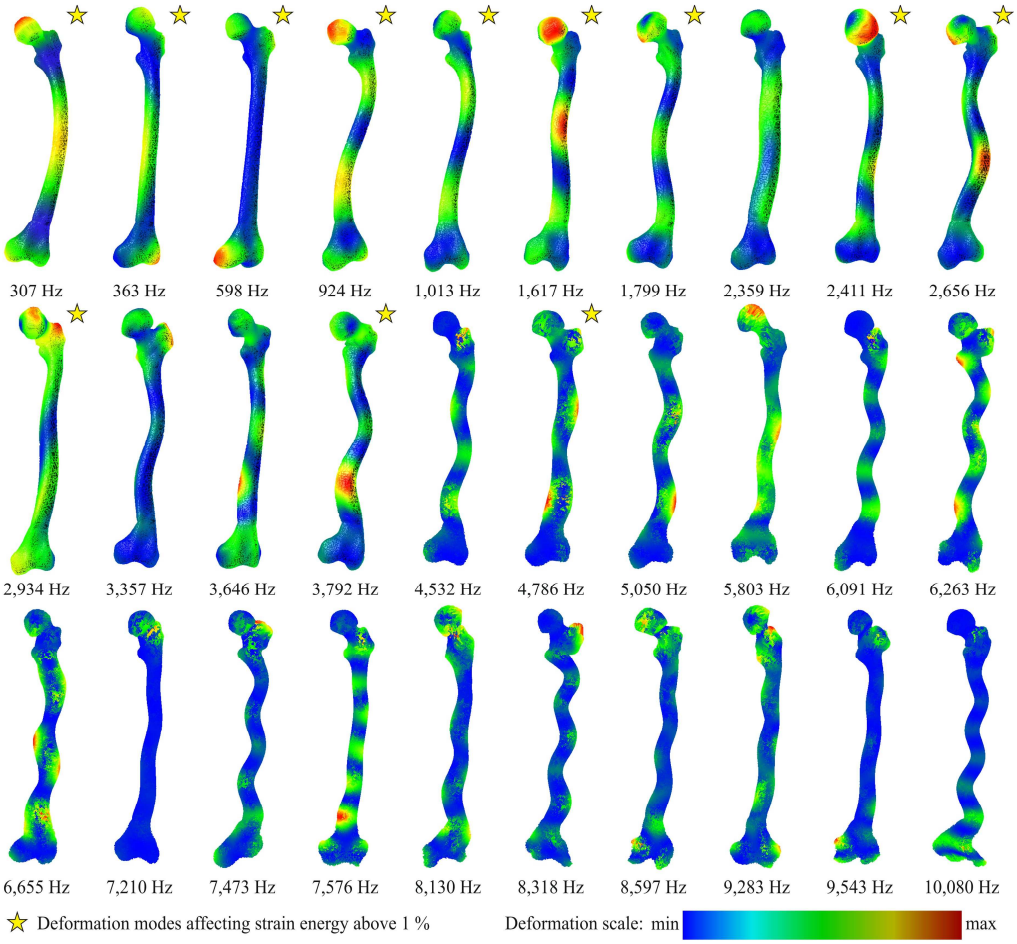

Figure 25. Femoral deformation modes obtained from the Craig-Bampton modal analysis.

During the forward dynamics simulation, ground reaction forces (Figure 26), axial strain values at the middle cross section of the femoral neck (Figure 27) and axial strain values at the proximal lateral aspect of femur (Figure 28) were computed. Ground reaction forces were used to verify the model against values measured in the gait experiment. Proximal lateral aspect strain histories were used for additional verification with the results of (Aamodt et al., 1997), who measured femoral strain *in-vivo*. The data is presented in the walking cycle domain.

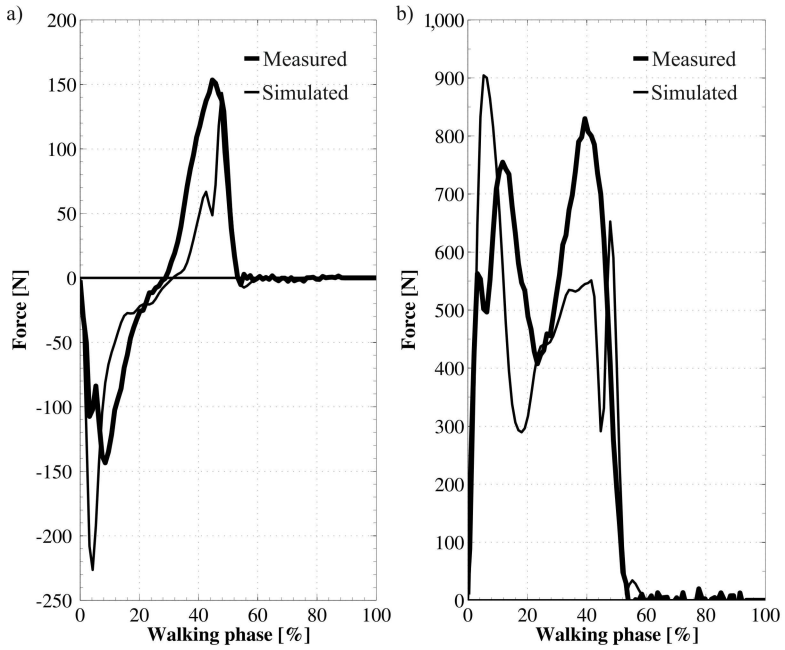

Figure 26. Ground reaction forces obtained from simulation and experimental measurements including a) the horizontal component of the ground reaction force along the walking direction, and b) the vertical component of the ground reaction force

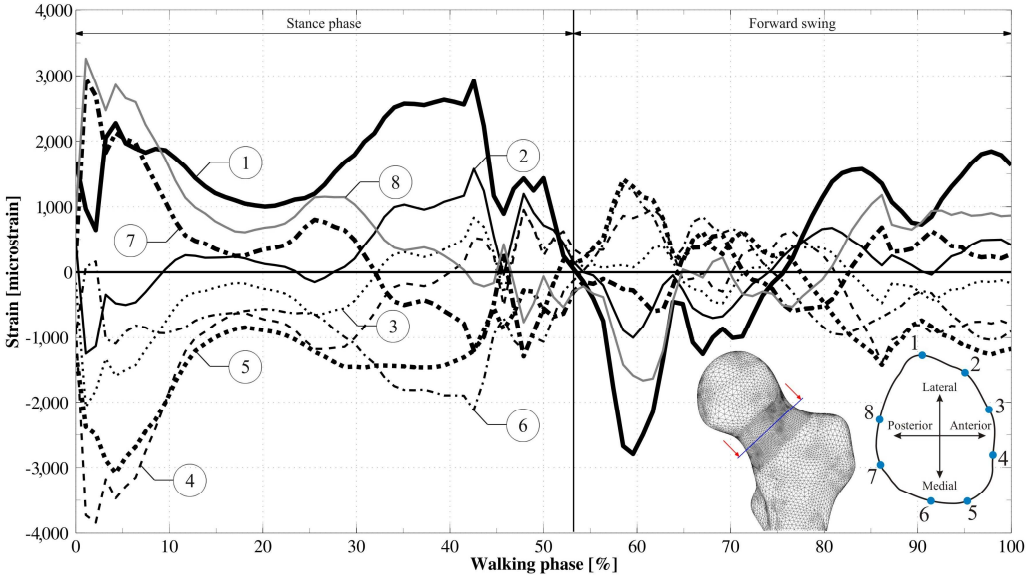

Figure 27. Axial strain values at the indicated cross section of the femoral neck during single walking phase

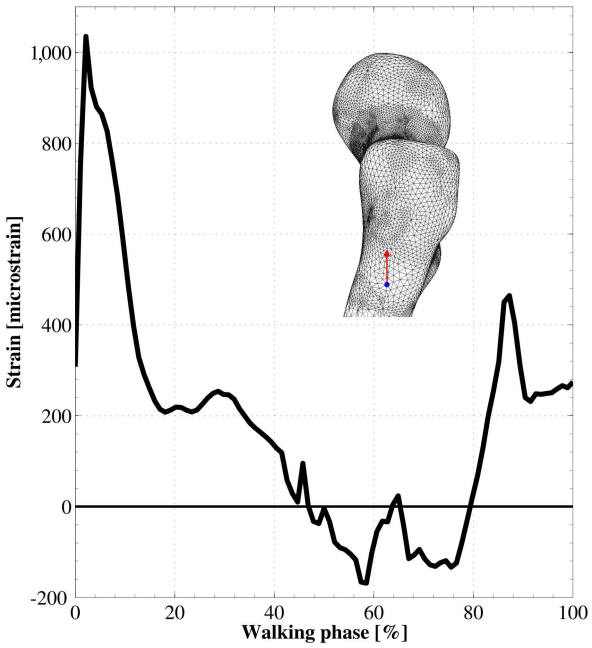

Figure 28. Axial strain values at the proximal lateral aspect of the femur during walking – The node location is indicated by the dot, and the arrow represents the direction along which strain values were measured.

3.4.3 Discussion

Verification of the model was performed using two sets of available data. Ground reaction forces obtained from the simulation were compared to values measured using force plates. The horizontal components (Figure 26a) of the ground reaction force correlate to the level of 85 %, which can be considered as a good result. Vertical component (Figure 26b) shows weaker correlation reaching 83 %. The largest discrepancy between measured and simulated vertical component of ground reaction force occurs during the push-off phase. The difference comes mostly from the simplifications in foot modeling (one rigid body), where in the reality there is some flexion of the toes during the push-off phase. Additional factor contributing to the differences is the stabilization forces needed for keeping the upright position during walking cycle.

The second verification method is comparison of the tensile strain values at the proximal lateral aspect of femur to the *in-vivo* strain measurements performed by (Aamodt et al., 1997). In this case, the simulation results depicted in Figure

28, comply with the *in-vivo* measurements – both at the level of strain pattern (correlation of 67 %) during the walking phase and also with respect to the extreme values. The maximum strain value indicated by Aamodt is on the level of 1,300 με, while in the current study it reaches 1,023 με. During the forward swing strain values are within -400 to 200 με in the cited study, while in the current research those values are within -168 to 464 με. Taking into account the average offset of the zero strain level between the studies to be 248 με during the forward swing, it can be concluded that the agreement is good. Especially taking into account that correlation of the strain results according to Aamodt's study between the averaged walking cycle and the full walking sequence is on the level of 94 %. Indicating that relatively large differences between gait cycles can be observed on a single subject. Both verification methods show that the model can give reasonable estimates of femoral strain.

Axial strain values at the femoral neck during gait cycle (Figure 27) are around three times higher than the strain values observed in the tibial midshaft. This indicates the importance of the femoral neck endurance properties in daily activities. Relatively high strain values can be explained by the geometry of the femoral neck. Its cross-sectional area is around 393 mm^2 while the cross-sectional area of tibial midshaft is close to 909 mm^2 which is 2.3 times larger than the femoral neck cross section. In addition femoral neck is most of the time caring bending load caused by the orientation of the femoral neck in respect to the shaft of the femur. In contrast to tibia which is not heavily loaded during the swing phase, femoral neck is subjected to considerable load at this phase, load that is mostly caused by muscles lifting the leg, and by the weight of the whole leg.

4 Exercise simulations

4.1 The subject

Simulations required motion capture and measurements of human subject as the input. Motion capture was used to ensure natural motion of the model. Laboratory of the University of Jyväskylä was used to conduct the experiment. The subject, who volunteered for the experiment, was Caucasian male; height 168 cm, weight 65 kg and age 25 years.

4.2 Leg press

Leg press is an exercise performed in a seated position with a backrest. The aim of the exercise is to push against the leg support, and by doing so lift weight to provide resistance. During this exercise, the most active muscles are the knee extensors and the hamstrings muscles. From a purely mechanical point of view, this exercise can be performed using either the hamstrings, the knee extensors, or any load sharing combination of those two muscle groups. In practice, the exercise is performed using both above-mentioned muscle groups at the same time, what allows minimizing the metabolical cost as well as reducing loading stresses at muscle attachment points on the bones.

4.2.1 Model description

A detailed CAD model has been created of the exercising machine for the purpose of subject model positioning and preserving kinematics. CAD model represents five parts of the machine: frame, seat, backrest, feet support, sliding support. The frame is fixed to the ground. The seat and backrest are fixed to the frame after positioning. Feet support and sliding support are fixed together, while sliding support is connected via translational (prismatic) joint with the frame. To simulate the loading history of the exercise, a single component force is applied to the sliding support. The force time history registered during experiment is used in the simulation. Illustration of the exercise machine with constraints is presented in Figure 29.

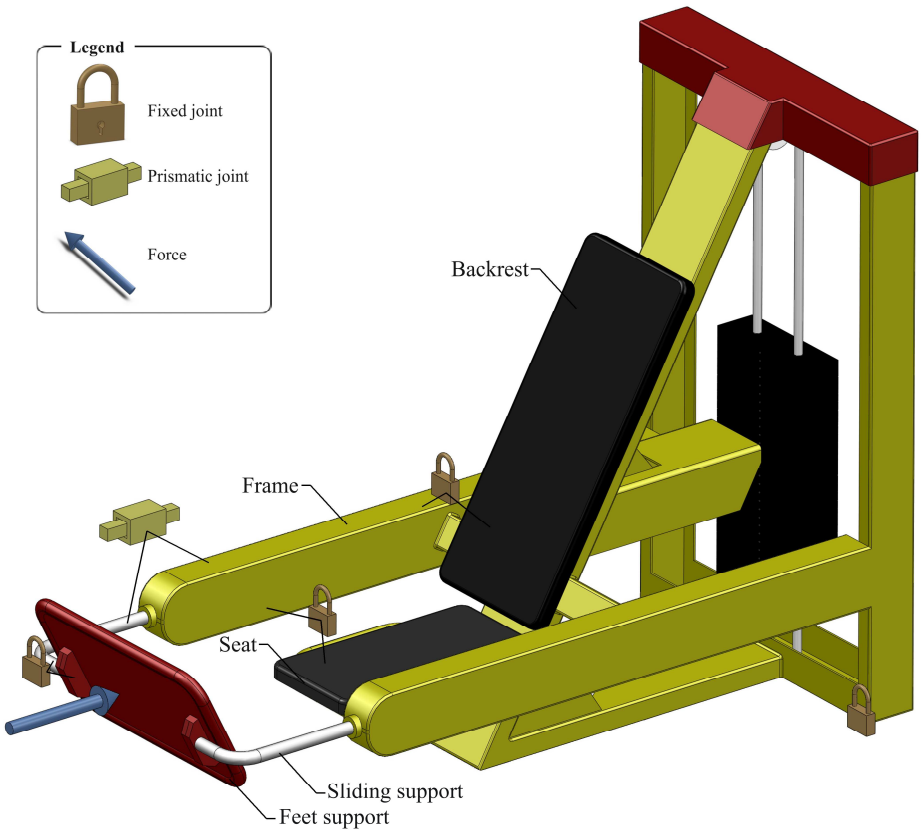

Figure 29. Leg press machine multibody model with marked external force, joints and components

The exercise was performed with the load of 90 kg, which corresponds to the highest load the subject was able to perform the full exercise cycle with. The exercise was performed with one leg, while the other leg was supported on the floor not taking the load. The linkage system of the machine transmits the force without division to the feet support. This means that a 90 kg weight results in a force of roughly 883 N in the stationary position at the foot support. The force history obtained from the experimental measurements is presented in Figure 30.

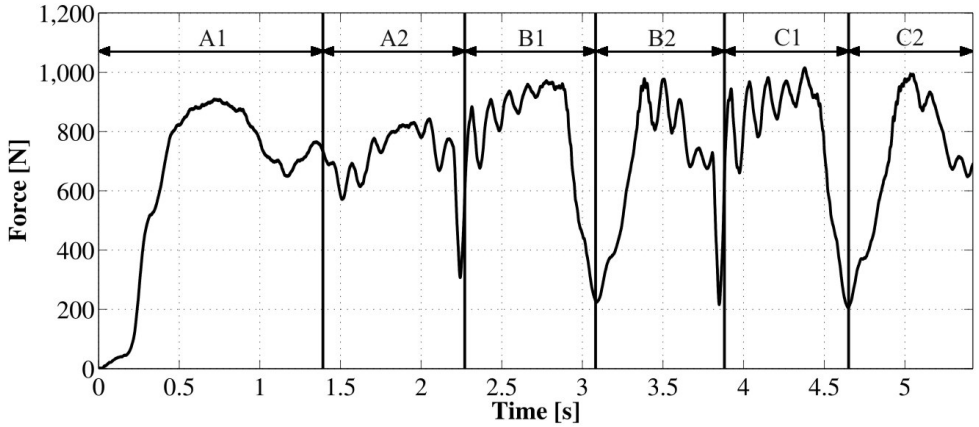

Figure 30. Rope force measured during the experiment – Sections A1, B1, C1 correspond to pressing phases; sections A2, B2, C2 correspond to retraction.

The subject was asked to perform three consequent repetitions of the exercise; each at higher speed then the proceeding one. Motion data analysis revealed only minor difference in speed between two last repetitions; however, the first cycle was clearly longer than the two remaining. Timing is presented in Figure 31. During the first phase pressing was clearly longer than retraction. Retraction times in all cycles are similar.

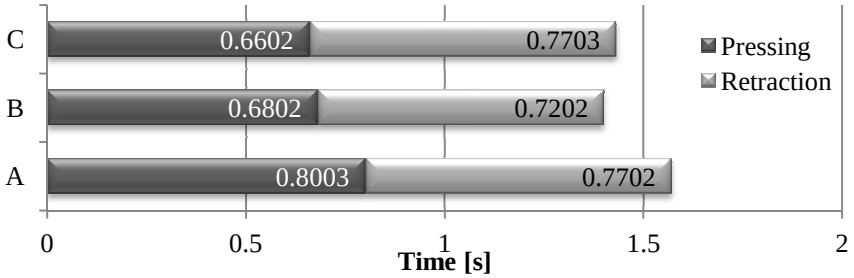

Figure 31. Leg press cycle timing – Three consequent repetitions are presented and marked A, B, C; respectively.

4.2.2 Results

Results from the simulation are axial strain values at the midshaft cross section of tibia during three repetitions of the exercise: slow (Figure 32), moderate (Figure 33), and fast (Figure 34). The magnitude of knee force is also reported (Figure 35), as this exercise is expected to produce high knee loads. Finally, knee angle time histories are reported in Figure 36 to clarify the exercise phase

time scale of the figures found in this section. Each of the figures presented in this section has distinct marks to identify loading and unloading phases of the exercise. Using the common exercise phase as the timeline eases the comparison of the results from exercises performed at different speeds. Each curve in Figure 32, Figure 33, and Figure 34 represents axial strain history at different node of the bone cross section. A legend presenting locations of the nodes in the bone cross section is included in each of the figures.

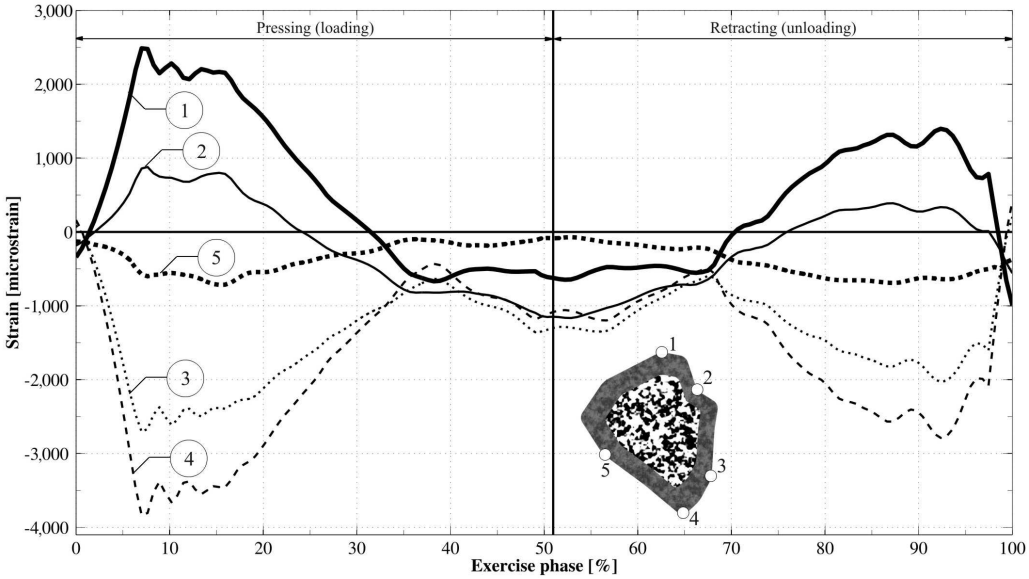

Figure 32. Axial strain values at the midshaft of the tibia resulting from slow-speed leg

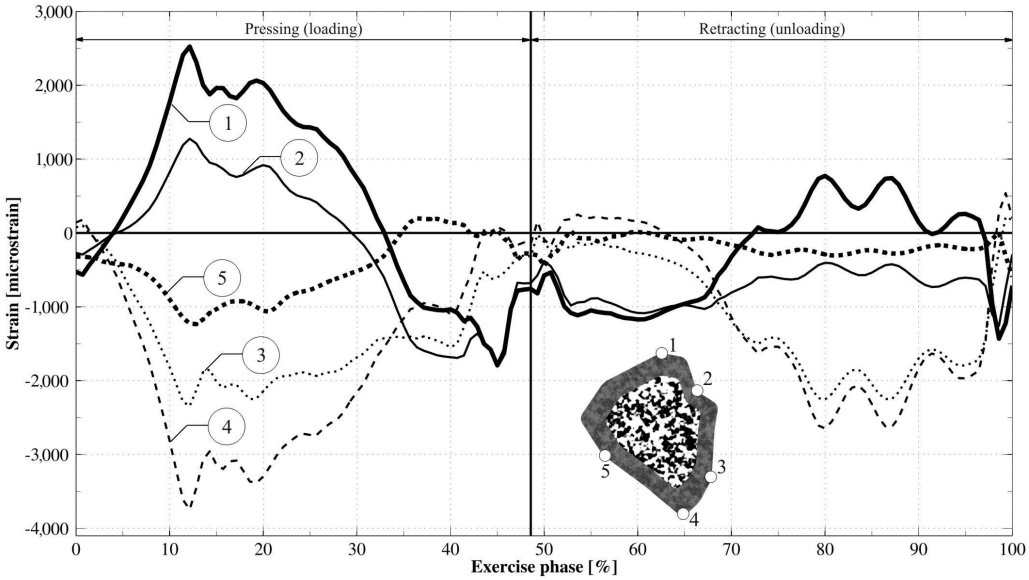

Figure 33. Axial strain values at the midshaft of the tibia resulting from moderate-speed leg press

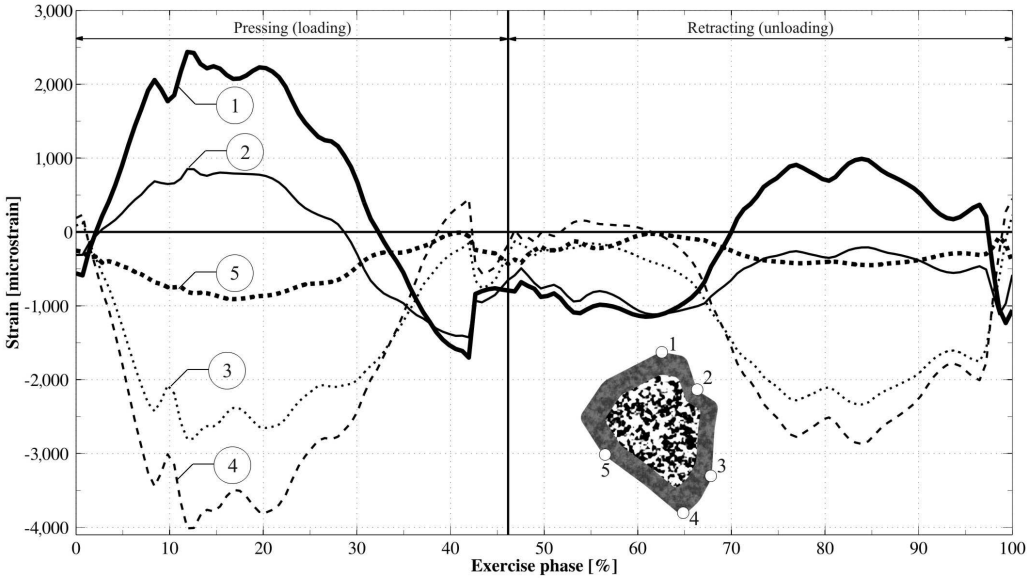

Figure 34. Axial strain values at the midshaft of the tibia resulting from high-speed leg press

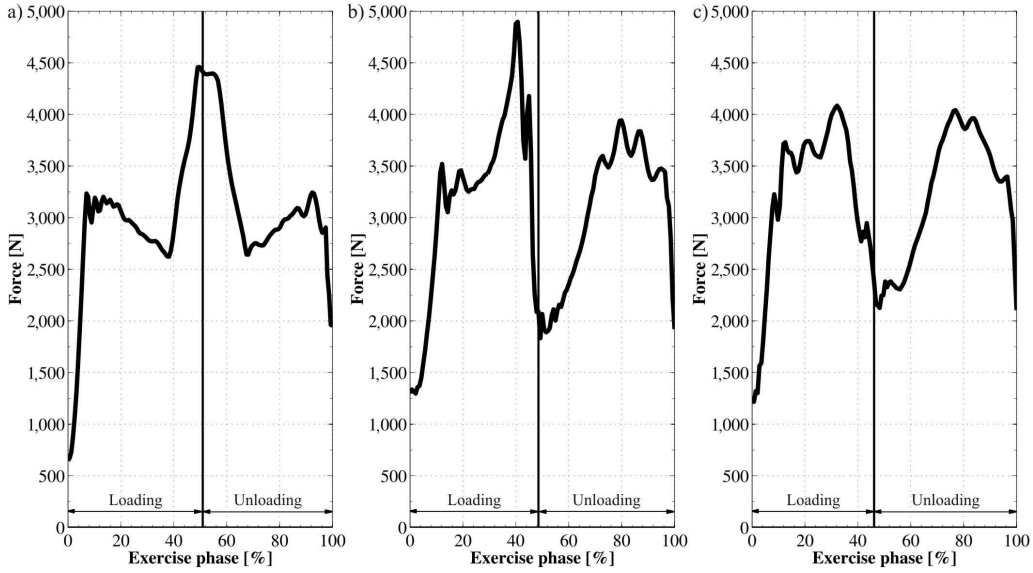

Figure 35. Magnitude of knee force during leg press exercise performed at a) low, b) moderate, and c) high speed

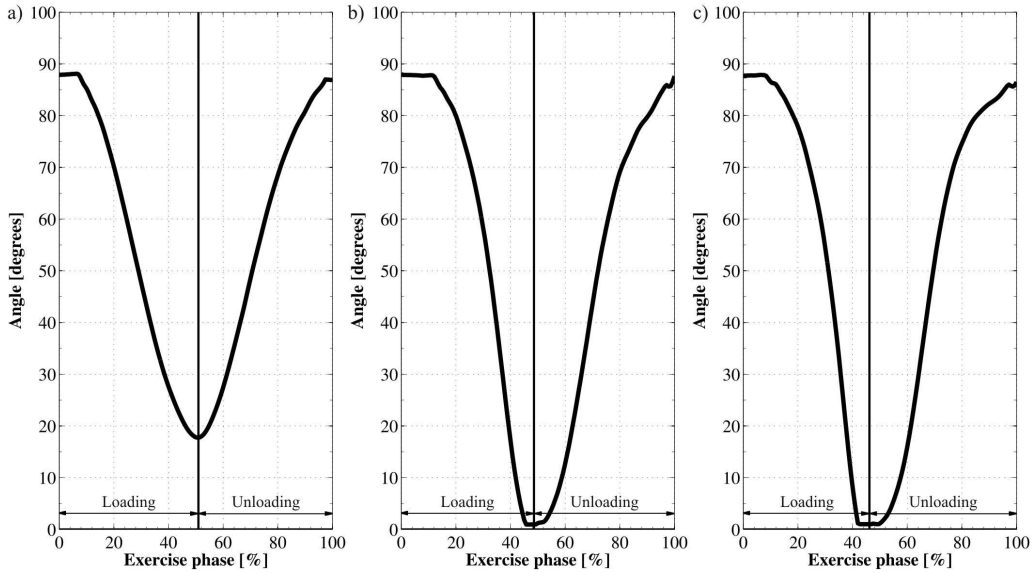

Figure 36. Left knee angle time history during leg press exercise performed at a) low, b) moderate, and c) high speed

4.2.3 Discussion

Leg press exercise indicates high dependency of tibial strain values on knee angle. For the straight leg, corresponding to the knee angle of 0°, the strain

values are comparable to peak strain values in walking. Angle of about 30° is the limit when the strain values exceed 1,000 με. This finding points out the constraints that should be applied for the knee angle if the exercise is performed by a person with weaker bones or knee joint problems. Design of the leg press machine so that knee angle joint could be controlled in addition to the external load, would allow using higher loads to strengthen the bones, at the same time protecting the joint from overloading. The increase of bone deformation with the increasing knee angle is a result of short muscle moment arms, which to generate torque necessary to produce the desired motion, create significant amount of extra forces. This explains the highly non-linear dependency of bone strain values to the knee angle.

The highest strain values occur at the initial phase of the exercise, which correspond to the deep knee flexion. It is caused by the need of extra force to accelerate the load in contrast to the final stage of the unloading phase. Peak tensile loading phase strain values are on average between 75 % and 209 % higher than the peak unloading strain values. In case of compressive strain values the differences are within 36 % to 41 % only. The differences increase with the speed. Significant difference can be observed between slow motion exercise and exercise performed at higher speeds. The peak knee force occurs in slow motion at the knee angle of 0°, while in case of faster motion this point correspond to the lowest strain values. It can also be observed in Figure 33 and Figure 34 that holding the load at extreme positions result in some oscillation in strain response. This behavior is a result of contact force variation, caused by non-smooth motion, which is a consequence of muscle activation being close to the limits of the muscles. Exercise performed at higher speeds is characterized by proportionally longer phase with low strain values around fully extended knee.

4.3 Knee flexion

Knee flexion exercise is performed in a seated position with a resistive load applied at the lower end of the tibia. Longer lower limbs result in higher knee loads during the exercise. The simulation of knee flexion was performed to determine the strain values at the tibial midshaft cross section and compare them with the knee forces.

4.3.1 Model description

Full-body motion capture of knee flexion exercise was performed. Two load cases were assumed. Due to inability of the subject to perform complete knee flexion with higher load, only one load case (25 kg) is presented. The exercise was performed three times with different speed: low, moderate and high. There was no means of controlling the speed except personal feeling of the subject.

In addition to performing the full-body motion capture, wire tension force versus time in the weight support mechanism was registered for further use in the simulation. To preserve geometrical exercise conditions a detailed exercising equipment CAD model was created. To ensure exact subject positioning on the machine in the simulation, motion capture global coordinate system was associated with the machine. Motion capture was performed using four high-speed cameras placed around the subject. Synchronization of motion data with tension sensor time series was achieved by common triggering system. During the exercise, a muscle bipolar surface electromyogram (EMG) was recorded for the rectus femoris, tibialis anterior, soleus, gastrocnemius, and vastus lateralis muscles for simulation validation and in case the data is needed for open-loop muscle control.

Exercising machine was modeled as a set of seven rigid bodies: frame, seat, backrest, passive leg support, swing-arm, leg length adjuster and active leg support. The stiffness of the machine is relatively high, thus such assumption is justified. Frame, seat, passive leg support, and backrest were fixed together and the frame was attached to the ground. The swing arm was attached to the frame by a revolute joint, leg length adjuster was fixed to the swing arm and active leg support was attached via revolute joint to the leg length adjuster. Illustration of the machine with constraints is presented in the Figure 37.

Active leg support and torque direction was adjusted depending on the exercise type. The torque was applied to the swing arm simulating the loading condition. The torque history was obtained by multiplying the tensile forces in the rope history by the pulley radius. Modeling the force acting upon leg by using torque at the revolute joint of the swing arm, allows disregarding modeling of linkage system that transmits the load in the real device.

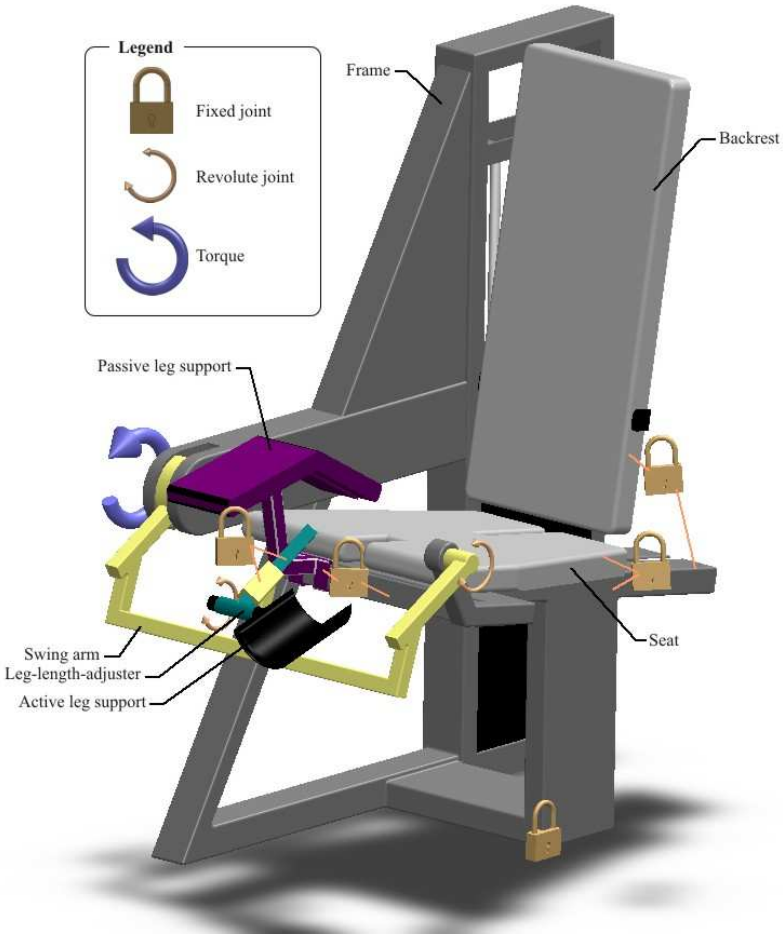

Figure 37. Knee flexion/extension machine multibody model with labeled elements – Joints and external torque are indicated by symbols.

4.3.2 Results

Axial strain values at the midshaft cross section of the tibia are presented for the three speeds at which the exercise was performed: low (Figure 38), moderate (Figure 39), and high (Figure 40). Each curve in the figures corresponds to a different point on the cross section, as shown in the graphical legend for each of the figures. The presented timeline represents the exercise period, which is divided into loading and unloading phases. Finally, knee force histories during the exercise are presented in Figure 41.

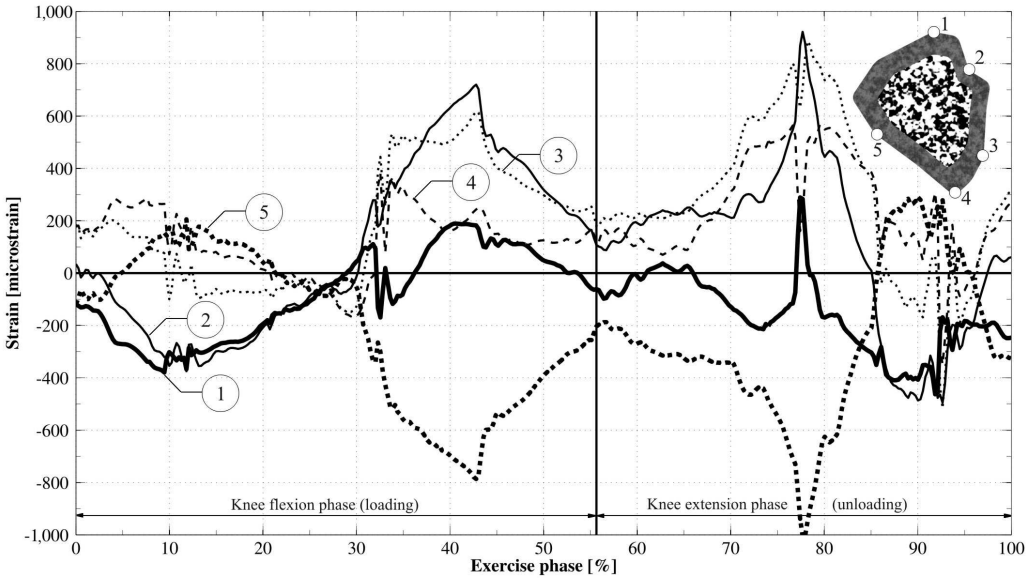

Figure 38. Axial strain values at the middle cross section of the tibia during knee flexion performed at low speed

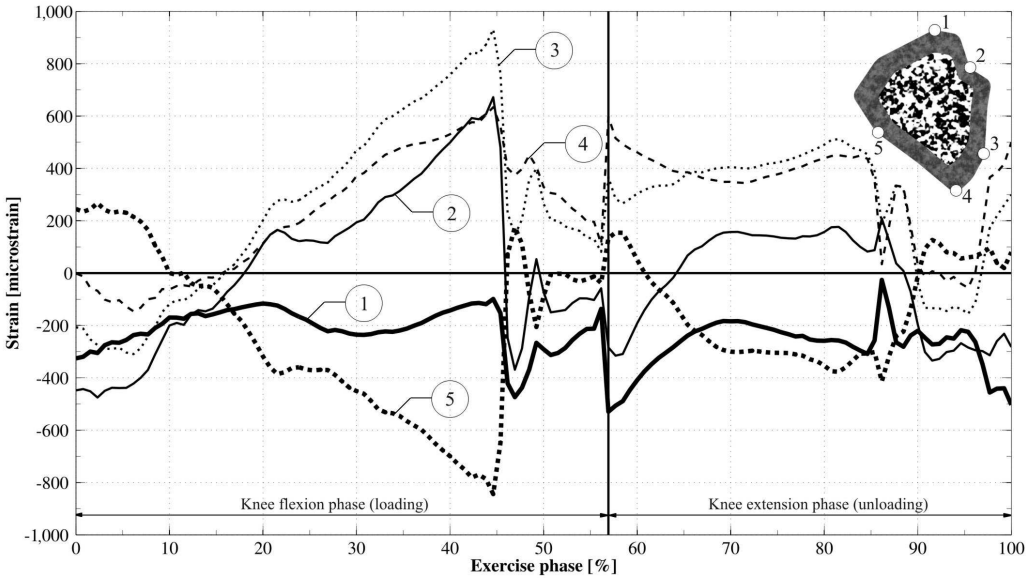

Figure 39. Axial strain values at the middle cross section of the tibia during knee flexion performed at moderate speed

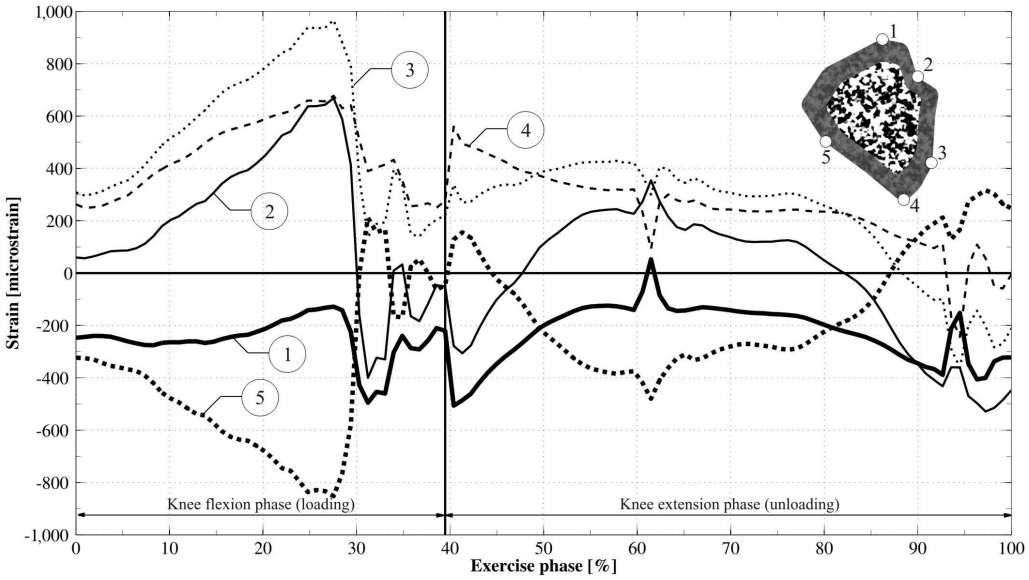

Figure 40. Axial strain values at the middle cross section of the tibia during knee flexion performed at high speed

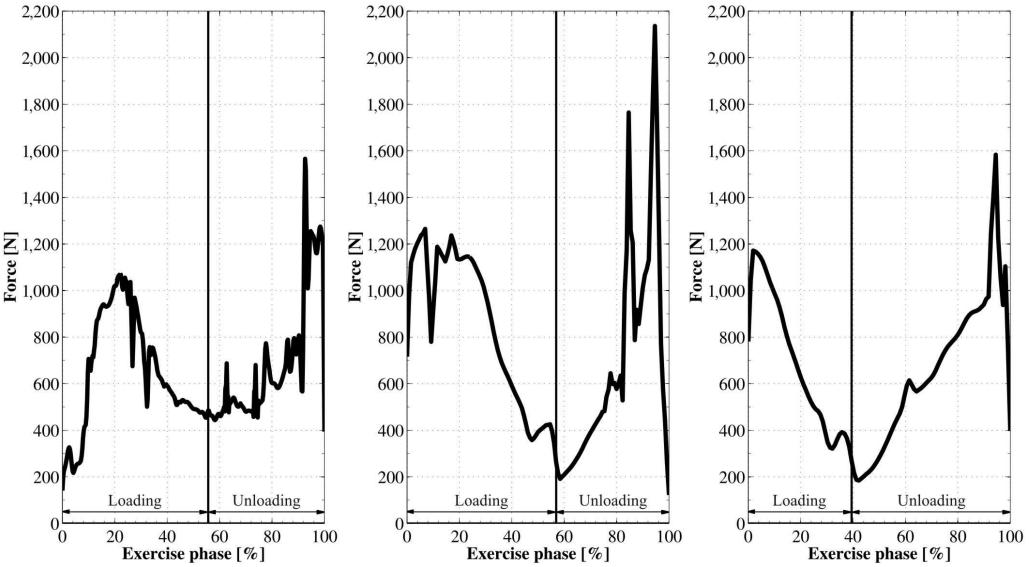

Figure 41. Knee force during knee flexion performed at a) low, b) moderate, and c) high speed

4.3.3 Discussion

Knee flexion exercise is performed mostly using knee flexor muscles with some aid from the knee extensors. Knee flexor muscles are attached to the tibia close

to the knee joint. This implies relatively short moment arms of the muscles, and thus need for relatively large muscle forces. The moment arms are approximately equal to the radius of the tibia. Comparing them to the length of tibia gives the lever ratio in a range of 1:7. The knee force however is lower than the value resulting from simple load times muscle lever ratio computation, due to the orientation of the leg in the gravity field, which causes that the mass of the leg actually reduces the force which has to be produced by muscles. This can be seen from the Figure 41, while the computation value for the knee force would be in a range of 1,700 N, the knee force is actually smaller, what in particular can be seen in the slow loading case. As the loading speed increases and the unloading time shortens, the peak knee force increases. In the loading phase, the maximum increase of the force related to the velocity change reached just 22 %, while during the unloading phase it reached 36 %. Nevertheless the unloading peak forces in the knee are short time only. While the forces caused by acceleration of the load maintain high for significant fraction of the loading phase. Comparing the knee force results (Figure 41) with the strain results at tibia (Figure 38, Figure 39, Figure 40), leads to the conclusion that knee force and tibial strain values are well correlated. However, the damping effect of the flexible bone model smoothes out the peak knee forces. Thus the peak knee force occurring during the unloading phase does not actually result in the peak strain values at tibia. The highest strain values in the slow motion can be observed during the unloading phase. Nevertheless, increasing the speed of motion, results in shifting the peak strain values to the loading phase of the exercise. This means that the effort required for slowing down the moving load can be more significant than the loading phase in terms of bone strengthening in case of quasi-static exercise conditions.

4.4 Knee extension

From mechanical point of view, the knee extension exercise is similar to the knee flexion exercise, differing only in the direction of the resistive force. The roles of the muscle groups change. In the knee extension, the knee extensor muscles are mostly active, and the knee flexors provide braking during the unloading phase.

4.4.1 Model description

The same exercising machine (Figure 37, page 89) was used for knee extension as for knee flexion. Adjustments were made to reverse the loading direction and the active leg support was flipped to the other side. The simulation procedure was analogous to the simulation procedure for knee flexion. Exercise was performed by the same subject, thus the same skeletal model was used. Exercise was performed at three different speeds freely chosen by the subject.

4.4.2 Results

The simulation results were grouped according to the speed at which the extension occurred, and ordered according to ascending speed. The exercise was performed at two loading cases, with 30 and 40 kg of dead load respectively. Axial strain values were observed at midshaft cross section of tibia during exercise performed with 30 (Figure 42, Figure 43, and Figure 44) and 40 kg (Figure 45, Figure 46, Figure 47) of external load. All figures represent the data in normalized exercise phase, where 0 % corresponds to the initial configuration with knee angle equal to 90°, and 100 % corresponds to the same position at the end of repetition. The maximum knee extension (leg in straight position) is achieved between 40 and 60 % of the exercise phase. This place is marked by vertical line in all the figures in this section. Knee forces during the exercise performed with 30 kg of load are presented in Figure 48. For the higher load the knee forces are presented in Figure 49. To illustrate the time spans of exercise phases Table 8 was prepared. Extreme strain values are reported in Table 9, with the division to loading and unloading phases, external load, and speed.

Table 8. Loading and unloading times for the knee extension

Exercise test case	Speed	Loading time [s]	Unloading time [s]
with 30 kg load	Slow	1.81	1.30
	Moderate	0.56	0.64
	Fast	0.50	0.69
with 40 kg load	Slow	1.76	1.36
	Moderate	0.62	0.67
	Fast	0.56	0.79

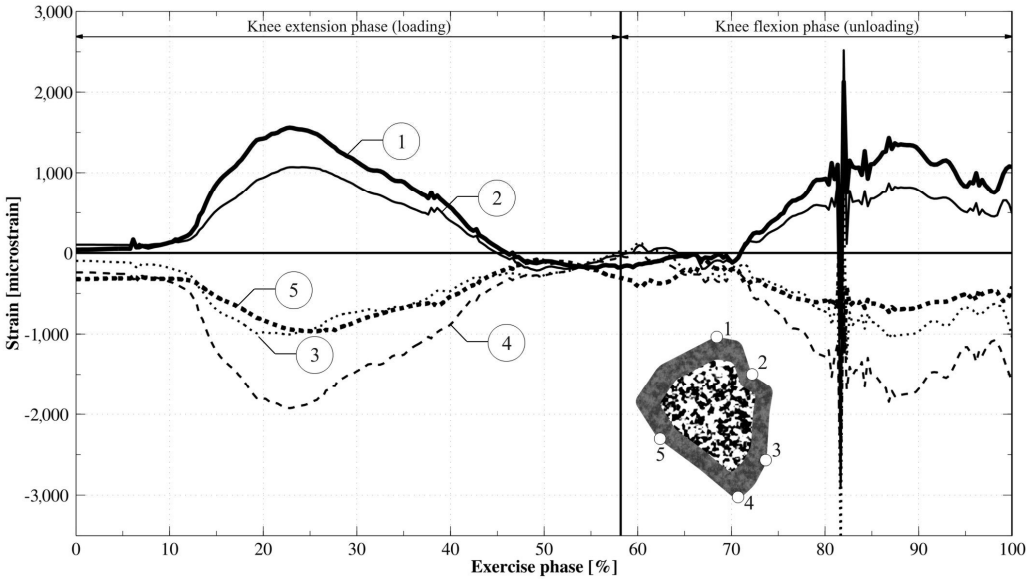

Figure 42. Axial strain values at the middle cross section of the tibia during knee extension with a 30 kg load performed at low speed

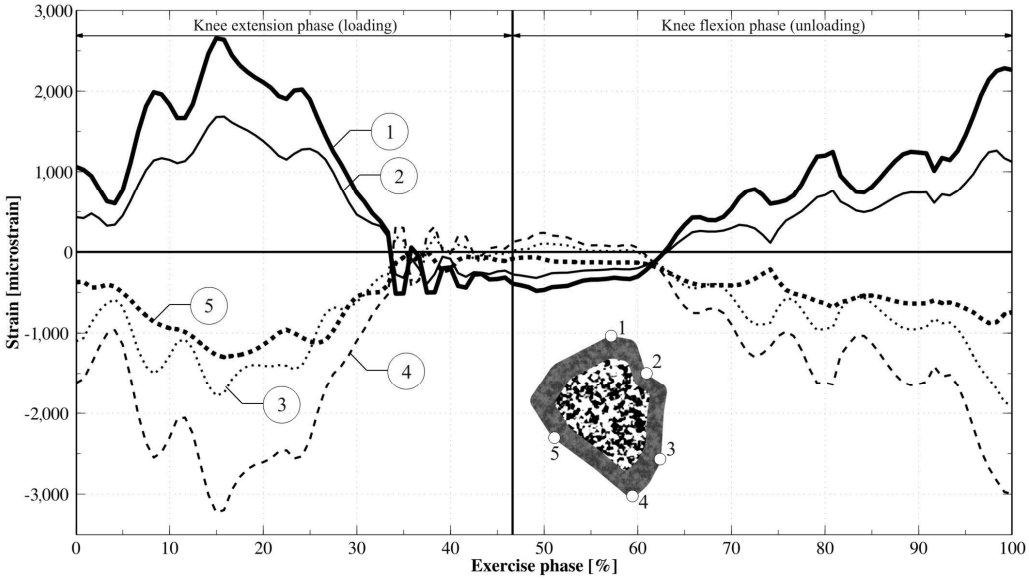

Figure 43. Axial strain values at the middle cross section of the tibia during knee extension with a 30 kg load performed at moderate speed

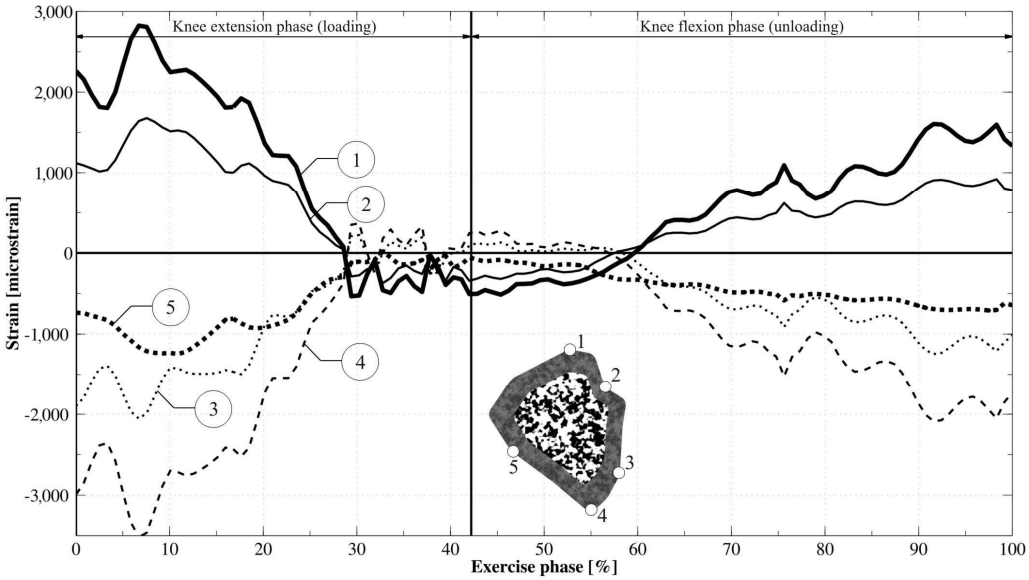

Figure 44. Axial strain values at the middle cross section of the tibia during knee extension with a 30 kg load performed at high speed

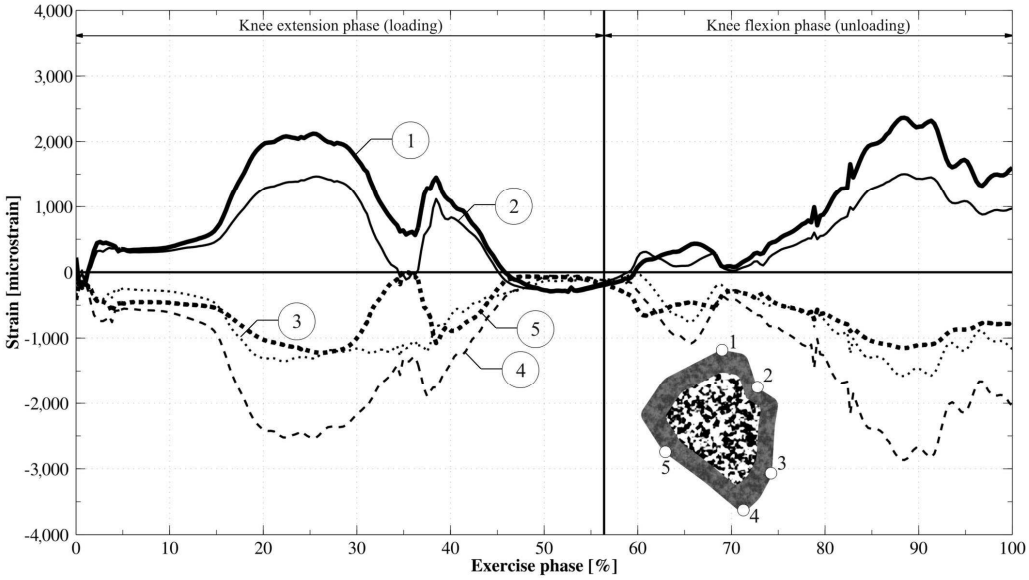

Figure 45. Axial strain values at the middle cross section of the tibia during knee extension with a 40 kg load performed at low speed

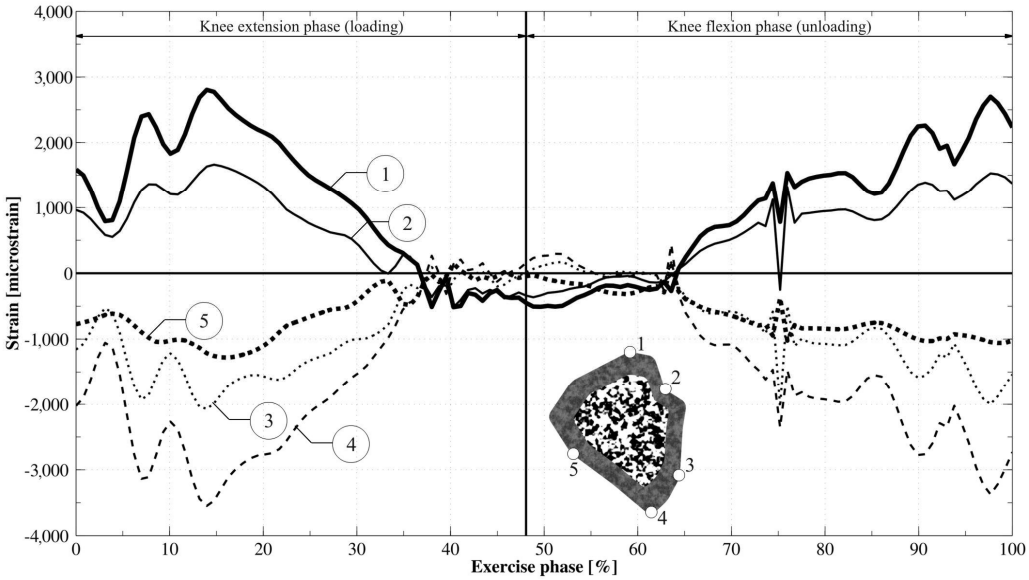

Figure 46. Axial strain values at the middle cross section of the tibia during knee extension with a 40 kg load performed at moderate speed

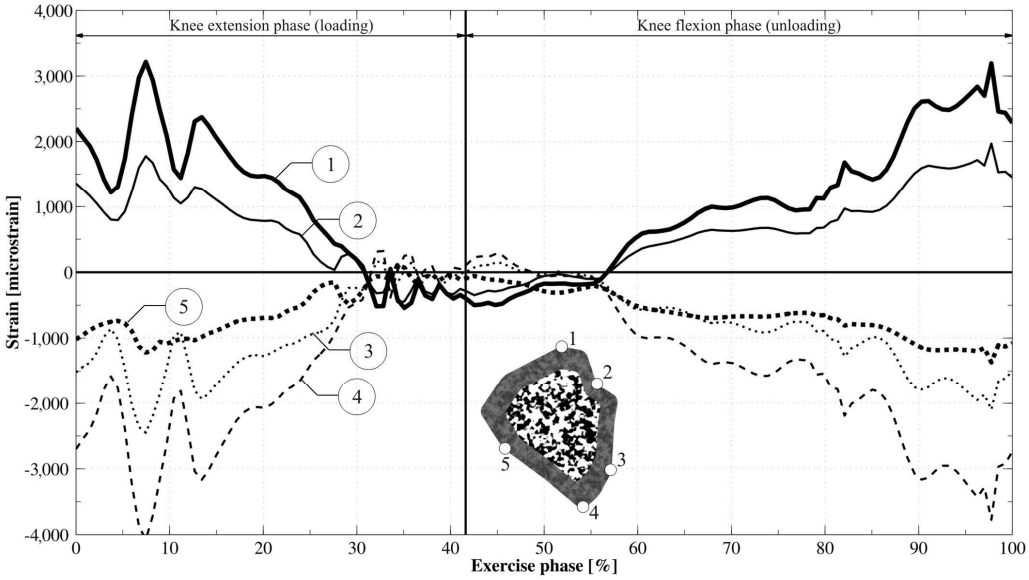

Figure 47. Axial strain values at the middle cross section of the tibia during knee extension with a 40 kg load performed at high speed

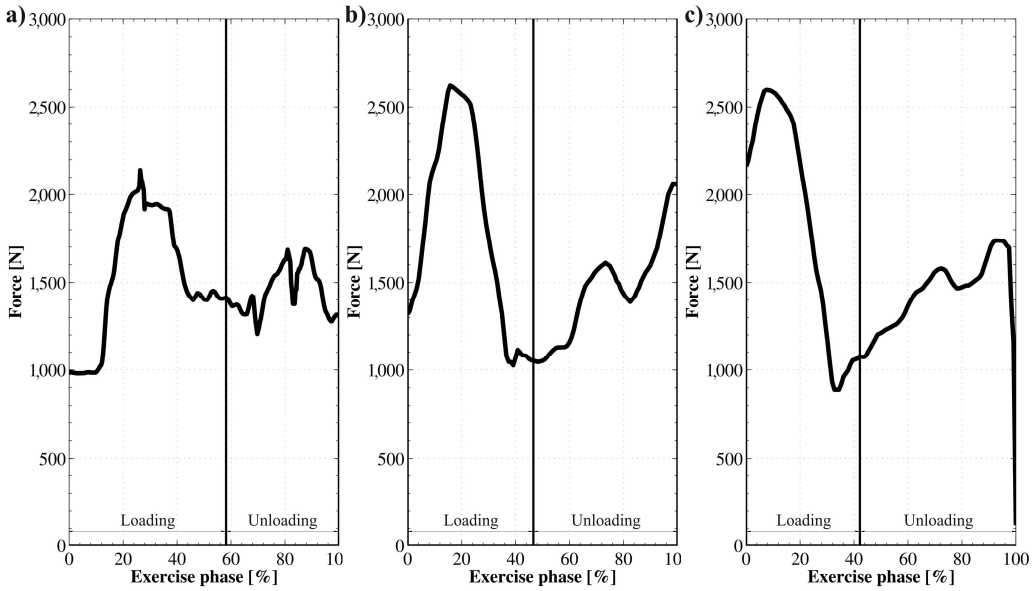

Figure 48. Knee forces during knee extension with a 30 kg load performed at a) low, b) moderate, and c) high speed

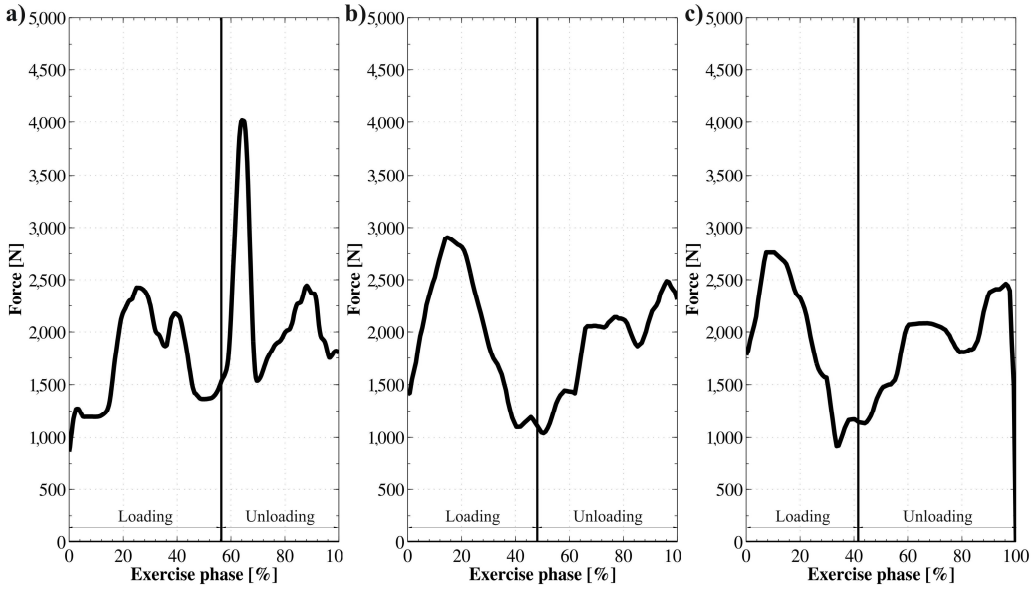

Figure 49. Knee forces during knee extension with a 40 kg load performed at a) low, b) moderate, and c) high speed

Table 9. Extreme strain values during knee extension exercise

	Speed	***Slow***		***Moderate***		***Fast***	
Load	**Phase**	**min [με]**	**max [με]**	**min [με]**	**max [με]**	**min [με]**	**max [με]**
30 kg	loading	-1,925	1,555	-3,226	2,655	-3,518	2,823
	unloading	-1,845	1,431	-2,996	2,282	-2,074	1,604
40 kg	loading	-2,536	2,121	-3,548	2,805	-4,077	3,215
	unloading	-2,866	2,363	-3,373	2,700	-3,775	3,193

4.4.3 Discussion

Knee extension in contrast to knee flexion exercise imposes higher muscle loading, as in addition to the external load, the weight of the lower leg and foot create extra resistance. Despite that, human knee extensors are capable of producing higher forces than knee flexor muscles, as can be seen by 60 % increase of the maximum resistance load during this exercise with respect to knee flexion. External load increased with respect to knee flexion by 20 % results in double the knee force. This means that knee extension is generally easier to perform, however loads the knee joint heavier. Knee extension is more symmetric exercise in terms of tibial strain values during the loading and unloading cycle with respect to knee flexion. Peak strain values can be observed at the initial and final phase of the exercise, and in the case of slow or moderate speeds, the peak strain values are similar. Exercise performed fast shows decrease in the peak unloading strain with respect to the loading peak strain.

Analyzing the timing (Table 8) and peak strain values at tibia (Table 9), it can be concluded that timing to strain relationship is highly non-linear. For instance decreasing the loading time by 69 % with 30 kg of load will result in 71 % increase of peak loading tensile strain values, 72 % decrease of the loading time with the same load will lead to 82 % increase of peak loading tensile strain values. However, when the load is increased to 40 kg, 65 % and 68 % decrease in loading time will result in only 32 % and 52 % increase of the peak tensile loading strain values. The rate at which compressive peak strain increase with the increase of exercising speed with 30 kg of load is 40 % higher than for tensile strain values. When the load is increased to 40 kg, the difference decreases to just 8 %. When loading approaches the maximum the person can handle, the muscle shielding effect is noticeable. Muscles on the tensile side of the bone are contracting reducing the tensile load, which is more likely to cause fracture.

4.5 Squat

Squat is an example of unconstrained exercise with fully three-dimensional motion. The balancing in this exercise is more complex when it is performed with external weight. For the purpose of this study a squat exercise with 70 kg of external loading was performed. The amount of external load was the maximum load the subject could handle. The subject performed the exercise twice, with two different speeds of movement.

Tibia loading, in this particular exercise, is a result of the gravity force and the exercise weights acting on the human body. Since the person is standing, muscle forces required for balancing need to be added to the total load. Moreover, muscle forces needed for actuation of the skeleton to perform the desired motion result in significant bone loading.

4.5.1 Model description

Weights and bar was modeled as rigid bodies, which were combined with the human model. The whole-body musculoskeletal model was constructed based on weight, height, age, and gender of the subject. Human model consisted of 19 bodies: two legs (each consisted of three segments: upper leg, lower leg and foot), lower torso, central torso, upper torso, neck, head, two arms (each consisted of four segments: scapula, arm, lower arm, hand). All the segments, excluding the left lower leg, were modeled as rigid bodies. The left tibia was modeled as a flexible body, allowing for strain estimation during the simulation. In addition to the skeleton, dumbbell bar and three pairs of weight plates were modeled of the total mass of 70 kg. The skeletal model was actuated by 122 PID controlled muscles.

The dumbbell bar was attached to the hands by rigid joints. Similarly the weight plates were rigidly attached to the dumbbell bar. Skeletal joints were described as defined in Table 5, page 21. The feet were attached to the ground using bushing joints to take into account the damping effect of the balls of the feet. Bushing joints stiffness was assumed to be 200 N/mm. The model overview is presented in Figure 50.

Rigid attachment of the dumbbell bar to the hands is justified, as the focus of this simulation was on tibial strain. For that reason, modeling of the friction forces and grip would be an unnecessary computational effort. The dumbbell

bar model and the weights model allow adding realistic forces coming from the inertia of the weights and the bar. In the case of these external loads, which approach the mass of the subject, neglecting inertia is not an option.

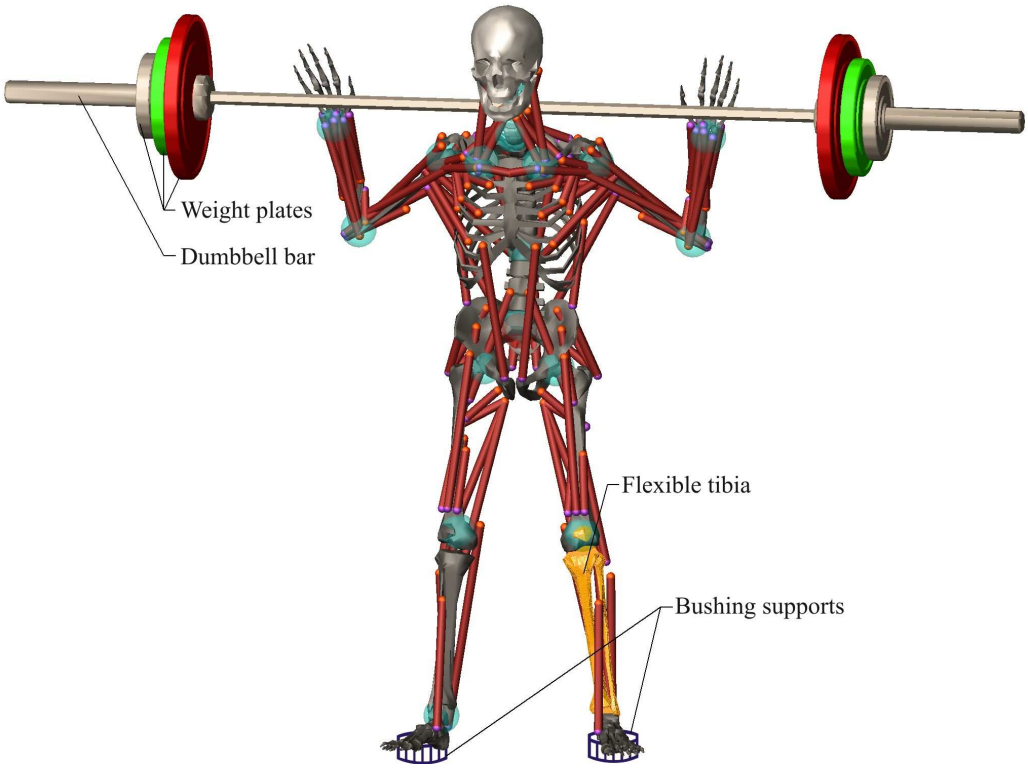

Figure 50. Overview of the multibody model used in the simulation of squatting with 70 kg of external load – The thick red lines represent muscles and the green spheres represent joints.

4.5.2 Results

The ground reaction force measured during the experiment for both legs was identical. For this reason, only one curve is used to represent the measurement data in Figure 55. The exercise timing values are presented in Figure 51. Computed axial strain values at the midshaft cross section of the left tibia are presented in Figure 52 and Figure 53 for slow and fast motion, respectively. Each curve in the figures represents strain at a single point of the cross section. Reference for point location on the cross section is embedded in each of the figures. Solid vertical line is used to indicate the transition point of the exercise

between down and up phase. Magnitudes of knee forces during the exercise are presented Figure 54.

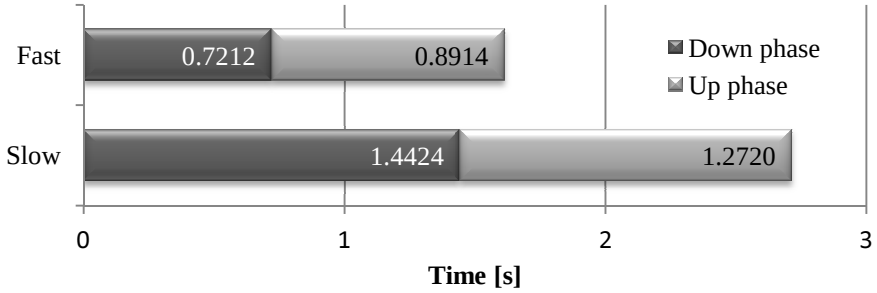

Figure 51. Timing of squat phases

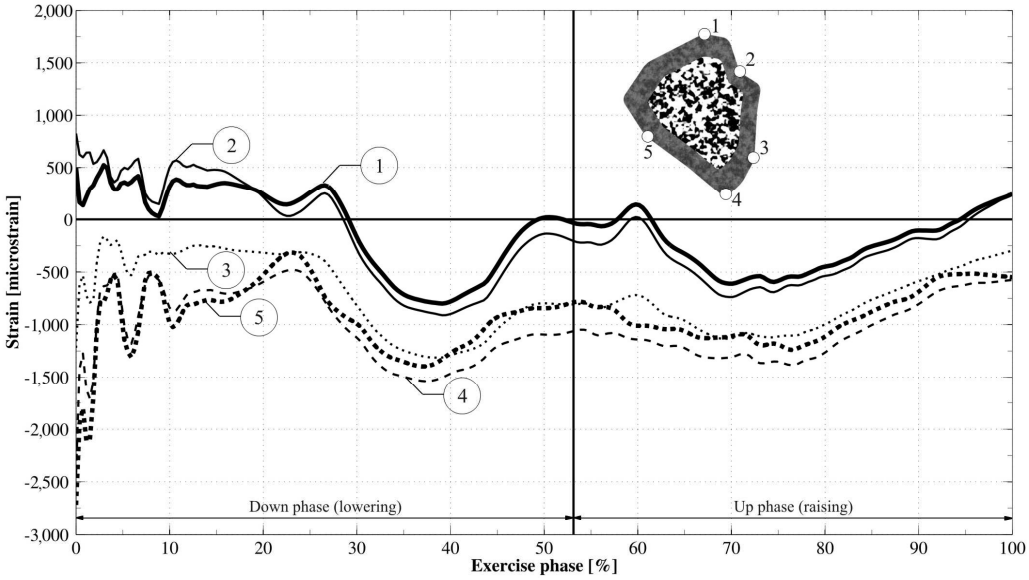

Figure 52. Axial strain values at the midshaft of the left tibia during squat performed at low speed

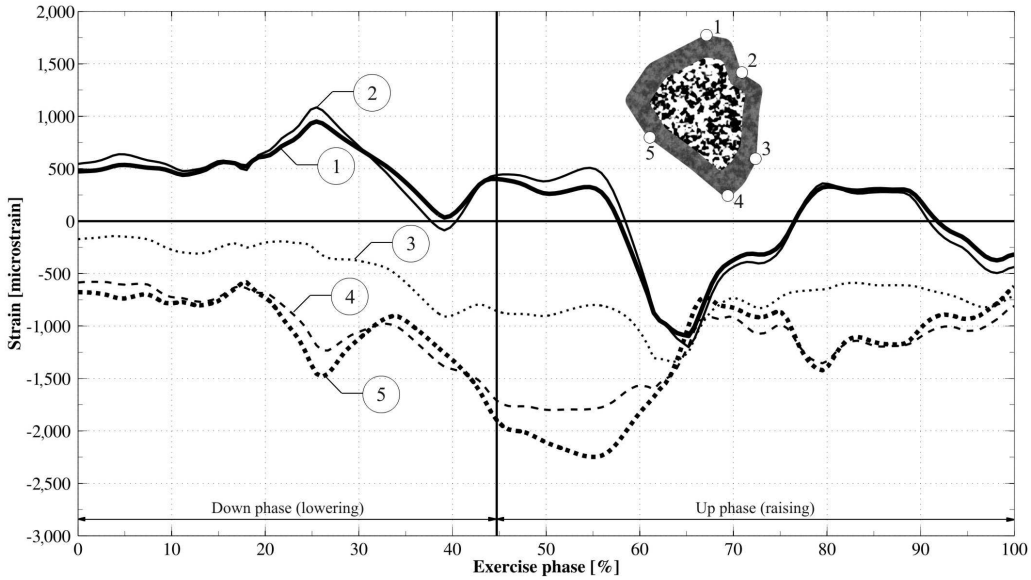

Figure 53. Axial strain values at the midshaft of the left tibia during squat performed at high speed

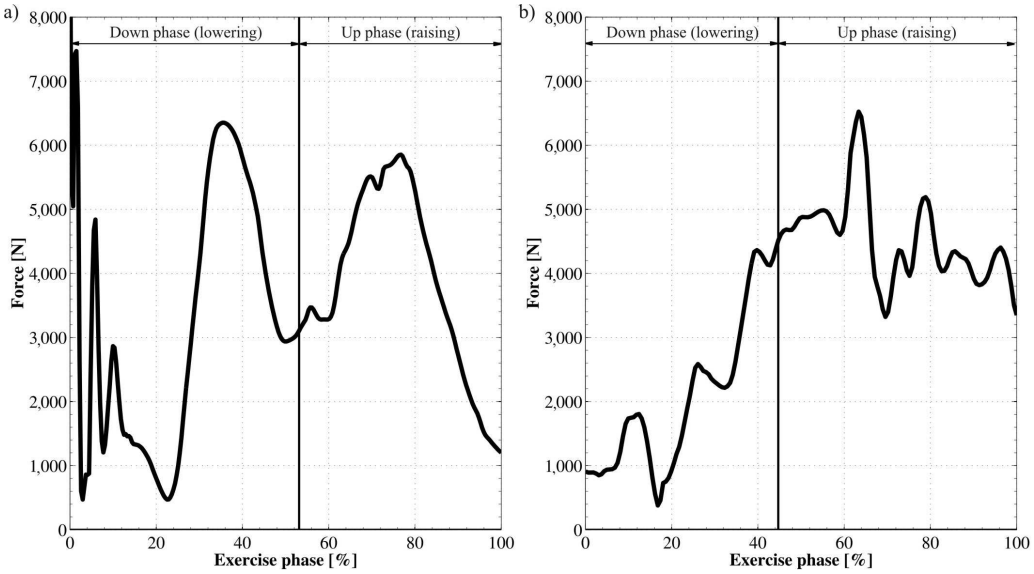

Figure 54. Left knee forces during squat performed at a) low and b) high speed

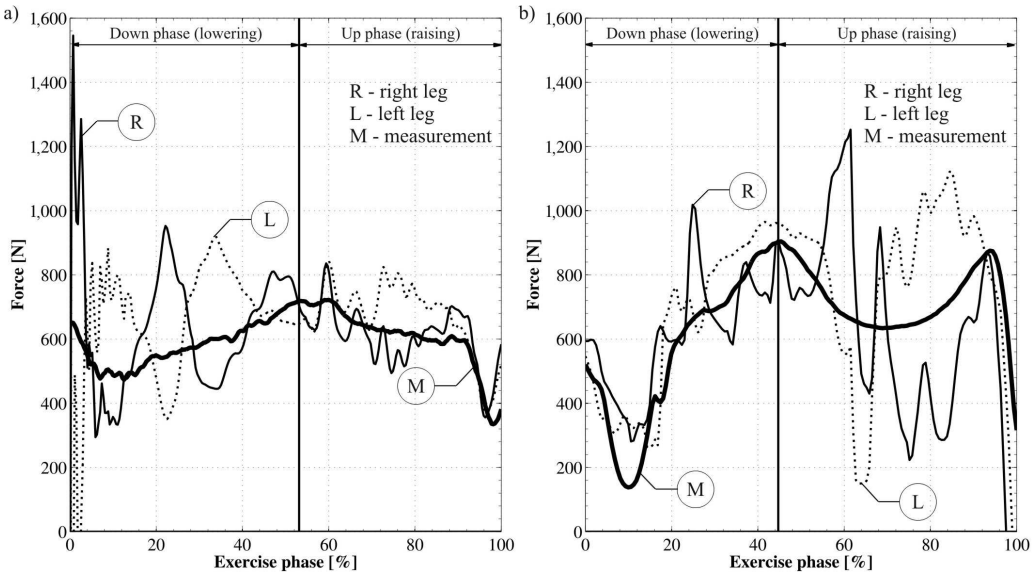

Figure 55. Ground reaction force during the squat exercise at a) low and b) high speed

4.5.3 Discussion

Correlation between ground reaction forces computed for left and right leg during both trials was 97.9 %. The correlation between computed values with respect to measured ones was obtained to be 83.6 % and 92.9 % for the right and left leg respectively. This indicates that flexibility of the left tibia improves the computation accuracy. Quantifying the speed of movement in case of the squat exercise is cumbersome, thus the timing of the exercise phases are used.

For the squat exercise the speed differences were significant (Figure 51). The speed difference between down phases is nearly double, the second down phase is performed almost 43 % faster than the first one. The speed differences clearly affect the ground reaction forces (Figure 55), especially during the up phase. Ground reaction forces estimated in the simulations closely follow the measured value that allows concluding the simulation correctness. Performing this exercise slowly results in increased knee forces during the down phase (Figure 54). Faster descent allows performing the exercise with little braking forces, which increase gradually until the turning point. Then several spikes of force are produced before the skeleton is accelerated upwards. From the knee loading point of view the most beneficial configuration would be with fast

descent and slow up phase. This configuration would result in the minimal knee forces.

Considering strain values, fast lowering results in bending domination. Slowing down the descent, results in the change of the dominating load to compression. This is the result of the muscle antagonistic effect, which allows reducing tensile strain values on the bended bone. Rising phase is characterized by combination of bending and compression in both cases. Fast raising however, results in higher absolute strain values what is plausible for bone formation. Bending axis location is preserved in the same orientation in both test cases.

Comparing knee forces and ground reaction forces charts, it can be concluded that in this particular exercise ground reaction force is not a good predictor of knee forces. It can only indicate load balance between legs, which can be used to determine the stronger leg, as it will carry higher load.

5 Conclusions and summary

Thesis presents results and methodologies of simulation of dynamic bone strain values during four typical gym exercises. In addition, simulations of walking are presented for reference. The strain results show that, similarly to walking, knee flexion is a low strain exercise. Despite the similarity to knee flexion, knee extension can be an optimal exercise for tibia strengthening according to the mechanostat theory (Frost, 1987). Moderate amount of strain is induced to tibia during squat. High strain values occurred during leg press. Despite that each of the exercises were performed at different loading condition, in all the cases the loading was chosen to be close to the maximum load that the subject could accommodate. Knee flexion, extension and leg press represent stationary exercises, where only leg muscles of one leg were considerably utilized. Squat and walking on the other hand, represent fully three-dimensional activities involving also balance.

The strain results observed during the studied gym exercises are comparable to values obtained *in-vivo* for running. Axial strains on mid-diaphysis of the tibia during over-ground running were measured within the *in-vivo* range between -2,456 to 1,243 με, depending on the subject (Milgrom et al., 2003). The same study gives values for treadmill running that range from -956 to 959 με. In the current research, at the same tibial-site, strain values oscillate between -1,813 to -579 με for high-speed squatting, and between -2,457 to -477 με for low-speed squatting. Squatting results in similar bone strain levels as over-ground running. Knee extension with a 40 kg load resulted in tibial strains on the anterior site of the mid-diaphysis in the range of -4,010 to 317 με, and -3,549 to 296 με for high-speed and moderate-speed exercise, respectively. This is significantly higher bone loading than for over-ground running. On the other hand, the same exercise performed slowly resulted in tibial strain values (-2,876 to -37 με) that were comparable to those of the over-ground running. Reducing the load from 40 to 30 kg did not appreciably reduce strain values. The leg press was characterized by high mid-diaphysis tibial strains at any speeds, reaching up to -4,013 με in compression and 362 με in tension. Finally, knee flexion showed results comparable to treadmill running. The strains were within -142 to 787 με.

Simulation procedure for each of the exercises were similar, they started with laboratory experiment, involving motion capture, force measurement and electromyography monitoring. The motion capture was used for driving the model in inverse dynamics; force measurements were used as an input to the model of externally applied forces, and electromyography was used on some occasions for individual muscle control to reduce muscle redundancy. Second phase was inverse dynamics aiming at validation of the motion capture as well as obtaining muscle shortening patterns. Finally forward dynamics analysis was performed, which allowed for strain estimation in the tibia or femur (in walking). This methodology has been proved to function correctly and reliably for the presented set of exercises. Verification of the customized simulation method for each exercise was performed separately, proving results to be sound. Finally correlation of the results obtained from the models with the previously published results was established and comparison of the results between exercises was made.

Collecting the information presented in previous two chapters, and applying bone formation theories to the obtained data, conclusions can be drawn regarding the osteogenicity of the presented exercises. Strain loading in walking is used here as the reference. According to the mechanostat theory (Frost, 1987), physiological bone strain limits are roughly 50–3,000 με. Where the lower limit can vary between 50 and 200 με and the upper boundary is set between 2,000 and 3,000 με. Physiological, in this case, means the loading condition that do not influence bone formation or resorption. According to the theory, bones subjected to loading resulting in strain values below 200 με will be subjected to the resorption process. That should be fast progressing with the decrease of the loading. On the other extreme, the theory defines strain values from the upper bound of physiological limits up to 4,000 με as the overload state. Already at this stage the bone formation process is initiated and progresses toward the last limit, referred as pathological. Mechanostat theory is backed up by experimental data, for instance (Kohrt et al., 2004) also shows that strength training has an osteogenic potential.

Considering the mechanostat theory, walking represents lower physiological loading scenario for tibia, however, femoral neck loading during walking already falls to the middle range of physiological loading. This indicates that

the strain that occur during the same exercise is different at different bone sites. Even thou the bones that are caring more load are larger in size, the size do not compensate the deformation due to the loading, what can be observed in femoral neck. Surprisingly femoral neck, which carries significant bending loads almost all the time, due to its orientation with respect to the human body, has the smallest cross section within the femur. This biological under-design, makes it the most vulnerable part of the femur.

Following the theory (Frost, 1987), leg press exercise with 90 kg of load can have positive effect on tibia strengthening. The peak strain values enforced by this exercise are within the limit of 2,000–3,000 με in tension and can reach to 4,000 με in compression. This indicates that this particular loading was relatively high for the test subject, reaching occasionally overload state defined by Frost (Frost, 1987). From mechanical point of view squatting is similar to leg press. This exercise however, requires additional effort due to balancing of the body and supporting the whole body weight in comparison to leg press. The test subject performed the squat with 70 kg of external load. This resulted in tibial strain values at the level of 1,000 με in tension, and up to 2,200 με in compression. The results indicate that in case of the specific loading and subject that was used in the current study, squatting does not represent efficient way of strengthening tibias. However, it is expected to cause strengthening of femurs, thou this has to be still verified.

Knee flexion performed with 25 kg of load was a light exercise for the subject in terms of tibial strengthening. The strain values did not exceed 1,000 με in tension and not even 900 με in compression. Because the subject could not perform the exercise with higher load, it is concluded that knee flexion is having weak osteogenic potential for tibia. Despite the similarity in mechanics of the knee extension exercise to knee flexion, stronger muscles are used to actuate the lower leg in the knee extension exercise. For that reason subject was able to perform the exercise with 30 and 40 kg of load. Exercise performed with 30 kg of load at low speed resulted in strain values that can be classified as the middle limit of physiological loading. The same exercise performed at high or moderate speed already caused increase of the strain values to the upper limit of physiological loading according to the theory (Frost, 1987). This loading-speed combination for the knee extension was an optimal case for the test subject.

Knee extension performed at low speed with 40 kg of loading already induces strain at tibia at the level of 2,000–3,000 με, indicating another optimal load-speed configuration for the subject. However, increasing the speed leads to the overloading case according to the mechanostat theory (Frost, 1987).

Taking into account safety, the optimal exercise limit could be the one causing strain at the border between physiological and overload case of mechanostat theory. This type of loading should allow maintaining bone mass or even slight increase of it, at the same time giving relatively large safety margin for fracture. Rapid bone mass increase could be observed at mild overload, which means enforcing strain on the level of 3,500 με (Frost, 1987). Exceeding the limit of 4,000 με will most probably considerably increase the risk of bone fracture, thus this region should be avoided. For instance, it is known that tibial stress fractures are common in case of infantry recruits, due to the overtraining (Milgrom et al., 1985).

5.1 Future developments

The computations of the models were conducted in MSC ADAMS commercial package. The efficiency of the computations was relatively good and forward dynamics simulations were performed around 60-times slower than the real time. Application of the method to estimate bone strain online would require customized code, however, it would create a great opportunity to aid physical training optimized on strengthening bones. Before application of this technique in commercial products, more comparative studies of experimental and simulation convergence is needed.

Strain values and muscle forces can be affected by the type of joint description used in the model. Thus it would be highly interesting to investigate the influence of contact joint description on the strain and muscle force results. Muscle models can be also improved in the future by utilizing neuromuscular muscle representation. Finally with the development of electromyography measurement devices, in the future it might be possible to control muscles reliably using EMG-force relationships established for the test subjects.

Bibliography

Aamodt, A., Lund-Larsen, J., Eine, J., Andersen, E., Benum, P., and Husby, O. S. "In Vivo Measurements Show Tensile Axial Strain in the Proximal Lateral Aspect of the Human Femur." *Journal of Orthopaedic Research* 15, no. 6 (1997): 927-931.

Agrawal, O. P., and Shabana, A. A. "Dynamic Analysis of Multibody Systems Using Component Modes." *Computers & Structures* 21, no. 6 (1985): 1303-1312.

Al Nazer, R., Klodowski, A., Rantalainen, T., Heinonen, A., Sievänen, H., and Mikkola, A. "Analysis of Dynamic Strains in Tibia During Human Locomotion Based on Flexible Multibody Approach Integrated with Magnetic Resonance Imaging Technique." *Multibody System Dynamics* 20, no. 4 (2008b): 287-306.

Al Nazer, R., Klodowski, A., Rantalainen, T., Heinonen, A., Sievanen, H., and Mikkola, A. "A Full Body Musculoskeletal Model Based on Flexible Multibody Simulation Approach Utilised in Bone Strain Analysis During Human Locomotion." *Computer Methods in Biomechanics and Biomedical Engineering* 14, no. 6 (2011): 573-579.

Al Nazer, R., Rantalainen, T., Heinonen, A., Sievänen, H., and Mikkola, A. "Flexible Multibody Simulation Approach in the Analysis of Tibial Strain During Walking." *Journal of Biomechanics* 41, no. 5 (2008a): 1036-1043.

Anderson, F. C., and Pandy, M. G. "Dynamic Optimization of Human Walking." *Journal of Biomechanical Engineering* 123, no. 5 (2001): 381-390.

Ashman, R. B., and Rho, J. Y. "Elastic Modulus of Trabecular Bone Material." *Journal of Biomechanics* 21, no. 3 (1988): 177-181.

Ashman, R. B., Cowin, S. C., van Buskirk, W. C., and Rice, J. C. "A Continuous Wave Technique for the Measurement of the Elastic Properties of Cortical Bone." *Journal of Biomechanics* 17, no. 5 (1984): 349-361.

Bankman, I. N. *Handbook of Medical Imaging.* Elsevier Inc (2000).

Bechard, L. J., Wroe, E., and Ellis, K. "Body Composition and Growth." In *Nutrition in Pediatrics: Basic Science, Clinical Applications* by Duggan, C., Watkins, J. B., and Walker, W. A. Hamilton: BC Decker Inc (2008): 27-39.

Beck, T. J., Rudd, C. B., Shaffer, R. A., Betsinger, K., Trone, D. W., and Brodine, S. K. "Stress Fracture in Military Recruits: Gender Differences in Muscle and Bone Susceptibility Factors." *Bone* 27, no. 3 (2000): 437-444.

Bediz, B., Ozgüven, H. N., and Korkusuz, F. "Vibration Measurements Predict the Mechanical Properties of Human Tibia." *Clinical Biomechanics* 25, no. 4 (2010): 365-371.

Biewener, A. A. "Musculoskeletal Design in Relation to Body Size." *Journal of Biomechanics* 24, suppl 1 (1991): 19-29.

Burr, D. B., Milgrom, C., Fyhrie, D., Forwood, M., Nyska, M., Finestone, A., Hoshaw, S., Saiag, E., and Simkin, A. "In Vivo Measurement of Human Tibial Strains During Vigorous Activity." *Bone* 18, no. 5 (1996): 405-410.

Bushong, S. C. *Magnetic Resonance Imaging.* St. Louis: C.V. Mosby Co. (1988).

Buzug, T. M. *Computed Tomography.* Luebeck: Springer (2008).

Carter, D. R., Caler, W. E., Spengler, D. M., and Frankel, V. H. "Fatigue Behavior of Adult Cortical Bone: The Influence of Mean Strain and Strain Range." *Acta Orthopedica Scandinavica* 52, no. 5 (1981): 481-491.

Carter, D. R., and Hayes, W. C. "The Compressive Behavior of Bone as a Two-Phase Porous Structure". *The Journal of Bone and Joint Surgery. American Volume* 59, no. 7 (1977): 954-962.

Choi, K., Kuhn, J. L., Ciarelli, M. J., and Goldstein, S. A. "The Elastic Moduli of Human Subchondral, Trabecular, and Cortical Bone Tissue and the Size-Dependency of Cortical Bone Modulus." *Journal of Biomechanics* 23, no. 11 (1990): 1103-1113.

Craig, R. R., and Bampton, M. C. C. "Coupling of Substructures for Dynamic Analysis." *AIAA Journal* 6, no. 7 (1968): 1313-1319.

Dalstra, M., Huiskes, R., Odgaard, A., and van Erning, L. "Mechanical and Textural Properties of Pelvic Trabecular Bone." *Journal of Biomechanics* 26, no. 4-5 (1993): 523-535.

Dong, X. N., and Guo, X. E. "The Dependence of Transversely Isotropic Elasticity of Human Femoral Cortical Bone on Porosity." *Journal of Biomechanics* 37, no. 8 (2004): 1281-1287.

Frost, H. M. "Bone “Mass” and the “Mechanostat”: A Proposal." *The Anatomical Record* 219, no. 1 (1987): 1-9.

Funk, R. J., Rudd, R. W., Kerrigan, J. R., and Crandall, J. R. "The Line of Action in the Tibia During Axial Compression of the Leg." *Journal of Biomechanics* 40, no. 10 (2007): 2277-2282.

Garcia, G. J. M., and da Silva, J. K. L. "On the Scaling of Mammalian Long Bones." *Journal of Experimental Biology* 207 (2004): 1577-1584.

Geradin, M., and Cardona, A. *Flexible Multibody Dynamics, A Finite Element Approach.* Chichester: John Wiley & Sons, LTD (2000).

Goh, J. C., Mech, A. M., Lee, E. H., Ang, E. J., Bayon, P., and Pho, R. W. "Biomechanical Study on the Load-Bearing Characteristics of the Fibula and the Effects of Fibular Resection." *Clinical Orthopaedics and Related Research* 279 (1992): 223-228.

Hadjidakis, D. J., and Androulakis, I. I. "Bone Remodeling." *Annals of the New York Academy of Sciences* 1092 (2006): 385-396.

Hatze, H. "Estimation of Myodynamics Parameter Values from Observations on Isometrically Contracting Muscle Groups." *European Journal of Applied Physiology and Occupational Physiology* 46, no. 4 (1981): 325-338.

Heinonen, A., Kannus, P., Sievänen, H., Oja, P., Pasanen, M., Rinne, M., Uusi-Rasi, K., and Vuori, I. "Randomised Controlled Trial of Effect of High-Impact Exercise on Selected Risk Factors for Osteoporotic Fractures." *Lancet* 348, no. 9038 (1996): 1343-1347.

Heinonen, A., Mckaya, H. A., Whittall, K. P., Forster, B. B., and Khan, K. M. "Muscle Cross-Sectional Area is Associated with Specific Site of Bone in Prepubertal Girls: A Quantitative Magnetic Resonance Imaging Study." *Bone* 29, no. 4 (2001): 388-392.

Helgason, B., Perilli, E., Schileo, E., Taddei, F., Brynjólfsson, S., and Viceconti, M. "Mathematical Relationships Between Bone Density and Mechanical Properties: A Literature Review." *Clinical Biomechanics* 23, no. 2 (2008): 135-146.

Hill, A. V. "The Heat of Shortening and the Dynamic Constants of Muscle." *Proceedings of the Royal Society of London* 126, no. 843 (1938): 136-195.

Hodgskinson, R., Currey, J. D., and Evans, G. P. "Hardness, an Indicator of the Mechanical Competence of Cancellous Bone." *Journal of Orthopaedic Research* 7, no. 5 (1989): 754-758.

Hoshaw, S. J., Fyhrie, D. P., Takano, Y., Burr, D. B., and Milgrom, C. "A Method Suitable for in Vivo Measurement of Bone Strain in Humans." *Journal of Biomechanics* 30, no. 5 (1997): 521-524.

Ishikawa, M., Niemelä, E., and Komi, P. V. "Interaction Between Fascicle and Tendinous Tissues in Short-Contact Stretch-Shortening Cycle Exercise with Varying Eccentric Intensities." *Journal of Applied Physiology* 99, no. 1 (2005): 217-223.

Jämsä, T., Vainionpää, A., Korpelainen, R., Vihriälä, E., and Leppäluoto, J. "Effect of Daily Physical Activity on Proximal Femur." *Clinical Biomechanics* 21, no. 1 (2006): 1-7.

Järvinen, T. L., Kannus, P., Sievänen, H., Jolma, P., Heinonen, A., and Järvinen, M. "Randomized Controlled Study of Effects of Sudden Impact Loading on Rat Femur." *Journal of Bone and Mineral Research* 13, no. 9 (1998): 1475-1482.

Kannus, P., Niemi, S., Parkkari, J., Palvanen, M., Heinonen, A., Sievänen, H., Järvinen, T., Khan, K., and Järvinen, M. "Why is the Age-Standardized

Incidence of Low-Trauma Fractures Rising in Many Elderly Populations?" *Journal of Bone and Mineral Research* 17, no. 8 (2002): 1363-1367.

Kannus, P., Niemi, S., Parkkari, J., Palvanen, M., Vuori, I., and Järvinen, I. M. "Hip Fractures in Finland Between 1970 and 1997 and Predictions for the Future." *Lancet* 353, no. 9155 (1999): 802-805.

Keller, T. S. "Predicting the Compressive Mechanical Behavior of Bone." *Journal of Biomechanics* 27, no. 9 (1994): 1159-1168.

Keyak, J. H., Rossi, S. A., Jones, K. A., and Skinner, H. B. "Prediction of Femoral Fracture Load Using Automated Finite Element Modeling." *Journal of Biomechanics* 31, no. 2 (1997): 125-133.

Kim, S. S., and. Haug, E. J. "Selection of Deformation Modes for Flexible Multibody Dynamics." *Mechanics of Structures and Machines* 18, no. 4 (1990): 565-586.

Kopperdahl, D. L., and Keaveny, T. M. "Yield Strain Behavior of Trabecular Bone." *Journal of Biomechanics* 31, no. 7 (1998): 601-608.

Klodowski, A., Rantalainen, T., Mikkola, A., Dastidar, P., Heinonen, A., and Sievänen, H. "A Dynamic Simulation of a Human Gait Using the Hybrid Muscle Model and a qCT-Based Flexible Tibia." *Proceedings of the ASME 2009 International Design Engineering Technical Conferences & Computers and Information in Engineering Conference.* San Diego (2009).

Kłodowski, A., Rantalainen, T., Heinonen, A., Sievänen, H., and Mikkola, A. "An Application of the Flexible Multibody Approach Used to Estimate Human Skeleton Loading." *Rakenteiden Mekaniikka (Journal of Structural Mechanics)* 44, no. 2 (2011a): 128-139.

Kłodowski, A., Rantalainen, T., Mikkola, A., Heinonen, A., and Sievänen, H. "Flexible Multibody Approach in Forward Dynamic Simulation of Locomotive Strains in Human Skeleton with Flexible Lower Body Bones." *Multibody System Dynamics* 25, no. 4 (2011b): 395-409.

Kłodowski, A., Valkeapää, A., and Mikkola, A. "Craig-Bampton Modal Reduction Applied to Human Tibia Tradeoff Between Accuracy and Speed."

Proceedings of the ASME 2011 International Mechanical Engineering Congress & Exposition. Denver (2011c).

Kłodowski, A., Valkeapää, A., and Mikkola, A. "Pilot Study on Proximal Femur Strains During Locomotion and Fall-Down Scenario." *Multibody System Dynamics* 28, no. 3 (2012): 239-256.

Kohrt, W. M., Bloomfield, S. A., Little, K. D., Nelson, M. E., and Yingling, V. R. "Physical Activity and Bone Health." *Medicine and Science in Sport and Exercise* 36, no. 11 (2004): 1985-1996.

Komi, P. V., Fukashiro, S., and Järvinen, M. "Biomechanical Loading of Achilles Tendon During Normal Locomotion." *Clinics in Sports Medicine* 11, no. 3 (1992): 521-531.

Kuhn, J. L., Goldstein, S. A., Choi, R., London, M., Feldkamp, L. A., and Matthews, L. S. "Comparison of the Trabecular and Cortical Tissue Moduli from Human Iliac Crests." *Journal of Orthopaedic Research* 7, no. 6 (1989): 876-884.

Kuipers, J. B. *Quaternions and Rotation Sequences.* New Jersey: Princeton University Press (2002).

Langsetmo, L., Morin, S., Kovacs, C. S., Kreiger, N., Josse, R., Adachi, J. D., Papaioannou, A., Goltzman, D., Hanley, D. A., Olszynski, W. P., Prior, J., Jamal, S. A. and CaMos Research Group "Determining Whether Women with Osteopenic Bone Mineral Density Have Low, Moderate, or High Clinical Fracture Risk." *Menopause* 17, no. 5 (2010): 1010-1016.

Lanyon, L. E. "Functional Strain in Bone Tissue as an Objective, and Controlling Stimulus for Adaptive Bone Remodelling." *Journal of Biomechanics* 20, no. 11-12 (1987): 1083-1093.

Lanyon, L. E., and Rubin, C. T. "Static vs Dynamic Loads as an Influence on Bone Remodelling." *Journal of Biomechanics* 17, no. 12 (1984): 897-905.

Lanyon, L. E., Hampson, W. G. J., Goodship, A. E., and Shah, J. S. "Bone Deformation Recorded in Vivo from Strain Gauges Attached to the Human Tibial Shaft." *Acta Orthopedica Scandinavica* 46, no. 2 (1975): 256-268.

Linde, F., Hvid, I., and Madsen, F. "The Effect of Specimen Geometry on the Mechanical Behaviour of Trabecular Bone Specimens." *Journal of Biomechanics* 25, no. 4 (1992): 359-368.

Liskova, M., and Hert, J. "Reaction of Bone to Mechanical Stimuli." *Folia Morphologica* 19, no. 3 (1971): 301-317.

Lotz, J. C., Gerhart, T. N., and Hayes, W. C. "Mechanical Properties of Trabecular Bone from the Proximal Femur: A Quantitative CT Study." *Journal of Computer Asisted Tomography* 14, no. 1 (1990): 107-114.

Macdonald, H. M., Cooper, D. M. L., and McKay, H. A. "Anterior-Posterior Bending Strength at the Tibial Shaft Increases with Physical Activity in Boys: Evidence for Non-Uniform Geometric Adaptation." *Osteoporosis International* 20, no. 1 (2008): 61-70.

Menegaldo, L. L., Fleury, A. T., and Weber, H. I. "Biomechanical Modeling and Optimal Control of Human Posture." *Journal of Biomechanics* 36, no. 11 (2003): 1701-1712.

Mente, P. L., and Lewis, L. J. "Experimental Method for the Measurement of the Elastic Modulus of Trabecular Bone Tissue." *Journal of Orthopaedic Research* 7, no. 3 (1989): 456-461.

Milgrom, C., Finestone, A., Benjoyan, N., Simkin, A., Ekenman, I., and Burr, D. B. "Measurement of Strain and Strain Rate Developed by Jumping Exercises in Vivo in Humans." *Southern Biomedical Engineering Conference - Proceedings.* IEEE (1998): 108.

Milgrom, C., Finestone, A., Segev, S., Olin, C., Arndt, T., and Ekenman, I. "Are Overground or Treadmill Runners More Likely to Sustain Tibial Stress Fracture?" *British Journal for Sports Medicine* 37 (2003): 160-163.

Milgrom, C., Giladi, M., Stein, M., Kashtan, H., Margulies, J. Y., Chisin, R., Steinberg, R., and Aharonson, Z. "Stress Fractures in Military Recruits. A Prospective Study Showing an Unusually High Incidence." *Journal of Bone and Joint Surgery* 67-B, no. 5 (1985): 732-735.

Milgrom, C., Radeva-Petrova, D. R., Finestone, A., Nyska, M., Mendelson, S., Benjuya, N., Simkin, A., and Burr, D. "The Effect of Muscle Fatigue on in Vivo Tibial Strains." *Journal of Biomechanics* 40, no. 4 (2007): 845-850.

Morgan, E. F., Bayraktar, H. H., and Keaveny, T. M. "Trabecular Bone Modulus-Density Relationships Depend on Anatomic Site." *Journal of Biomechanics* 36, no. 7 (2003): 897-904.

Nikander, R., Kannus, P., Dastidar, P., Hannula, M., Harrison, L., Cervinka, T., Narra, N. G., Aktour, R., Arola, T., Eskola, H., Soimakallio, S., Heinonen, A., Hyttinen, J., and Sievänen, H. "Targeted Exercises Against Hip Fragility." *Osteoporosis International* 20, no. 8 (2009a): 1321-1328.

Nikander, R., Kannus, P., Rantalainen, T., Uusi-Rasi, K., Heinonen, A., and Sievänen, H. "Cross-Sectional Geometry of Weight-Bearing Tibia in Female Athletes Subjected to Different Exercise Loadings." *Osteoporosis International* 21, no. 10 (2009b): 1687-1694.

Nikander, R., Sievänen, H., Heinonen, A., Karstila, T., and Kannus, P. "Load-Specific Differences in the Structure of Femoral Neck and Tibia Between World-Class Moguls Skiers and Slalom Skiers." *Scandinavian Journal of Medicine & Science in Sports* 18, no. 2 (2008): 145-153.

Perttunen, J. O., Kyröläinen, H., Komi, P. V., and Heinonen, A. "Biomechanical Loading in the Triple Jump." *Journal of Sports Sciences* 18, no. 5 (2000): 363-370.

Peterman, M. M., Hamel, A. J., Cavanagh, P. R., Piazza, J., and Sharkey, N. A. "In Vitro Modeling of Human Tibial Strains During Exercise in Micro-Gravity." *Journal of Biomechanics* 34, no. 5 (2001): 693-698.

Rantalainen, T., and Kłodowski, A. "Estimating Lower Limb Skeletal Loading." In *Theoretical Biomechanics* by Vaclav Klika. Rijeka: InTech (2011): 243-266.

Rantalainen, T., Kłodowski, A., and Piitulainen, H. "Effect of Innervation Zones in Estimating Biceps Brachii Force-EMG Relationship During Isometric

Contraction." *Journal of Electromyography and Kinesiology* 22, no. 1 (2011): 80-87.

Rantalainen, T., Nikander, R., Heinonen, A., Suominen, H., and Sievänen, H. "Direction-Specific Diaphyseal Geometry and Mineral Mass Distribution of Tibia and Fibula: A pQCT Study of Female Athletes Representing Different Exercise Loading Types." *Calcified Tissue International* 86, no. 6 (2010): 447-454.

Reilly, D. T., and Burstein, H. H. "The Elastic and Ultimate Properties of Compact Bone Tissue." *Journal of Biomechanics* 8, no. 6 (1975): 393-405.

Rho, J. Y., Ashman, R. B., and Turner, C. H. "Young's Modulus of Trabecular and Cortical Bone Material: Ultrasonic and Microtensile Measurements." *Journal of Biomechanics* 26, no. 2 (1993): 111-119.

Rho, J. Y., Hobatho, M. C., and Ashman, R. B. "Relations of Mechanical Properties to Density and CT Numbers in Human Bone." *Medical Engineering & Physics* 17, no. 5 (1995): 347-355.

Rho, J. Y., Roy, M., Tsui, T. Y., and Pharr, G. M. "Young's Modulus and Hardness of Trabecular and Cortical Bone in Various Directions Determined by Nanoindentation." In *Transactions of the 43rd Annual Meeting of the Orthopaedic Research Society.* San Francisco (1997): 891.

Riggs, B. L., and Melton, L. J. *Osteoporosis. Etiology, Diagnosis and Treatment*. 2nd Ed. Hagerstown, MD: Lippincott-Raven Publishers (1995).

Rubin, C. T., and Lanyon, L. E. "Regulation of Bone Formation by Applied Dynamic Loads." *Journal of Bone and Joint Surgery. American Volume* 66, no. 3 (1984): 397-402.

Runkle, J. C., and Pugh, J. "The Micro-Mechanics of Cancellous Bone. II. Determination of the Elastic Modulus of Individual Trabeculae by a Buckling Analysis." *Bulletin of the Hospital for Joint Diseases* 36, no. 1 (1975): 2-10.

Ryan, S. D., and Williams, J. L. "Tensile Testing of Rodlike Trabecluae Excised from Bovine Femoral Bone." *Journal of Biomechanics* 22, no. 4 (1989): 351-355.

Schaffler, M. B., Radin, E. L., and Burr, D. B. "Long-Term Fatigue Behavior of Compact Bone at Low Strain Magnitude and Rate." *Bone* 11, no. 5 (1990): 321-326.

Shabana, A. A. *Dynamics of Multibody Systems.* Third Edition. New York: Cambridge University Press (2005).

Shedd, K. M., Hanson, K. B., Alekel, D. L., Schiferl, D. J., Hanson, L. N., and van Loan, M. D. "Quantifying Leisure Physical Activity and Its Relation to Bone Density and Strength." *Medicine and Science in Sports and Exercise* 39, no. 12 (2007): 2189-2198.

Silder, A., Heiderscheit, B., and Thelen, D. G. "Active and Passive Contributions to Joint Kinetics During Walking in Older Adults." *Journal of Biomechanics* 41, no. 7 (2008): 1520-1527.

Simon, D. A., and Lavallée, S. "Medical Imaging and Registration in Computer Assisted Surgery." *Clinical Orthopaedic and Related Research* September, no. 354 (1998): 17-27.

Slaughter, W. S. *The Linearised Theory of Elasticity*. Boston: Birkhauser (2002).

Smith, E. L., and Gilligan, C. "Mechanical Forces and Bone." *Journal of Bone and Mineral Research* 6 (1989): 139-173.

Snyder, S. M., and Schneider, E. "Estimation of Mechanical Properties of Cortical Bone by Computed Tomography." *Journal of Orhopaedic Research* 9, no. 3 (1991): 422-431.

Sverdlova, N. S., and Witzel, U. "Principles of Determination and Verification of Muscle Forces in the Human Musculoskeletal System: Muscle Forces to Minimise Bending Stress." *Journal of Biomechanics* 43, no. 3 (2010): 387-396.

Townsend, P. R., Rose, R. M., and Radin, E. L. "Buckling Studies of Single Human Trabeculae." *Journal of Biomechanics* 8, no. 3-4 (1975): 199-201.

Turner, C. H. "Three Rules for Bone Adaptation to Mechanical Stimuli." *Bone* 23, no. 5 (1998): 399-407.

Turner, C. H., and Robling, A. G. "Designing Exercise Regimens to Increase Bone Strength." *Exercise and Sport Sciences Reviews* 31, no. 11 (2003): 45-50.

Turner, C. H., Takano, Y., and Owan, I. "Aging Changes Mechanical Loading Tresholds for Bone Formation in Rats." *Journal of Bone and Mineral Research* 10 (1995): 1544-1549.

Umemura, Y., Sogo, N., and Honda, A. "Effects of Intervals Between Jumps or Bouts on Osteogenic Response to Loading." *Journal of Applied Physiology* 93, no. 4 (2002): 1345-1348.

Vainionpää, A., Korpelainen, R., Leppäluoto, J., and Jämsä, T. "Effects of High-Impact Exercise on Bone Mineral Density: A Randomized Controlled Trial in Premenopausal Women." *Osteoporosis International* 16, no. 2 (2005): 191-197.

Vainionpää, A., Korpelainen, R., Sievänen, H., Vihriälä, E., Leppäluoto, J., and Jämsä, T. "Effect of Impact Exercise and Its Intensity on Bone Geometry at Weight-Bearing Tibia and Femur." *Bone* 40, no. 3 (2007): 604-611.

Vainionpää, A., Korpelainen, R., Vihriälä, E., Rinta-Paavola, A., Leppäluoto, J., and Jämsä, T. "Intensity of Exercise is Associated with Bone Density Change in Premenopausal Women." *Osteoporosis International* 17, no. 3 (2006): 455-463.

van Rietbergen, B., Weinans, H., Huiskes, R., and Odgaard, A. "A New Method to Determine Trabecular Bone Elastic Properties and Loading Using Micromechanical Finite-Element Models." *Journal of Biomechanics* 28, no. 1 (1995): 69-81.

Verghese, J., Lipton, R. B., Hall, C. B., Kuslansky, G., Katz, M. J., and Buschke, H. "Abnormality of Gait as a Predictor of Non-Alzheimer's Dementia." *The New England Journal of Medicine* 347, no. 22 (2002): 1761-1768.

von Stengel, S., Kemmler, W., Kalender, W. A., Engelke, K., and Lauber, D. "Differential Effects of Strength Versus Power Training on Bone Mineral

Density in Postmenopausal Women: A 2-Year Longitudinal Study." *British Journal of Sports Medicine* 41, no. 10 (2007): 649-655.

von Stengel, S., Kemmler, W., Pintag, R., Beeskow, C., Weineck, J., Lauber, D., Kalender, W. A., and Engelke, K. "Power Training is More Effective Than Strength Training for Maintaining Bone Mineral Density in Postmenopausal Women." *Journal of Applied Physiology* 99, no. 1 (2005): 181-188.

Whalen, R. T., Carter, D. R., and Steele, C. R. "Influence of Physical Activity on the Regulation of Bone Density." *Journal of Biomechanics* 21, no. 10 (1988): 825-837.

WHO. *Recomentation for Preventing Osteoporosis* (1994): http://www.who.int.

Wilks, D. C., Winwood, K., Gilliver, S. F., Kwiet, A., Chatfield, M., Michaelis, I., Sun, L. W., Ferretti, J. L., Sargeant, A. J., Felsenberg, D., and Rittweger, J. "Bone Mass and Geometry of the Tibia and the Radius of Master Sprinters, Middle and Long Distance Runners, Race-Walkers and Sedentary Control Participants: A pQCT Study." *Bone* 45, no. 1 (2009): 91-97.

Williams, J. L., and Lewis, J. L. "Properties and Anisotropic Model of Cancellous Bone from the Proximal Tibial Epiphysis." *Journal of Biomechanical Engineering* 104, no. 1 (1982): 50-56.

Winters, J. M. "How Detailed Should Muscle Models Be to Understand Multi-Joint Movement Coordination?" *Human Movement Science* 14, no. 4 (1995): 401-442.

Wolff, J. "Das Gesetz der Transformation der Knochen." *A. Hirschwald* (1892). English translation by Maquet, P., and Furlong, R. Berlin: Springer-Verlag (1986).

Wu, H. T., Mani, N. K., and Ashrafiuon, H. "Selection of Modal Basis for Flexible Bodies of Mechanical Systems." *Mechanism and Machine Theory* 30, no. 3 (1995): 471-489.

Yoshikawa, T., Mori, S., Santiesteban, A. J., Sun, T. C., Hafstad, E., Chen, J., and Burr, D. B. "The Effects of Muscle Fatigue on Bone Strain." *Journal of Experimental Biology* 188 (1994): 217-233.

Zajac, F. E. "Muscle and Tendon: Properties, Models, Scaling, and Application to Biomechanics and Motor Control." *Critical Reviews in Biomedical Engineering* 17, no. 4 (1989): 359-411.

ACTA UNIVERSITATIS LAPPEENRANTAENSIS

440. BALANDIN, SERGEY, KOUCHERYAVY, YEVGENI, JÄPPINEN, PEKKA, eds. Selected Papers from FRUCT 8. 2011.

441. LAHTI, MATTI. Atomic level phenomena on transition metal surfaces. 2011. Diss.

442. PAKARINEN, JOUNI. Recovery and refining of manganese as by-product from hydrometallurgical processes. 2011. Diss.

443. KASURINEN, JUSSI. Software test process development. 2011. Diss.

444. PEKKANEN, PETRA. Delay reduction in courts of justice – possibilities and challenges of process improvement in professional public organizations. 2011. Diss.

445. VANHALA, MIKA. Impersonal trust within the organization: what, how, and why? 2011. Diss.

446. HYNYNEN, KATJA. Broadband excitation in the system identification of active magnetic bearing rotor systems. 2011. Diss.

447. SOLONEN, ANTTI. Bayesian methods for estimation, optimization and experimental design. 2011. Diss.

448. JABLONSKA, MATYLDA. From fluid dynamics to human psychology. What drives financial markets towards extreme events. 2011. Diss.

449. MYÖHÄNEN, KARI. Modelling of combustion and sorbent reactions in three-dimensional flow environment of a circulating fluidized bed furnace. 2011. Diss.

450. LAATIKAINEN, MARKKU. Modeling of electrolyte sorption – from phase equilibria to dynamic separation systems. 2011. Diss.

451. MIELONEN, JARI. Making Sense of Shared Leadership. A case study of leadership processes and practices without formal leadership structure in the team context. 2011. Diss.

452. PHAM, ANH TUAN. Sewage sludge electro-dewatering. 2011. Diss.

453. HENNALA, LEA. Kuulla vai kuunnella – käyttäjää osallistavan palveluinnovoinnin lähestymistavan haasteet julkisella sektorilla. 2011. Diss.

454. HEINIMÖ, JUSSI. Developing markets of energy biomass – local and global perspectives. 2011. Diss.

455. HUJALA, MAIJA. Structural dynamics in global pulp and paper industry. 2011. Diss.

456. KARVONEN, MATTI. Convergence in industry evolution. 2011. Diss.

457. KINNUNEN, TEEMU. Bag-of-features approach to unsupervised visual object categorisation. 2011. Diss.

458. RUUSKANEN, VESA. Design aspects of megawatt-range direct-driven permanent magnet wind generators. 2011. Diss.

459. WINTER, SUSANNA. Network effects: scale development and implications for new product performance. 2011. Diss.

460. JÄÄSKELÄINEN, ANSSI. Integrating user experience into early phases of software development. 2011. Diss.

461. KÄÄRIÄINEN, TOMMI. Polymer surface modification by atomic layer deposition. 2011. Diss.

462. KOCHURA, ALEKSEY. Growth, magnetic and transport properties of InSb and II-IV-As2 semiconductors doped with manganese. 2011. Diss.

463. PUTKIRANTA, ANTERO. Possibilities and challenges of longitudinal studies in operations management. 2011. Diss.

464. HAPPONEN, ARI. Muuttuvaan kysyntään sopeutuva varastonohjausmalli. 2011. Diss.

465. VASAVA, PARITOSH. Application of computational fluid dynamics in modelling blood flow in human thoracic aorta. 2011. Diss.

466. PURO, LIISA. Identification of extractives and polysaccharides as foulants in membrane filtration of pulp and paper mill effluents. 2011. Diss.

467. LAPPALAINEN, PIA. Socially Competent Leadership – predictors, impacts and skilling in engineering. 2012. Diss.

468. PLAMTHOTTATHIL, ANSHY OONNITTAN. Application of electrokinetic Fenton process for the remediation of soil contaminated with HCB. 2012. Diss.

469. EBRAHIMI, FATEMEH. Synthesis of percarboxylic acids in microreactor. 2012. Diss.

470. JANTUNEN, SAMI. Making sense of software product requirements. 2012. Diss.

471. VILKO, JYRI. Approaches to supply chain risk management: identification, analysis and control. 2012. Diss.

472. TANSKANEN, VESA. CDF modelling of direct contact condensation in suppression pools by applying condensation models of separated flow. 2012. Diss.

473. HUHTANEN MIKKO. Software for design of experiments and response modelling of cake filtration applications. 2012. Diss.

474. PARJANEN, SATU. Creating possibilities for collective creativity Brokerage functions in practice-based innovation. 2012. Diss.

475. KUKKONEN, SAKU. Generalized differential evolution for global multi-objective optimization with constraints. 2012. Diss.

476. LAAKSONEN, JONNA. Tactile-proprioceptive robotic grasping. 2012. Diss.

477. KALLIO, ANNE. Enhancing absorptive capacity in a non-research and development context An action research approach to converting individual observations into organizational awareness. 2012. Diss.

478. LÄTTILÄ, LAURI. Improving transportation and warehousing efficiency with simulation based decision support systems. 2012. Diss.

479. OYOMNO, WERE. Usable privacy preservation in mobile electronic personality. 2012. Diss.

480. LINNALA, MIKKO. Simulation and optimization tools in paper machine concept design. 2012. Diss.

481. KORPIJÄRVI, JUHA. Aging based maintenance and reinvestment scheduling of electric distribution network. 2012. Diss.

482. KORHONEN, JUHAMATTI. Active inverter output filtering methods. 2012. Diss.